In-situ observations of materials properties with Auger electron spectroscopy

van Agterveld, Dimitri

RIJKSUNIVERSITEIT GRONINGEN

IN-SITU OBSERVATIONS OF MATERIALS PROPERTIES WITH AUGER ELECTRON SPECTROSCOPY

PROEFSCHRIFT

ter verkrijging van het doctoraat in de
Wiskunde en Natuurwetenschappen
aan de Rijksuniversiteit Groningen
op gezag van de
Rector Magnificus, dr. D.F.J. Bosscher,
in het openbaar te verdedigen op
vrijdag 7 december 2001
om 16.00 uur
door

Dimitri Theodoor Leon van Agterveld

geboren op 23 augustus 1974
te Huizen

Promotor: Prof. dr. J.Th.M. De Hosson

Beoordelingscommissie: Prof. dr. A. van Veen
Prof. dr. D. Boerma
Prof. dr. ir. E. van der Giessen

In-situ observations of materials properties with Auger electron spectroscopy
University of Groningen, 2001
Print: Groningen University Press
Cover: Forest in Malaysia, where the treetops obtain their shape through mutual interaction, as do the grains in Ni_3Al (backside). The addition of boron to Ni_3Al enhances the interaction between the grains during deformation processes. The image was taken during the 'East 96'trip.

ISBN: 90 367 1519 9

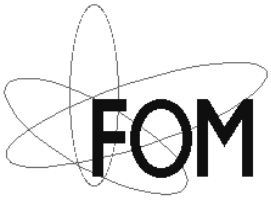

The work described in this thesis is part of the Priority Programme for Materials Research. It has been made possible by financial support from the Foundation for Fundamental Research on Matter (FOM-Utrecht).

CONTENTS

LIST OF PUBLICATIONS

D.T.L.van Agterveld, G. Palasantzas, J.Th M.De Hosson
Surface sensitivity effects with local probe scanning Auger-scanning electron microscopy
Applied Physics Letters **75** (1999) 1080

D.T.L.van Agterveld, G. Palasantzas, J.Th M.De Hosson
Magnesium surface segregation and oxidation in Al-Mg alloys studied with local probe scanning Auger-scanning electron microscopy
Applied Surface Science **152** (1999) 250

D.T.L.van Agterveld, G. Palasantzas, J.Th M.De Hosson
Effects of precipitates in Cu upon impact fracture: an ultra-high-vacuum study with local probe scanning Auger-electron microscopy
Acta Materialia **48** (2000) 1995

D.T.L.van Agterveld, G. Palasantzas, J.Th M.De Hosson
Local probe scanning Auger–electron microscopy studies of segregation effects upon in-situ fracture
Conference Proceedings Euromat 1999 (Eds. B. Jouffrey and J. Svejcar) **4** (2000) 87

D.T.L.van Agterveld, G. Palasantzas, J.Th M.De Hosson
Surface sensitivity effects with local probe scanning Auger – scanning electron microscopy
Materials Research Society Symposium Proceedings **589** (2000) 134

S.A. Koch, D.T.L.van Agterveld, G. Palasantzas, J.Th M.De Hosson
Electron beam induced oxidation of surfaces of Ni_3Al-base alloys
Surface Science Letters **476** (2001) L267

S.A. Koch, D.T.L.van Agterveld, G. Palasantzas, J.Th M.De Hosson
Influence of oxidation on boron segregation to grain boundaries of in-situ fractured Ni_3Al alloys
Materials Research Society Symposium Proceedings **654** (2001) 121

D.T.L.van Agterveld, S.A. Koch, G. Palasantzas, J.Th M.De Hosson
Ultra high vacuum scanning Auger/electron microscopy studies of oxidation and B surface segregation of in situ fractured B-doped Ni_3Al alloys
Surface Science **482-485** (2001) 254

G. Palasantzas, D.T.L.van Agterveld, S.A. Koch, J.Th M.De Hosson
Influence of electron flux on the oxidation of Ni_3Al surfaces
Journal of Vacuum Science and Technology A, accepted for publication, 2001

Chapter 1

INTRODUCTION

The segregation of elements to grain boundaries in engineering materials is of great technological importance, because it may have a considerable influence on mechanical properties, such as strength and interface toughness. One of the most illustrious examples is the catastrophe with the Royal Mail Ship 'Titanic' in 1912. Investigations on material, retrieved from the bottom of the ocean in 1985, revealed that the steel contained large amounts of sulfur and phosphorus, compared to present-day steels [1]. The presence of these segregating impurity elements, together with a low amount of manganese, leads to an increase in the ductile-brittle transition temperature (DBTT). This means that an otherwise ductile material can become brittle easily, once the temperature is reduced below the DBTT.

Another classical example of the change in properties of a material upon addition of another element is the embrittlement of copper by small amounts of bismuth, which was first observed in 1874 [2]. Only with the advent of Auger electron spectroscopy in the seventies of the last century it was shown that this was caused by grain boundary segregation, i.e. the enrichment of bismuth at the grain boundaries in copper. The accumulation of impurity atoms at grain boundaries leads to the formation of a very narrow zone with a different chemical composition, having a large influence on the interface. Very small bulk concentrations of impurity atoms can already lead to significant amounts of those atoms at the grain boundary. This may drastically change the response of a material on mechanical loading and can eventually lead to brittle failure of an otherwise ductile material.

Although grain boundary segregation in most engineering materials is detrimental to the materials properties, in some cases it has a positive effect.

One of the examples is the ductilizing effect of the addition of boron to Ni_3Al with a slightly Ni-rich composition [3], where boron was observed to segregate to the grain boundaries [4].

The embrittlement or ductilization by solute segregation was explained within a thermodynamical framework [5]. According to this theory, a segregating solute will embrittle the material if it has a higher free energy of segregation to a free surface, compared to the free energy of grain boundary segregation. Therefore, a solute with a higher tendency for grain boundary segregation than for surface segregation will increase the ductility of a material.

The objective of the research described in this thesis is to study the influences of impurity segregation on the materials properties in polycrystalline alloys. The alloys that are used contain a relatively low number of different elements, which will minimize obscuring effects such as the interaction between segregating impurities. In this way, macroscopic changes can be correlated to the influences of the specific elements. In principle, if the influence of a segregating element is known, it would be possible to tailor materials for specific applications.

Through in-situ intergranular fracture in a combined scanning electron – scanning Auger microscope, grain boundaries are exposed, which enables the study of grain boundary segregation and its dependence on previous heat treatments and bulk composition. A direct comparison between grain boundary and surface segregation can be made when pores, which were internal surfaces during materials processing, are present on the fracture surface. Because of the high surface sensitivity of Auger electron spectroscopy and the use of a field emission gun, segregation can be studied with a high lateral as well as depth resolution.

However, the instrumental conditions with which segregation is studied may influence surface segregation of several species as well. Surface oxidation leads to surface segregation of elements with high oxygen affinities. Prolonged exposure of a clean fracture surface to an electron beam leads to enhanced oxidation, compared to the non-exposed areas on which only oxygen chemisorption takes place. The phenomenon of electron beam enhanced oxidation is found to obscure the observation of surface segregation as a function of time. Therefore, knowledge of the influence of an electron beam on the processes at a surface is indispensable when interpreting the acquired segregation data. Nevertheless, it enables a study of the kinetics of oxidation at

room temperature in a UHV atmosphere where residual gases cause surface oxidation. Several oxidation models have been developed in the past for the oxidation of pure Ni exposed to low oxygen pressures [6,7]. The validity of these models for the oxidation of Ni_3Al under the influence of an electron beam will be examined.

The materials that are studied throughout this thesis are Al-Mg, Cu-Sb, Cu-Bi and Ni_3Al (with or without boron) alloys. Aluminum – magnesium based alloys are suitable candidates for a wide range of applications because they are characterized by excellent corrosion resistance, formability and weldability [8,9]. Enhanced Mg segregation to the surface can detoriate such properties because it leads to the formation of relatively thick, brittle oxides. Besides the fact that strain can be released upon Mg surface segregation, oxidation of the surface is a driving force for Mg segregation as well, because of the high oxygen affinity of Mg.

Segregation of both Bi and Sb in Cu is studied in combination with the presence of small amounts of sulfur. For Bi and Sb, chemically similar because they are in the same column of the periodic table, strain release is the main driving force for grain boundary segregation. The segregation of sulfur occurs through very fast diffusion of sulfur-vacancy complexes and Cu_2S formation at defects. Studies of site competition between S and Sb/Bi at surfaces and grain boundaries yield information about the influence of each of these elements on failure phenomena.

The strongly ordered aluminide Ni_3Al has attractive properties for structural applications. The flow stress of single crystalline material increases with increasing temperature and at high temperatures, an oxide layer is formed that protects against corrosion. However, polycrystalline Ni_3Al is extremely brittle at room temperature. The addition of boron, which segregates to the grain boundaries, circumvents this problem. Auger electron spectroscopy observations of segregated boron are combined with orientation imaging microscopy to study processes at the grain boundaries and with tensile experiments to examine the influence on ductility and fracture behavior. The influences of boron concentration, grain size and grain boundary character distribution, thermomechanical treatments and the presence of a notch in the test specimens are investigated.

In chapter 2, theories of segregation and its influence on materials properties will be described, as well as the experimental setup. This will be illustrated with

results obtained from in situ heating experiments on an Al-20 at.% Mg alloy. The alloy decomposes in two phases, enabling the observation of Mg surface segregation in materials with different Mg concentration. In chapter 3, the oxidation of Ni and Ni_3Al(-B) under the influence of an electron beam is discussed. The validity of the oxidation model will be tested by varying the incident electron flux. In chapter 4, the results on Sb and Bi segregation in Cu, in combination with the presence of S, will be presented. Finally, chapter 5 describes the influences of boron segregation on the mechanical properties of Ni_3Al.

REFERENCES

1. K. Felkins, H.P. Leighly Jr., A. Jankovic, JOM **50** (1998) 12
2. W. Hampe, Z. Berg-, Hütten- u. Salinen-Wesen **22** (1874) 93
3. K. Aoki, O. Izumi, Nippon Kinzoku Gakkaishi, **43** (1979) 1190
4. C.T. Liu, C.L. White, J.A. Horton, Acta Metall. **33** (1985) 213
5. J.R. Rice, J.S. Wang, Mat. Sci. Eng. A **107** (1989) 23
6. P.H. Holloway, J.B. Hudson, Surf. Sci. **43** (1974) 123
7. Wei Li, M.J. Stirniman, S.J. Sibener, J. Vac. Sci. Technol. A **13** (1995) 1574
8. J.E. Hatch (Ed.), Aluminum: Properties and Physical Metallurgy, American Society for Metals, Metals Park, OH (1984)
9. F.J. Esposto, C.-S. Zhang, P.R. Norton, R.S. Timsit, Surf. Sci. **302** (1994) 109

Chapter 2

BASIC CONCEPTS

2.1 THEORY OF SEGREGATION

2.1.1 Segregation and materials properties

Segregation can be defined as the enrichment of a material constituent at a surface or internal interface of a material. In a polycrystalline solid, the internal adsorption sites are at defects such as dislocations, grain boundaries, stacking faults and the interfaces with precipitates or another phase in the solid [1]. A grain boundary in a polycrystalline solid is a narrow zone with a certain degree of misfit between two crystallographically ordered crystals. Impurity atoms, present in solution in one of those crystals, may have an associated strain energy if they do not 'fit' in the crystal due to their size. An impurity atom can replace matrix atoms at the grain boundary, thereby releasing its strain. Simultaneously, the preexisting strain at the grain boundary is reduced. Segregation is the shift of solute atoms from the interior of the grain to concentrate at a grain boundary, surface or other interface. It is called equilibrium segregation to the extent that is governed thermodynamically through the appropriate free energy of segregation [2]. Although the occurrence of intergranular fracture in steels containing arsenic, phosphorus and sulfur was noted already in 1894 [3], the partitioning of the solute atoms between grain boundary and the lattice was predicted first by McLean in 1957 [4].

Very small bulk concentrations of impurity atoms can lead to significant amounts of those atoms at the grain boundary. Although the segregation can be very intense, the extent or the width of the segregation layer is very narrow, typically of the order of one monolayer or a few atomic layers [5]. Segregation

to grain boundaries has been observed in many materials and it was found that the intensity of segregation is related to the solubility of the impurity elements in the matrix material [6]. Impurities with low solubilities have high grain boundary enrichment ratios, i.e. the ratios between grain boundary and bulk concentration, that can be as high as ~ 10^5. Segregation of elements in solid solution, governed by equilibrium segregation theory, usually does not lead to precipitation. However, the intense segregation to interfaces can result in a change of properties.

The most extensive work has been done on the effect of impurity segregation on fracture of materials. Early work already showed embrittlement of iron due to the addition of small amounts of oxygen [7]. Due to grain boundary embrittlement, the fracture mode of the material changed from cleavage to intergranular, with the fracture path closely following the grain boundaries. This behavior is typical of materials that have undergone certain types of heat treatments when impurities are present. The heat treatments lead to the accumulation of impurities at the grain boundary. The effect of segregation on surface and interfacial energies is well established [8]. It has been shown that the surface or interface energy is reduced by segregants and that those segregants that are highly surface active lead to the most drastic reduction.

The effects of segregants on grain boundary cohesion have been the subject of many discussions. Calculations for segregants in all matrices in the ideal solution approximation have given an indication of the influence of segregation on the grain boundary cohesion [9]. These calculations suggest an explanation of the observed embrittlement of copper by bismuth [10] and the improvement in ductility of nickel-aluminum alloys by grain boundary segregation of boron [11]. However, an increase in grain boundary cohesion cannot be related directly to a decrease in the propensity of intergranular fracture. The temperature at which fracture takes place may influence the fracture process, as will be discussed below. Roughly speaking, at a crack tip, the occurrence of either dislocation nucleation and emission or atomic bond breaking determines whether or not ductile or brittle fracture occurs.

Effects of segregation on mechanical properties have been presented within a thermodynamic framework [12]. The embrittlement of grain boundaries by solute segregation was formulated in terms of the ideal work of interfacial separation, $2\gamma_{int}$. It was suggested that control of $2\gamma_{int}$,

$$2\gamma_{\text{int}} = (2\gamma_{\text{int}})_0 - (\Delta G^0_{GB} - \Delta G^0_{FS})\Gamma \qquad (2.1)$$

where $(2\gamma_{int})_0$ is the work of separation of a fully clean interface and Γ is the excess interfacial solute coverage (concentration per unit area), is the most appropriate way of enhancing interfacial resistance to fracture. ΔG^0_{GB} and ΔG^0_{FS} are usually negative and represent the free energies of segregation to the grain boundary and free surface, respectively, evaluated at the same temperature.

Embrittlement (or ductilization) by solute segregation can now be explained with equation (2.1) in terms of $2\gamma_{int}$: a segregating solute with a greater free energy of segregation to a free surface compared with ΔG^0_{GB} (i.e. more negative) will embrittle, because $2\gamma_{int}$ will be reduced. In contrast, a lower free energy at a boundary compared with ΔG^0_{FS} will enhance interfacial cohesion, i.e. $2\gamma_{int}$ increases.

However, even more important than these brittle fracture modes is the effect of segregation on the ductile-brittle transition temperature (DBTT). Above that temperature a material is ductile, whereas it becomes brittle when the temperature decreases below the DBTT. An otherwise ductile material becomes brittle because the DBTT is raised. The effects of segregants have been reported generally as variations in DBTT, i.e. δ DBTT, associated with a variation in solute coverage, $\delta\Gamma$,

$$\delta DBTT \propto \delta\Gamma \qquad (2.2)$$

According to equation (2.1) solute segregation influences the DBTT via the effect on $2\gamma_{int}$ and

$$\frac{\delta DBTT}{\delta\Gamma} \propto (\Delta G^0_{GB} - \Delta G^0_{FS}) \qquad (2.3)$$

In some cases, the DBTT has been observed to be inversely related to the impact fracture toughness, $K_{IC,}$ and K_{IC}^{-1} versus Γ should be approximately linear. The latter is confirmed for P and C segregants in ferritic steels.

Equation (2.1) has been postulated by Hirth and Rice [13]. When there is no redistribution of the segregants, the reduction in the ideal work of fracture, namely

$$\Delta 2\gamma_{\text{int}} = -\int_0^{\Gamma_{GB}} \left[\left(\frac{\delta G_{GB}(\Gamma)}{\delta n_i} \right)_{P,T,n_j} - \left(\frac{\delta G_{FS}(\Gamma)}{\delta n_i} \right)_{P,T,n_j} \right] d\Gamma \qquad (2.4)$$

where $\left(\frac{\delta G(\Gamma)}{\delta n_i} \right)_{P,T,n_j}$ is the chemical potential of solute n_i in equilibrium with Γ

at the boundary or free surface, leads in the dilute limit to equation (2.1). Finally, it should be emphasized again that at a crack tip it is the critical choice between dislocation nucleation and emission versus atomic bond breaking that determines whether or not ductile or brittle fracture occurs. Segregants may offset the total embrittling effect described by equation (2.3) because of their contribution to the ease of dislocation emission at the crack tip.

2.1.2 Free energy and kinetics of segregation

The theories of segregation developed rapidly in the seventies, when large amounts of data from Auger electron spectroscopy measurements became available. The theories describe the final equilibrium state. However, in practical situations segregation is limited by diffusion and therefore the kinetics of the process has to be considered as well. In the earliest theory, specifically for grain boundaries, McLean proposed a model with the solute atoms populating grain boundary and lattice sites with an energy difference ΔG_{GB}, the free energy of segregation [4]. The system energy was minimized for a fractional monolayer of segregant, X_{GB}, at the grain boundary, which yields

$$\frac{X_{GB}}{X_{GB}^0 - X_{GB}} = \frac{X_B}{1 - X_B} \exp\left(-\frac{\Delta G_{GB}}{RT} \right) \qquad (2.5)$$

where X_{GB}^0 is the fraction of the grain boundary monolayer available for segregated atoms at saturation and X_B is the bulk solute molar fraction. The theory is only valid for monolayer segregation, but was confirmed by, for example, grain boundary segregation data of phosphorus in iron [14]. It predicts higher grain boundary concentrations with higher X_B and at lower temperatures. Values of ΔG_{GB} in a binary system were estimated from the elastic strain energy, w, fully released by the segregation of solute atoms [4,15]. The

solute atom is represented by an elastic sphere fitted into a spherical hole in an elastic matrix continuum, which yields

$$w = \frac{24\pi K \mu_0 r_0 \quad (r_1 - r_0)^2}{3K + 4\mu_0} \tag{2.6}$$

Here, K is the bulk modulus of the segregating impurity, r_0 and r_1 are the atomic radii of the matrix and impurity atoms, respectively, and μ_0 is the shear modulus of the matrix. This yields values of ΔG_{GB} that agree with experimental observations to a factor of two. Better agreement can be obtained when the solid state analogue [16]

$$\frac{X_{GB}}{X_{GB}^0 - X_{GB}} = \frac{X_B}{1 - X_B^0} \exp\left(-\frac{\Delta G'}{RT}\right) \tag{2.7}$$

is used, where X_B^0 is the solid solubility, which is well known for many elements. $\Delta G'$ is the difference between the free energies of grain boundary segregation and precipitation, $\Delta G_{gb} - \Delta G_{sol}$.

When the regular solution model for a binary system is used, equation (2.5) is valid for surface segregation as well, substituting X_s for X_{GB} [17]. The free energy of surface segregation is $\Delta G_s = \Delta H_s - T\Delta S$. The enthalpy is given by

$$\begin{aligned} -\Delta H_s = \gamma_0^S - \gamma_1^S - \frac{2H_m}{Z X_B (1 - X_B)} \left[Z_1 (X_B - X_S) + Z_V \left(X_B - \frac{1}{2} \right) \right] \\ + \frac{24\pi K \mu_0 r_0 (r_1 - r_0)^2}{3K + 4\mu_0} \end{aligned} \tag{2.8}$$

where γ_0 and γ_1 are the matrix surface energies without and with solute, H_m is their heat of mixing, Z and Z_1 are the coordination numbers in the matrix and at the surface and Z_v is the coordination number for surface atoms to the layer below. The last term in equation (2.8) is equal to equation (2.6), governed by the mismatch between solute and matrix atoms [18-20]. For solid metals the surface energies scale with the melting points. The surface segregation enrichment ratio increases when the solute atom size is larger than the matrix atom size and when the melting point of the solute is lower than that of the matrix [2].

The presence of a chemisorbed gaseous species on the surface can have an effect on the surface composition of a binary alloy. In the presence of a coverage of a chemisorbed species θ, it was proposed that equations (2.5) and (2.8) will be valid, with the free energy of surface segregation given by ΔG_{chem} [21], where

$$\Delta G_{chem} = \Delta G_S + (E_B - E_A)\theta \tag{2.9}$$

E_A and E_B are the chemisorption energies of the gas on solute A and matrix B.

At high temperatures, evaporation from a surface can take place, which causes a deviation from equation (2.5). At low temperatures, both grain boundary and surface segregation can be limited by the diffusion of atoms from the bulk to the surface or interface. In most practical situations, the kinetics of segregation is of importance. Most models of segregation kinetics follow McLean's approach [4]. Solute atoms are assumed to segregate to a grain boundary from two infinite half-crystals or to a surface from one infinite half-crystal. Diffusion in the crystals is described by Fick's laws and the ratio of grain boundary to bulk concentration is given by a presumably constant grain boundary enrichment ratio β. In practice, β is only constant for dilute systems with low segregation levels. The kinetics of segregation is described by

$$\frac{X_{GB}(t) - X_{GB}(0)}{X_{GB}(\infty) - X_{GB}(0)} = 1 - \exp\left(\frac{FDt}{\beta^2 f^2}\right)\mathrm{erfc}\left(\frac{FDt}{\beta^2 f^2}\right)^{1/2} \tag{2.10}$$

where F = 4 for grain boundaries and 1 for the free surface, $X_{GB}(t)$ is the boundary content at time t, D is the solute bulk diffusivity and f is related to the atom sizes of the solute and matrix atoms, a and b respectively, by $f = b^3 a^{-2}$.

The descriptions given in this paragraph all assume equilibrium, monolayer segregation; non-equilibrium segregation depends on changes in the microstructure, quench rates as well as structural and thermal vacancies.

2.2 AUGER ELECTRON SPECTROSCOPY

In 1968, two reports were published [22,23], following the notion that Auger electrons from solids could be used for surface analysis [24]. When a sample is irradiated with electrons from a source, having a primary energy in the order of keVs, core electrons are ejected from a depth extending up to 1 μm. The incident

electron collides with an electron in an inner shell of an atom, e.g. the K-shell, as is schematically illustrated in figure 2.1, step 1. This process is most efficient when the incident electron has an energy that is more than five times the energy of the core electron. The electron in the K-shell is ejected (step 2), leaving the atom in an ionized state. The hole in the K-shell is filled by an electron from the L_1 shell (step 3), releasing an amount of energy ($E_K - E_{L1}$), which can appear as a photon with this energy or can be transferred to another electron. In this example the third electron, called Auger electron after Pierre Auger who was the first to observe such events in a cloud chamber [25], is in the $L_{2,3}$ shell and is ejected (step 4) with a kinetic energy [2]

$$E_{KL_1L_{2,3}} = E_K - E_{L_1} - E^*_{L_{2,3}} \tag{2.11}$$

The asterisk in the last term stems from the fact that it represents the binding energy of an electron in the presence of a hole, instead of in the ground state, which is usually a small difference. Because Auger emission involves (at least) three electron shells and is not subject to any selection rules, a large number of possible Auger transitions exists. Their relative probabilities, however, are determined by the mutual coupling between the two electrons involved in the recombination and by the number of similar electrons present in the atom. The most intensive transitions that are consequently best suited for analysis involve adjacent shells, such as the KLL, LMM, and MNN series. Almost all elements show strong lines of these series in the energy range up to 3 keV.

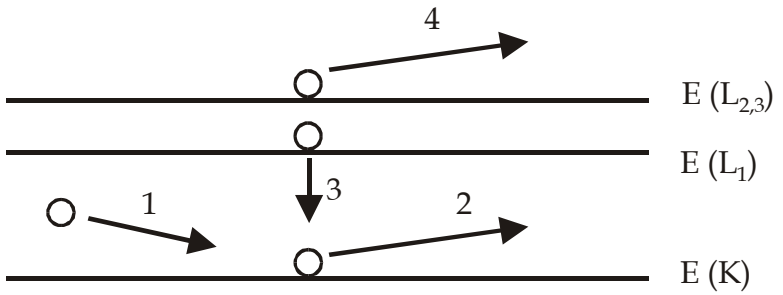

Figure 2.1: *Schematic diagram of the process of KLL Auger electron emission in a solid*

The kinetic energy of the ejected Auger electrons can be determined by a spectrometer. Because the binding energies in elements are known, the elements present at the electron bombarded surface can be determined from the peaks in the observed spectrum corresponding to the Auger transitions. All elements, except hydrogen and helium, can be identified, because three different electrons are involved in the process. Furthermore, the number of

detected Auger electrons with a certain kinetic energy can be related to the quantity of the corresponding element present in the volume of analysis, enabling compositional analysis of the surface region.

The volume of analysis is laterally determined by the spot size of the electron beam. A fraction of the Auger electron signal is emitted from a region of the diameter of the incident electron beam and a fraction from a larger region defined by the backscattering [2]. However, when well focused electron beams with relatively large currents are used (currents ~1 nA and probe sizes smaller than 50 nm), the effect of backscattering is negligible [26] and the lateral resolution is mainly determined by the beam size. The intense elastic scattering of the Auger electrons is the reason of the surface sensitivity. Only Auger electrons ejected from the outermost atomic layers in a solid can reach the detector without energy loss. Scattered electrons are recaptured or contribute to the large smooth background in an Auger spectrum. Estimations of the inelastic mean free path λ of electrons with a certain energy in solids are made by numerical calculations [27]. The surface sensitivity of Auger electron spectroscopy makes it a suitable technique for the study of processes at solid surfaces, such as segregation and oxidation. Nowadays, Auger electron spectroscopy has become the most frequently used technique for providing compositional information on many types of surfaces, thin films and interfaces. In particular, Auger electron spectroscopy has some important advantages: submicrometer lateral resolution, good detection possibilities for light elements, the ability to construct depth profiles and a high surface sensitivity.

2.3 INSTRUMENTATION

The instrument that is employed to perform Auger electron spectroscopy is a modified JEOL JAMP 7800F. It is a combined scanning electron and scanning Auger microscope, operating under ultra high vacuum conditions and equipped with a field emission electron gun. Electrons are generated in the field emission source, passing electrostatic condenser and objective lens systems before they hit the specimen surface. Typical conditions are an accelerating voltage of 10 kV and a primary beam current of 2.4 nA. A schematic setup of the system is shown in figure 2.2.

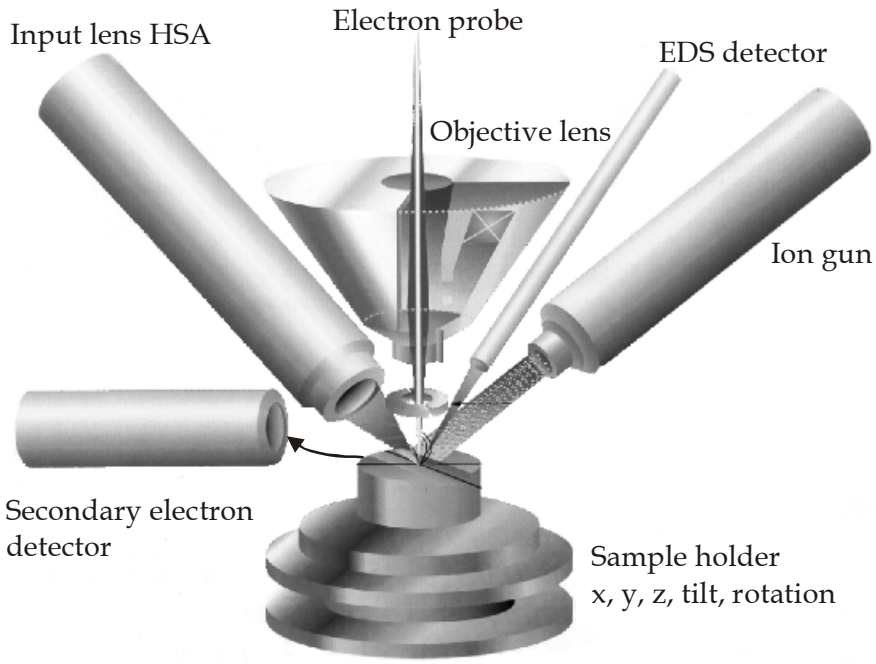

Figure 2.2: *Schematic setup of the JEOL JAMP 7800F*

The system contains three detectors: a secondary electron (SE) detector, a hemispherical analyzer (HSA) and an energy dispersive X-ray detector. Secondary electrons have very low energies, typically less than 50 eV, and therefore only secondary electrons that originate from the specimen surface reach the SE detector. The incident electron beam is scanned across the surface and simultaneously the number of secondary electrons originating from the irradiated part of the surface is counted. This yields an image of the scanned surface, which is commonly referred to as scanning electron microscopy (SEM). Topography has a large influence on the number of emitted secondary electrons, compared to the elemental composition of the surface, the crystal orientations and other contributions. This enables an easy, quick observation of the microstructure of a surface.

During scanning, the electron beam is focused as much as possible. The resolution of the obtained secondary electron image is mainly determined by the beam size, due to the low energy and surface sensitivity of the secondary electrons. The JAMP 7800F can accomplish a resolution of ~ 5 nm, with an incident current of ~ 10^{-11} A. This current yields sufficient secondary electrons to obtain a scanning electron image, but not enough Auger electrons to obtain a

spectrum with a reasonable signal-to-noise ratio. The incident current has to be increased to ~ 10^{-9} A to accomplish this. The advantage of a field emission electron gun is that it can vary the beam current over several orders of magnitude without much loss of resolution. The resolution for the beam current used throughout this thesis, 2.4 nA with 10 kV accelerating voltage, is about 15 nm. Electron beam irradiation of a surface can lead to heating in the case of insulators [28] and to enhanced oxidation in the case of metals [29], which may lead to irreversible structural changes at the surface.

Energy dispersive X-ray spectroscopy (EDS) detects the X-rays that leave the specimen after the second step in the Auger process. Therefore, their energy is element specific as well, enabling compositional analysis. Because X-rays are less prone to scattering in material, detected X-rays originate from depths in the order of ~1 μm. Due to backscattering, the lateral resolution is of the same order. Therefore, a combination of EDS and Auger electron spectroscopy (AES) in the same system can yield an immediate comparison between surface enrichment in the topmost atom layers (AES) and bulk composition (EDS). The EDS mainly used in the course of this thesis is attached to a Philips XL-30 SEM and is manufactured by EDAX.

The hemispherical analyzer acts as an energy separator for the emitted Auger electrons and detects electrons with a specific kinetic energy. It consists of two hemispherical plates, on which different potentials are applied. In this way, only Auger electrons with certain kinetic energy can reach the actual detectors. Through variation of the potentials of the two plates, Auger electrons with different energies can be detected. The operator defines the energy range, after which the number of incoming Auger electrons is counted as a function of energy. In this way, a spectrum of the number of detected Auger electrons (or current) versus their kinetic energy is obtained. The number of points in the spectrum is determined by the energy step size, which is typically 1 eV. The predefined dwell time is the time that incoming electrons are counted during one energy step, i.e. at a specific energy. Throughout this thesis, it ranges from 60 ms for fast scans to 400 ms for slow scans, used for quantification. Furthermore, the number of sweeps can be defined. This means that the acquisition of a spectrum on a point is repeated several times, after which the spectra are averaged. In this way, a better signal-to-noise ratio is obtained and the observed peaks are more clearly defined.

The specimens for analysis are mounted on a specimen holder. The specimen holder is transferred to the specimen stage inside the analysis chamber. The specimen stage can be moved along x-, y- and z-axes. Other degrees of freedom are specimen tilt toward the hemispherical analyzer and rotation.

Inside the analysis chamber, ultra high vacuum conditions are required. Electrons travelling from the electron source to the specimen surface and from the surface to the analyzer should encounter as few gas molecules as possible, otherwise they will be scattered and lost for analysis. This requires a vacuum of ~10^{-4} Pa, which is a moderate vacuum. The need for ultra high vacuum stems from the surface sensitivity of Auger electron spectroscopy. Because Auger electrons originate from depths of only a few atom layers, the technique is very sensitive to surface contamination. At a residual pressure of ~ 10^{-8} Pa and a sticking coefficient of unity, the buildup of one monolayer of contamination takes ~ 10^{4} seconds at room temperature. This time is sufficient to carry out most experiments. Ultra high vacuum is attained through the constant use of a combination of two sputter ion pumps and a turbomolecular pump. A titanium sublimation pump is operated at certain times. The exchange of specimens is performed via a separate chamber (load lock) to avoid disturbing the vacuum in the analysis chamber. During normal operation, the ambient pressure is of the order of $5 \cdot 10^{-8}$ Pa.

An essential feature of the JAMP 7800F for the experiments described in this thesis is the in situ fracture stage, which was acquired separately. The need for clean surfaces is evident from the aforementioned surface sensitivity of the Auger process. This can be accomplished by cleaning a contaminated surface in situ with inert ion sputtering, which may lead to compositional surface changes. Another possibility, i.e. in situ fracture, leads to very clean surfaces that remain clean for a certain period, depending on the pressure in the analysis chamber. If the fracture path follows the grain boundaries, i.e. the fracture is intergranular, the previous grain boundaries are exposed as free surfaces. In this way, grain boundary segregation can be studied.

Figure 2.3 shows the setup of the in situ fracture stage. It is connected to the analysis chamber and the specimen can be transferred by the magnetic loader under ultra high vacuum conditions. The specimen holder can accommodate three cylindrical specimens with a diameter of 3 mm and a length of ~ 15 mm. The specimens are cylindrically notched to promote and localize fracture. Furthermore, the specimen holder can be cooled indirectly through contact with

the cooling unit, which is filled with liquid nitrogen. In this way, brittle fracture can be promoted in otherwise ductile specimens. The specimens are fractured by the impact of the hammer rod on the right side of the image. The fracture process resembles the Charpy test.

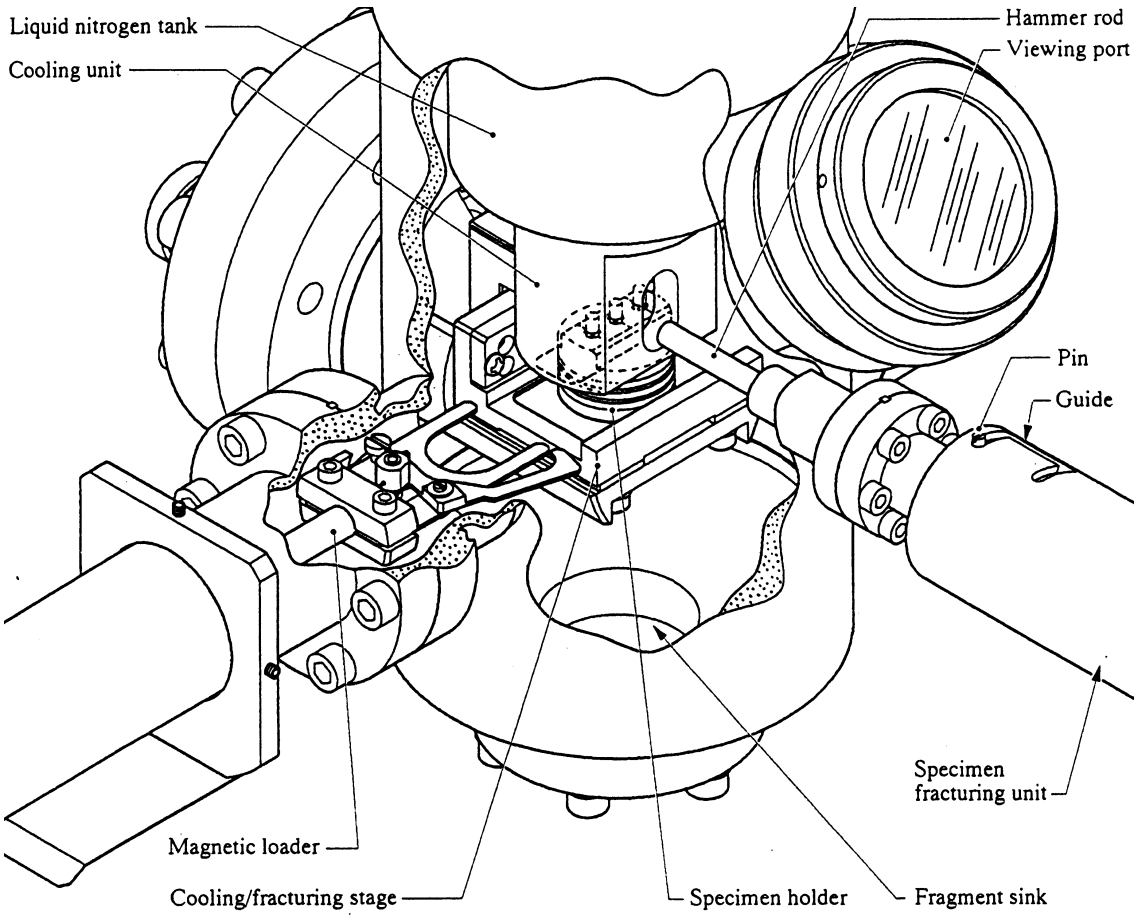

Figure 2.3: *Geometry of the in situ fracture stage*

2.4 MODES OF ANALYSIS

In the next paragraphs, the modes of analysis of the JEOL JAMP 7800F will be described and illustrated by experiments that are performed on an Al-Mg alloy.

2.4.1 The aluminum-magnesium alloy

Aluminum – magnesium based alloys are suitable candidates for a wide range of applications because they are characterized by excellent corrosion resistance, formability and weldability [30,31]. Enhanced Mg segregation to the surface can diminish such properties because it leads to the formation of relatively thick,

brittle oxides [31]. A number of studies on Al-Mg alloys has shed light on many aspects of Mg segregation and its influence on oxidation mechanisms [31-33]. In a study of an Al-10% Mg alloy by means of AES [34], it was found that at 700 K the surface oxide layer was largely magnesium oxide, being an order of magnitude thicker than the (mainly) aluminum oxide layer that was formed at room temperature. These findings were in agreement with results on alloys with low Mg contents (≤ 2.5 at.%) at temperatures around 700 K [33,35].

However, most of the previous studies were performed on systems with relatively low Mg contents, which were therefore in the single-phase regime. The studied material in this chapter is Al-Mg (80-20 at.%), which decomposes in two phases with different Mg contents [36]. Therefore, Mg surface segregation can be studied simultaneously in two phases with two different diffusion probabilities for Mg. Because the material is no longer homogeneous, the lateral resolution of the instrument has to be much smaller than the size of the present phases, which was not possible before the advent of field emission guns.

The influence of oxidation on Mg surface segregation is studied in an Al–Mg alloy (80%-20%), obtained as an ingot from Highways International. According to the Al-Mg phase diagram [36], decomposition will occur into the intermetallic β-phase, which is commonly referred to as Al_3Mg_2, and Al containing Mg in solid solution, Al(Mg). The structure of Al_3Mg_2 is complex [37], with a unit cell containing more than 1100 atoms. A characteristic feature of this structure is the large number of structural vacancies present.

Specimens are cut from the ingot and polished, in the final stage in a silica suspension. The polished specimens are sputter cleaned by 3 keV Ar^+ ions in the analysis chamber of the JAMP 7800F and in situ heated afterwards in the transfer chamber, to induce oxidation and surface segregation. Because the residual pressure in the transfer chamber is ~$2 \cdot 10^{-6}$ Pa during heating and both Al and Mg have very high oxygen affinities, the surface will be oxidized by residual water vapor. After cooling and transfer to the analysis chamber, the Auger intensities of Al, Mg and O are obtained.

2.4.2 Illustrations of the modes of analysis

After the acquisition of a scanning electron image, a point can be designated from which an Auger spectrum is obtained. Figure 2.4 shows a scanning electron image of the Al-Mg alloy, with the rough β-phase (top) and Al(Mg)

phase (bottom). EDS analysis showed that the β-phase contained 38 ± 1 at.% Mg and that the Al(Mg) phase contained 14 ± 1 at.% Mg. Although the intermetallic β-phase is commonly referred to as Al_3Mg_2, it is known to contain 38.2 at.% Mg [36], which agrees well with our result.

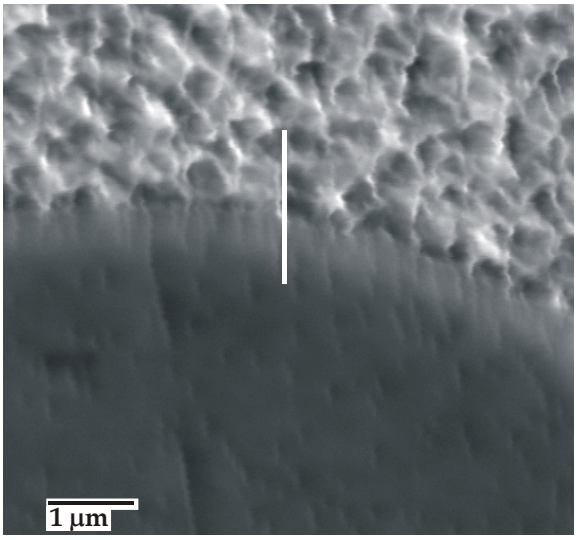

Figure 2.4: *SE image of the rough β-phase (top) and the smooth Al(Mg) (bottom). The vertical line is the line along which Auger intensities of O, Mg and Al are obtained*

A direct spectrum, obtained on the β-phase, is shown in figure 2.5 (top). The observed peaks in the spectrum are small compared to the background, consisting of secondary, backscattered and inelastically scattered Auger electrons. To overcome this problem, the spectrum is differentiated with respect to energy. In the early days of Auger electron spectroscopy this was done by modulating the detector for each kinetic energy, leading to longer measuring times. Nowadays, the spectra are differentiated numerically after completion of the direct spectrum, as is shown in figure 2.5 (bottom). The peaks become much clearer in this representation, due to the almost removed background.

By definition, the peak position in the direct spectrum is the position where the intensity has its local maximum. In the differential spectrum, the point with minimal intensity is defined as the peak position, instead of the point where the differential is zero, which would correspond to the peak maximum in the direct spectrum. Due to varying background conditions, the point where the differential spectrum has zero intensity may change, which can lead to minor variations in peak positions for the same element in different measurements.

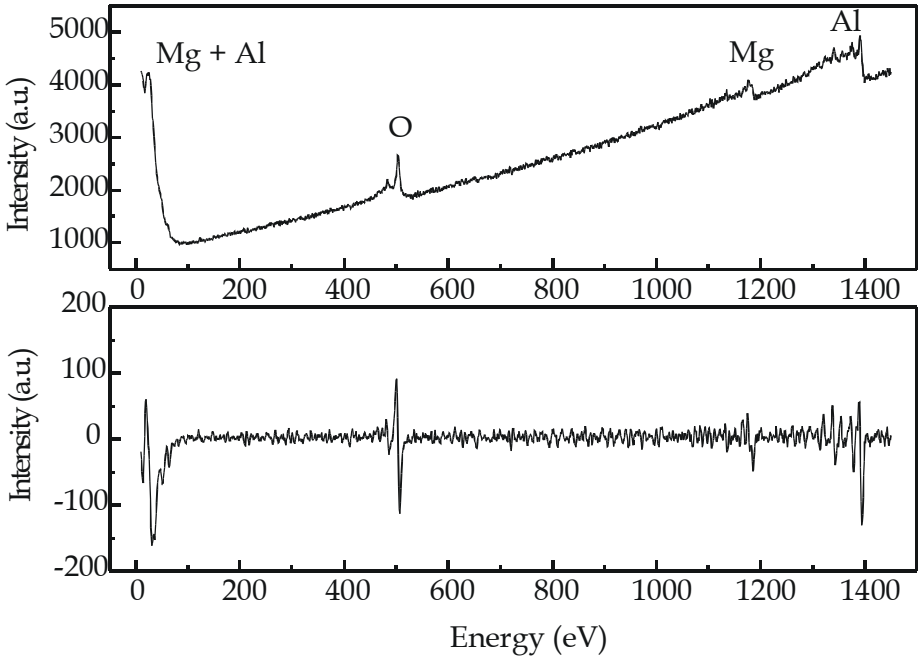

Figure 2.5: *Direct Auger spectrum of Al_3Mg_2 (top) and differential spectrum (bottom)*

The peaks of Mg and Al at the right end of the direct spectrum correspond to KLL transitions. The features in the beginning of the direct spectrum stem from LVV transitions, involving valence electrons. These features are much clearer in the differentiated spectrum on the bottom. Because of the lower energy of the LVV Auger electrons, their surface sensitivity is higher. In principle, a comparison between compositions of regions with different depths can be made by comparing the LVV and KLL transitions. Due to the overlap of Al and Mg LVV peaks, direct comparison is difficult. At ~ 506 eV, an oxygen peak is visible. In the differential spectrum, the most intense transitions are used to determine the intensities of Mg and Al. The Auger intensity is defined as the difference between the maximum and the minimum intensity of a transition in the differential spectrum. This intensity is also referred to as the Auger peak-to-peak height. As long as the differential spectrum is used, the terms intensity and peak-to-peak height are interchangeable in this thesis.

Differentiation of the spectra bears some disadvantages as well. The number of detected Auger electrons varies with topography, but the ratio of the Auger peak size to its background in the direct spectrum is rather insensitive to topographical changes. However, in the differential spectrum, most of the background is removed. Topographical corrections can be made only by comparing the intensities of different elements in the same spectrum, because the effect of topography is the same for all elements.

Before the Auger spectra are acquired, the analysis positions and the spot sizes have to be defined. Several analysis positions can be predefined, up to a maximum of 20, which are analyzed sequentially. For each analysis position, the used spot size can be defined separately. The spot size can be varied in steps of 5 μm from 0 to 300 μm, or a scan of the whole field of view can be obtained. Spot size '0' corresponds to the best focused electron beam with a spot size of ~15 nm. It can be useful to change from a nanometer sized spot to a micrometer sized spot, in order to obtain a better spatially averaged signal or to reduce electron beam effects, as will be shown later. When 20 points have to be analyzed sequentially, the measurements can be very lengthy. An efficient way of reducing the acquisition time is to measure only small parts of the spectrum, once it is known which elements are present in the specimen. The first measurement of a specimen always has to be a so-called 'wide scan spectrum', as is shown in figure 2.5, to determine the elements present. After that, only the small parts of the spectrum that contain the most intense Al, Mg and O transitions have to be acquired, which is called a 'split scan spectrum'. The only requirement is that these 'regions of interest' contain the peak maximum and minimum of the differential spectrum.

In the figures 2.6, 2.7 and 2.8 the I_O/I_{Al} and I_{Mg}/I_{Al} intensity ratios after oxidation are depicted as a function of position. The ratios of intensities are used to reduce topographical influences. The intensities are measured at a number of points on a straight line, traversing from the Al(Mg) phase into the β-phase, along the vertical line in figure 2.4. At the first point, r = 0. Annealing and oxidation treatments of the Al-Mg alloy are performed at three different temperatures, 180° C, 220° C and 520° C. All surfaces are sputter cleaned before the annealing/oxidation treatments. Annealing treatments consist of heating the sample to the designated temperature T and maintaining that temperature during a time Δt, thereby oxidizing the surface.

In these figures, a transition layer is observed over which the Mg/Al intensity ratio gradually increases as the beam moves from the Al(Mg) to the β-phase. For T = 180° and 220° C, the Mg/Al ratio on the Al(Mg) phase is not different from the room temperature ratio, although the surface is oxidized. It was observed earlier that there is no additional Mg enrichment when heating below 300° C [38]. The Mg/Al ratio of the β-phase increases from ~ 0.2 at room temperature to ~ 0.4 in both cases, accompanied by a large increment of oxygen. In the β-phase, Mg surface segregation is therefore possible at temperatures

below 300° C. This may be attributed to the large number of structural vacancies in the β-phase [37], which facilitates diffusion.

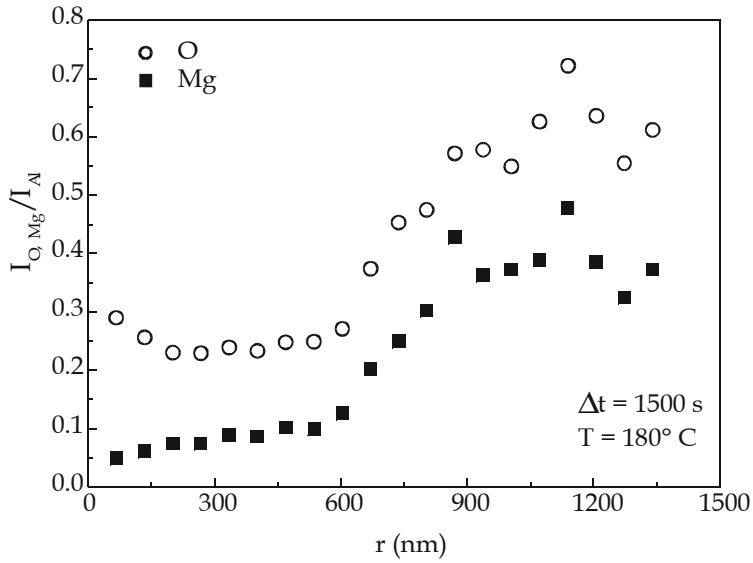

Figure 2.6: *I_O/I_{Al} and I_{Mg}/I_{Al} intensity ratios as a function of beam position after annealing at 180° C, obtained with minimum beam size (~ 15 nm)*

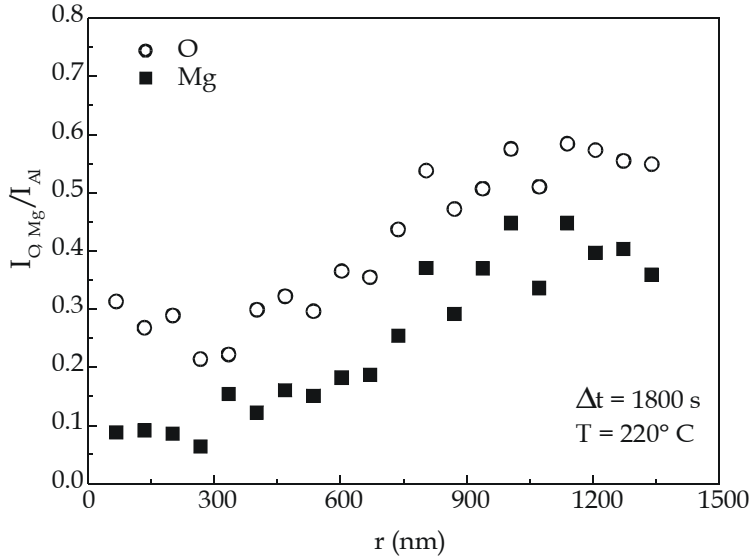

Figure 2.7: *I_O/I_{Al} and I_{Mg}/I_{Al} intensity ratios as a function of beam position after annealing at 220° C, obtained with minimum beam size (~ 15 nm)*

Figure 2.8 clearly shows that after heating at 520° C for 20 minutes, the difference in surface Mg/Al ratios between the two phases is much smaller than in the previous figures. This yields a less sharp transition between the two phases. This means that relatively more Mg surface enrichment occurred in the

Al(Mg) phase than in the β-phase. At a certain moment, the composition of the volume of Auger analysis does not change anymore and the amount of magnesium oxide is similar at the surfaces of both phases [31].

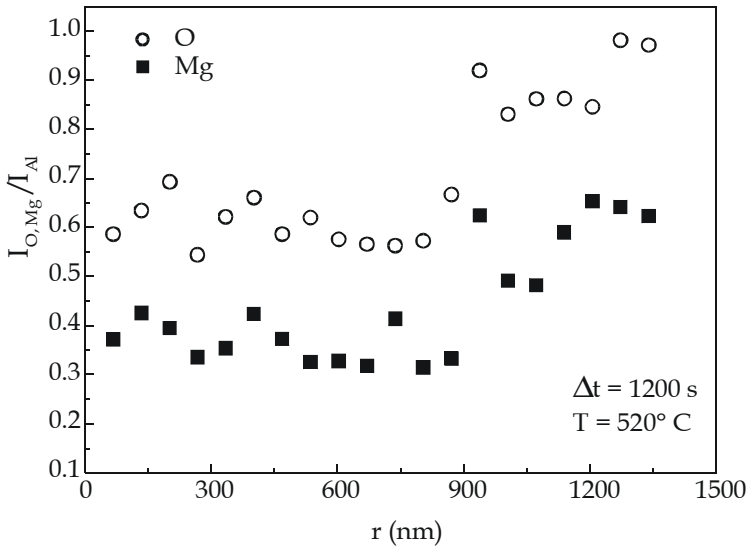

Figure 2.8: *I_O/I_{Al} and I_{Mg}/I_{Al} intensity ratios as a function of beam position after annealing at 520° C, obtained with minimum beam size (~ 15 nm)*

Annealing of a pure Al specimen below 300° C yields an O to Al intensity ratio of ~0.2, which is comparable to the ratios observed on the Al(Mg) surface after heating below 300° C. The amount of Mg in that phase is small and the observed Mg enrichment is minimal, which will lead to mainly aluminum oxide at the surface. When Mg surface segregation occurs, the O/Al ratios drastically increase, due to enhanced oxidation and the presence of less Al in the volume of analysis. Nevertheless, prolonged heating at 520° C does not lead to higher Mg intensities at the surface. This can be caused by saturation within the volume of analysis or by the fact that the presence of an oxide layer inhibits the rapid increment of Mg at the surface, because Mg diffusion in the oxide is much slower than in the alloy. The exact structure and composition of the formed oxide is unknown. Therefore, the formation of a spinel structure (Al_2MgO_4) cannot be ruled out.

Two other, closely related modes of analysis are the line profile and the Auger image or the Auger map. These modes use the direct spectrum to display the variation in element intensity over a line on the image or over the image as a whole. In the case of a line profile, a horizontal or vertical line can be defined on the scanning electron image. The number of pixels, i.e. the points of analysis, on that line can be defined and will range between 32 and 1024. The advantage of

this mode of analysis becomes clear when this is compared to the maximum number of spots, which is only 20. On every pixel, both peak and background intensity will be measured for all designated elements. Because it is too time consuming to obtain a split scan spectrum on every pixel and differentiate it in order to obtain the intensities, only the peak and background intensity are acquired. The peak position has to be defined after acquisition of a spectrum, as well as the background position, which is defined as the point on the right side of the peak where the intensity is locally minimal. In figure 2.5 (top), 1390 eV and 1406 eV can be defined as the peak and background positions of Al. If only the intensity at the peak position (*P*) would be measured and displayed, local variations in topography like surface roughness and surface inclination would lead to changes in intensity. Therefore, the intensity at the background position *(B)*, which has the same topographic dependence as *P*, is measured as well. The ratio *(P-B) / B* is displayed, minimizing the influences of topography in the case of homogeneous specimen compositions. Furthermore, when line profiles of several elements are acquired and one element shows higher intensities on places where the other element yields lower intensities, in most cases topographic variations can be ruled out as a physical cause.

The Auger image is obtained in a similar way, but instead of defining a line on the scanning electron image, the whole image is scanned. The number of pixels now ranges from 32×32 to 1024×1024. Usually, 128×128 or 256×256 pixels are selected, with an acquisition time ranging between one and 16 hours, depending on the dwell time, the counting time per point. Ultimately, the lateral resolution of the Auger image is limited by the spatial resolution of the electron probe (~15 nm). As an example, figure 2.9 shows Auger images of O, Al and Mg, acquired on the surface shown in the scanning electron image in the top left corner, after heating and oxidation at 520° C. The bar on the right side of an Auger image indicates which greyscales correspond to high and low intensities. Clearly visible are the higher O and Mg intensities on the right side of the image (the β-phase) and the higher Al intensity at the left side, the Al(Mg) phase.

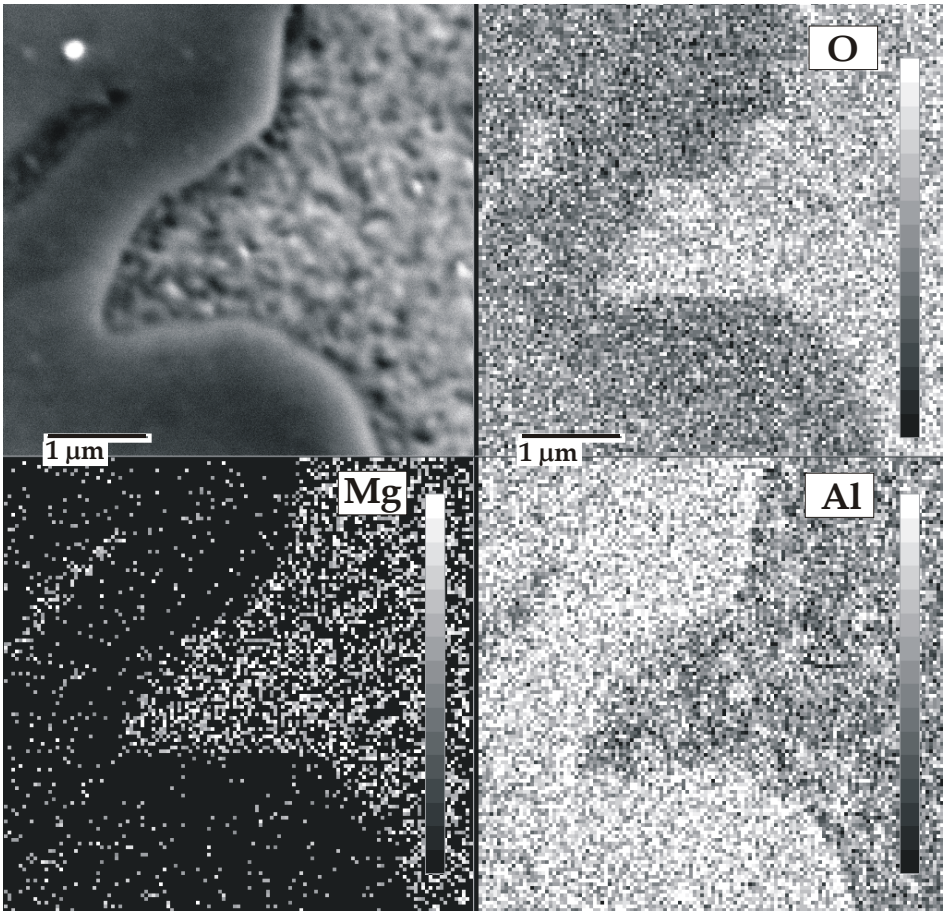

Figure 2.9: *Scanning electron image of an Al-Mg alloy surface and scanning Auger images of O, Mg and Al, displaying (P-B) / B*

2.4.3 Depth profiling by inert ion sputtering

Depth profiling is an additional mode of analysis. It will be treated separately because ion sputtering is also used to remove surface contaminants and it comprises the use of an extra component, namely the ion gun. The ion gun is an electrostatic device where the inert gas ions are generated by collisional excitation with electrons of typically 100 eV energy from a hot filament [39]. This takes place in an ionization chamber that is pumped by the turbomolecular pump and, through a small aperture, by the sputter ion pumps attached to the analysis chamber. The Ar^+ ions are accelerated to energies between 1 and 3 keV by means of an emission aperture under a negative potential and are focused using electrostatic lenses. Furthermore, the emission aperture acts as a differential pressure stage. The pressure in the analysis chamber rises from ~$5 \cdot 10^{-8}$ Pa to ~$1 \cdot 10^{-5}$ Pa during sputtering. However, the purity of the argon is such that no extra contaminants are introduced in the analysis chamber. The

focused ion beam is rastered over a large area (typically in the order of 400×400 μm), which greatly improves the uniformity of the ion beam density [40] and leads to a flat bottom of the sputter crater, which is necessary for optimum depth resolution. For optimum results it is necessary that the electron beam is much smaller than the size of the sputter crater and is focused in the center of the crater, where the sputter rate is well defined and constant. In our instrument, with spot sizes of ~ 15 nm to a few microns at most, this condition is easily fulfilled. Depending on the accelerating voltage, the measured positive currents on the specimen range between 0.5 μA for 1 keV to 1.6 μA at 3 keV. The sputter rate is determined by removing a well defined, 100 nm thick SiO_2 layer on a Si substrate and monitoring both Si and O intensities. The measured sputter rates range from 3.3 to 20 nm/min and will be stated when describing the experiments. However, the sputter rates are valid for SiO_2 only and vary with the sputtered elements, depending on the sputter yield. Therefore, in most cases the sputter times of different experiments are compared to gain information about relative depths, while the absolute values of the sputter depths remain uncertain.

A depth profile consists of alternating periods of ion sputtering and obtaining 'split scan' spectra. In this way, the variation of the element intensities with sputter depth is obtained. The intensity that is plotted in intensity versus sputtering time diagrams is the difference between the maximum and minimum of the differential spectrum in a particular region of interest. Therefore, care has to be taken that this corresponds to the actual peak maximum and minimum.

There are several factors that limit the accuracy of depth profiles and the depth resolution. For instance, redeposition of sputtered species can occur, which can lead to a memory effect of the original surface composition. The original surface roughness has an effect on the depth resolution, because ion sputtering changes the surface roughness as well. It is advisable to start with a surface that is as smooth as possible. During ion sputtering of alloy surfaces, preferential sputtering of one of the constituents is very likely. This is illustrated by figures 2.4 and 2.9, which display a surface that was sputtered for long periods. The Mg-rich β-phase has a rough appearance, compared to the Al(Mg) phase. Mg has a larger sputter yield than Al [41], which leads to Al surface enrichment after sputtering. Therefore, any observed Mg surface enrichment cannot be caused by preferential sputtering.

An example of a depth profile is given in figure 2.10. First, the surface of the Al-Mg alloy is cleaned by sputtering with 3 keV Ar^+ ions, with a sputtering rate of 15 nm/min on SiO_2. The oxide layer that is formed on the Al-Mg samples during the preparation stages, due to exposure to atmospheric conditions, is easily removed by Ar^+ sputtering. Then, the alloy is heated and thereby oxidized at 520° C. After that, the depth profile of figure 2.10 is obtained on the Al(Mg) phase. In figure 2.10, the ratios of measured peak-to-peak heights, I_O/I_{Al} and I_{Mg}/I_{Al} are shown, to reduce the effects of topography on the displayed intensities.

It is clearly visible that the oxidation of the surface is accompanied by an enrichment of Mg. The depth profile of the β-phase after heating to 520° C is shown in figure 2.11. A comparison between figures 2.10 and 2.11 indicates that both the intensity ratios at the surface and the depths over which O and Mg are enriched are similar for both phases. However, I_{Mg}/I_{Al} is different for the two phases after the removal of O, because the 'bulk' Mg content is different. This means that the relative surface enrichment of Mg is higher in the Al(Mg) phase than in the β-phase. However, at temperatures lower than 300° C the Al(Mg) surface does not show significant Mg enrichment, whereas the β-phase shows an increase in I_{Mg}/I_{Al} ratio from ~0.2 to ~0.3 upon heating to 200° C and to ~0.35 at 300° C, with a slightly thinner oxide layer than at 520° C[38].

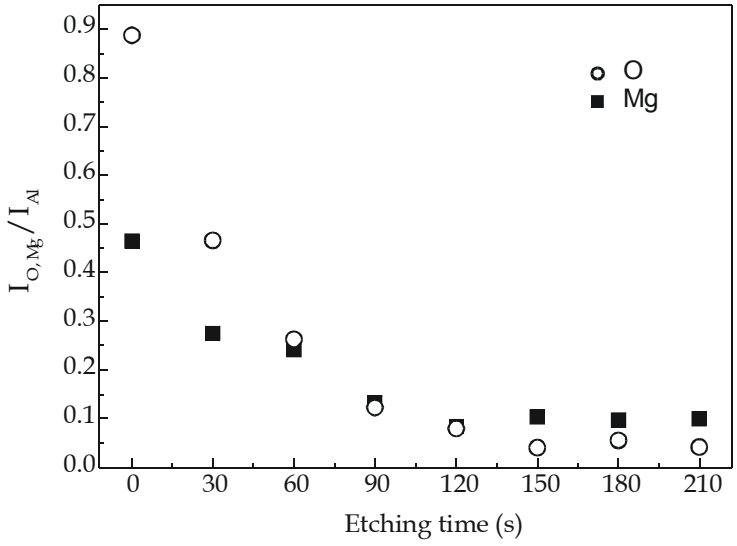

Figure 2.10: *Depth profile of an oxidized Al(Mg) surface, using minimum beam size (~ 15 nm)*

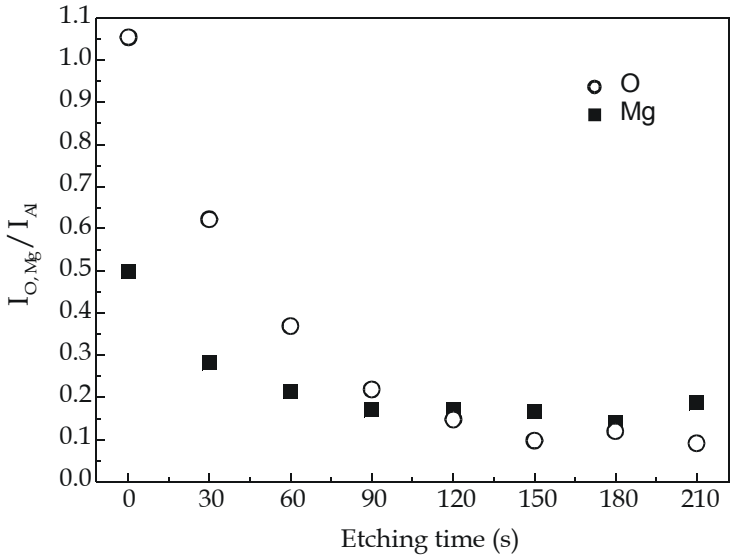

Figure 2.11: *Depth profile of an oxidized surface of the β-phase*

2.4.4 Discussion

It can be concluded that the presence of Mg significantly enhances oxidation, which is also in agreement with the fact that Mg has a higher affinity to oxygen compared to Al. The heat of formation of Al_2O_3 is 1113.6 kJ/mol, while that of MgO is 1202.2 kJ/mol [42]. The increasing amount of Mg at the surface with increasing temperature can be explained from the fact that Mg preferentially segregates to the surface, under the influence of the present oxygen. In the β-phase, significant Mg segregation is possible at lower temperatures than in the Al(Mg) phase, because of the large number of structural vacancies present in that phase, which facilitates diffusion.

In commercial Al-Mg alloys with low Mg content, Mg can segregate to grain boundaries, where it can lead to the precipitation of Al_3Mg_2. Previous experiments showed that the phase initially formed at triple points and then along the grain boundaries [43]. The presence of this phase in an Al-Mg alloy is potentially harmful, because of the faster formation of magnesium rich, brittle oxides.

2.5 QUANTIFICATION OF AUGER SPECTRA

The earliest attempts to quantify the amounts of materials through an obtained Auger spectrum naturally made use of the differential spectrum, because of the clarity of the peaks and the ease of defining the peak-to-peak heights. It is valid to use the peak-to-peak heights as measures for I_A and I_A^∞ [2], where I_A is the measured intensity of an element during analysis and I_A^∞ is the intensity of that element measured on a pure standard specimen, if three conditions are fulfilled. The same differentiating algorithm has to be used, the analyzers for both spectra must have the same resolution and the peak shapes have to be the same in both analysis and reference spectra. The first two conditions are easily fulfilled by always using the standard differentiating algorithm provided with the JAMP 7800F and the same analyzer resolution. The third condition can be achieved for metallic alloys if all experiments are performed on the same instrument. However, due to changes in the chemical environment the peak shapes may change. For example, surface oxidation can lead to an energy shift of the peak, a change in peak shape and therefore a change in peak-to-peak height. In most experiments described in the next chapters, surface oxidation is limited and in the studies on electron beam enhanced oxidation quantification is not attempted. Therefore, in the next section the quantification of binary alloys using the differential spectra will be described.

The intensity of the signal from element A, I_A, is roughly proportional to the molar fractional content in the analysis depth, X_A. If the dependence would be linear, only the ratios of element intensities to their elemental standard intensities would be sufficient to calculate the concentrations in the volume of analysis. However, the intensities are also influenced by other factors such as backscattering terms, which vary when other elements are present as well. A correction with the so-called matrix factor is necessary. The Auger electron current of an element A may be expressed as

$$I_A \propto \int_0^\infty X_A(z) \exp\left[\frac{-z}{\lambda_M \cos\phi}\right] dz \qquad (2.12)$$

where $X_A(z)$ is the distribution of A atoms with depth z, λ_M the inelastic mean free path in the matrix M and ϕ is the angle between the surface normal and the Auger detector (the hemispherical analyzer). For a homogeneous binary

system, the integral becomes $X_A\ \lambda_M cos(\phi)$. If, for binary systems, the ratio of intensities I_A/I_B is used and compared with the ratio of pure element standards the number of unknowns can be reduced if all measurements are performed on the same instrument [2]. This leads to

$$\frac{X_A}{X_B} = F_{AB}^{A} \frac{I_A / I_A^{\infty}}{I_B / I_B^{\infty}} \tag{2.13}$$

In this equation, F is the matrix factor that is given by

$$F_{AB}^{A} = \left[\frac{1+r_A(E_A)}{1+r_B(E_A)}\right]\left(\frac{a_B}{a_A}\right)^{1.5} \tag{2.14}$$

In equation (2.14), $r_{A,B}$ is a backscattering term, which is energy dependent. However, the ratio r_A/r_B is not very energy dependent and therefore F may be considered being constant for a binary AB system. For ϕ = 30°, which resembles the settings of the JAMP 7800F, the backscattering term r was approximated by [44]

$$r = \left(0.46 - 0.78\,Z^{0.2}\right)U^{-0.32} + \left(1.15Z^{0.2} - 1.05\right); \qquad (\phi = 30°) \tag{2.15}$$

where Z is the atomic number and U the ratio of the energy of the primary electrons and the energy of the Auger transition. The remaining unknowns of equation (2.14) are a_A and a_B, which are defined by

$$a_m^3 = \frac{A_m}{1000\,\rho_m\,N} \tag{2.16}$$

where A_m is the atomic weight of the matrix atoms, ρ_m the density and N is Avogadro's number.

In this thesis, besides a homogeneous composition, two other configurations of elements are of importance. In the case of grain boundary or surface segregation, the enrichment can extend over one or several monolayers. When solute enrichment extends over more than one monolayer, a composition gradient with depth is usually present. The distribution of segregated atoms

with depth, $X_A(z)$, has to be known or estimated, after which it can be introduced in equation (2.12).

In the case of monolayer segregation, the signal of the substrate B covered by a fraction of a monolayer Γ_A of A is

$$I_B = I_B^{\infty}\left\{1-\Gamma_A+\Gamma_A \exp\left[\frac{-a_A}{\lambda_A(E_B)\cos\phi}\right]\right\} \tag{2.17}$$

The signal from the overlayer is

$$I_A = \Gamma_A\, I_A^{\infty}\left[\frac{1+r_B(E_A)}{1+r_A(E_A)}\right]\left\{1-\exp\left[\frac{-a_A}{\lambda_A(E_A)\cos\phi}\right]\right\} \tag{2.18}$$

Because of surface roughness and other influences on absolute intensities, it is necessary to use the ratio of intensities. From the ratio of intensities, the coverage Γ can be deduced, assuming that Γ is small and the Auger peaks are at high energy, where

$$\Gamma_A = m\, K_{AB}\frac{I_A}{I_B} \tag{2.19}$$

In equation (2.14), m is 1 for surfaces and 2 for grain boundaries because on average, half of the amount of segregant is retained on either boundary after intergranular fracture. For individual boundaries, this might not be the case and therefore this equation will be only used for averages of grain boundary intensities. K_{AB} is defined as

$$K_{AB} = \left[\frac{\lambda_A(E_A)\cos\theta}{a_A}\right]\left[\frac{1+r_A(E_A)}{1+r_B(E_A)}\right]\frac{I_B^{\infty}}{I_A^{\infty}} \tag{2.20}$$

The aforementioned equations will be used in the next chapters to estimate the amounts of elements present on the surfaces or former grain boundaries.

2.6 ORIENTATION IMAGING MICROSCOPY

Orientation Imaging Microscopy (OIM) can be used to gain information about several aspects of polycrystalline solids. Analyses that can be performed are on crystallographic textures, grain boundary misorientations, relations between different phases and, rather qualitatively, on strain. In our experiments, OIM is mainly used to obtain the misorientations between grains in polycrystalline materials. In order to discuss the concepts of this technique, it is necessary to explain the Coincidence Site Lattice (CSL) model that is used to classify grain boundaries [45,46]. This model uses the so-called dichromatic point group, which is formed by hypothetically allowing the lattices of two grains to interpenetrate. In figure 2.12, the lattice sites belonging to grain 1 are white and those belonging to grain 2 black. For certain misorientations, a new lattice of coincident black and white sites can be constructed. This is the lattice shown in figure 2.12 that connects the coincident sites, the black dots in a white circle. The parameter Σ is defined as the ratio between the volume of the CSL unit cell and the unit cell of the material. The density of coincident sites in space is equal to $1/\Sigma$, therefore figure 2.12 shows a $\Sigma = 5$ grain boundary in a simple cubic structure, projected along the [100] direction. Grain boundaries where a CSL and the parameter Σ can be defined are called special boundaries. It should be emphasized that the CSL is a rather mathematical construction and does not provide any physical information of the local atomic surroundings.

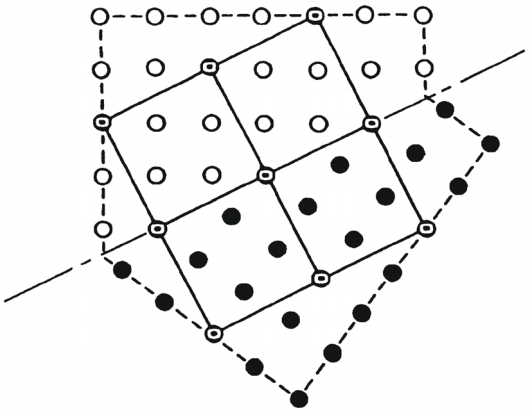

Figure 2.12: *Σ = 5 grain boundary constructed with a dichromatic pattern*

OIM is based on the automatic indexing of electron backscatter diffraction patterns (EBSP) from a specimen surface, which are produced in a Philips XL30F SEM. It gives information of the misorientations between grains in a polycrystalline specimen, classified according to the CSL model. However, the

CSL classification does not fully describe the grain boundary, i.e. the grain boundary plane is still unknown.

The system used to obtain and analyze OIM data is manufactured by TSL. Electron backscatter diffraction patterns are obtained in the SEM by focusing the electron beam on a crystalline sample. The specimen surface has to be smooth and the orientation of the surface region, from which the diffraction patterns are obtained, must be representative of the bulk of the grain. Therefore, the specimens are usually chemically etched before insertion to remove deformed surface layers. The specimen is tilted to approximately 70 degrees with respect to the horizontal. The diffraction pattern is imaged on a phosphor screen and the image is captured using a CCD camera. The Kikuchi bands in the diffraction pattern represent the reflecting crystallographic planes in the diffracting crystal volume. Thus, the geometrical arrangement of the bands is a function of the orientation of the crystal lattice. In this thesis, only experiments on specimens with known crystallographic structures are described. Therefore, the patterns can be compared with standard patterns to obtain the orientations of the grains, relative to the specimen.

In an OIM scan the beam scans the sample surface in a rectangular grid. At each step the EBSP is automatically indexed and the orientation is recorded, as well as the pattern quality of the EBSP, the image quality. As the beam is moved from grain to grain the electron backscatter diffraction pattern will change due to the change in the orientation of the crystal lattice in the diffracting volume. An image processing algorithm (Hough Transform) is used to detect bands in the diffraction pattern. Because the structure is known, the patterns can be indexed by comparing the angles between the detected bands to the theoretical table. A grain boundary map can be generated by comparing the orientation between each pair of neighboring points in an OIM scan. A line separating a pair of points is drawn if the difference in orientation between the points exceeds a given tolerance angle, which is normally 15°. In this way, points with similar misorientations are grouped into grains, with grain boundaries in between.

In the experiments described in this thesis, OIM is mainly used to correlate the grain boundary character distribution (GBCD) of a specimen with its mechanical properties. Some low Σ boundaries, like $\Sigma = 3$, have low energies and can be favorable with respect to mechanical properties, because they can be less susceptible to intergranular fracture.

REFERENCES

1. Hondros, M.P. Seah, Int. Met. Rev. **22** (1977) 262
2. M.P. Seah in Practical Surface Analysis, Vol. 1 (Eds. D. Briggs, M.P. Seah) John Wiley & Sons Ltd., Chichester, UK (1990)
3. J.O. Arnold, J. Iron Steel Inst. **45** (1894) 107
4. D. McLean, Grain Boundaries in Metals, Oxford University Press, London (1957)
5. D.F. Stein, L.A. Heldt in Interfacial Segregation (Eds. W.C. Johnson, J.M. Blakely) American Society for Metals, Metals Park, OH (1979)
6. M.P. Seah, J. Vac. Sci. Technol. **17** (1980) 16
7. W.P. Rees, B.E. Hopkins, J. Iron Steel Inst. **172** (1952) 403
8. E.D. Hondros, D. McLean, Monograph 28, Society of Chemical Industry, London (1968)
9. M.P. Seah, Acta Metall. **25** (1977) 345
10. E. Voce, A.P.C. Hallowes, J. Inst. Metals **73** (1947) 323
11. C.T. Liu, C.L. White, J.A. Horton, Acta Metall. **33** (1985) 213
12. J.R. Rice, J.S. Wang, Mat. Sci. Eng. A **107** (1989) 23
13. J.P. Hirth, J.R. Rice, Metall. Trans. **11A** (1980) 1501
14. H. Erhart, H.J. Grabke, Met. Sci. **15** (1981) 401
15. A.P. Sutton, R.W. Balluffi in Interfaces in Crystalline Materials, Oxford University Press, New York (1995)
16. E.D. Hondros, M.P. Seah, Metall. Trans. **8A** (1977) 1363
17. P. Wynblatt, R.C. Ku in Interfacial Segregation (Eds. W.C. Johnson, J.M. Blakely) American Society for Metals, Metals Park, OH (1979)
18. F.L. Williams, D. Nason, Surf. Sci. **45** (1974) 377
19. J.J. Burton, E.S. Machlin, Phys. Rev. Lett. **37** (1976) 1433
20. A.R. Miedema, Z. F. Metallkunde **69** (1978) 455
21. D. Tomanek, S. Mukherjee, V. Kumar, K.H. Bennemann, Surf. Sci. **114** (1982) 11
22. L.A. Harris, J. Appl. Phys. **39** (1968) 1419
23. L.A. Harris, J. Appl. Phys. **39** (1968) 1428
24. J.J. Lander, Phys. Rev. **91** (1953) 1382
25. P. Auger, J. Phys. Radium **6** (1925) 205
26. M.P. Seah in Proceedings of 9th International Vacuum Congress and 5th International Conference on Solid Surfaces (Ed. J.L. de Segovia) ASEVA, Madrid (1983)
27. S. Tanuma, C.J. Powell, D.R. Penn, Surf. Interface Anal. **11** (1988) 577
28. S. Hofmann, A. Zalar, Thin Solid Films **56** (1979) 337
29. S.A. Koch, D.T.L. van Agterveld, G. Palasantzas, J.Th.M. De Hosson, Surf. Sci. **476** (2001) L267

30. J.E. Hatch (Ed.), Aluminum: Properties and Physical Metallurgy, American Society for Metals, Metals Park, OH (1984)
31. F.J. Esposto, C.-S. Zhang, P.R. Norton, R.S. Timsit, Surf. Sci. **302** (1994) 109
32. G.C. Allen, P.M. Tucker, B.E. Hayden, D.F. Klemperer, Surf. Sci. **102** (1981) 207
33. K.J. Holub, L.J. Matienzo, Appl. Surf. Sci. **9** (1981) 22
34. G.R. Wakefield, R.M. Sharp, Appl. Surf. Sci. **51** (1991) 95
35. B. Goldstein, J. Dresner, Surf. Sci. **71** (1978) 15
36. A.A. Nayeb-Hashemi, J.B. Clarke (Eds.), Phase Diagrams of Binary Magnesium Alloys, American Society for Metals, Metals Park, OH (1988)
37. S. Samson, Acta Cryst. **19** (1965) 401
38. D.T.L. van Agterveld, G. Palasantzas, J.Th.M. De Hosson, Appl. Surf. Sci. **152** (1999) 250
39. S. Hofmann in Practical Surface Analysis, Vol. 1 (Eds. D. Briggs, M.P. Seah) John Wiley & Sons Ltd., Chichester, UK (1990)
40. H.J. Mathieu, D. Landolt, J. Micros. Spectr. Electron **3** (1978) 113
41. M.P. Seah, Thin Solid Films **81** (1981) 279
42. C. Jardin, D. Robert, Appl. Surf. Sci. **35** (1988) 495
43. J.S. Vetrano, D.R. Baer, R.H. Jones, in Automotive Alloys II, ed. S.K. Das, The Minerals, Metals and Materials Society, Warrendale, PA (1997) p.117
44. R. Shimizu Jap. J. Appl. Phys. **22** (1983) 1631
45. M.L. Kronberg, F.H. Wilson, Trans. Metall. Soc. AIME **185** (1949) 501
46. R.W. Balluffi, A. Brokman, A.H. King, Acta Metall. **30** (1982) 1453

Chapter 3

ELECTRON BEAM ENHANCED OXIDATION

3.1 INTRODUCTION

Electron irradiation of a surface has been observed to stimulate surface oxidation [1,2]. In this thesis, this phenomenon is encountered during surface segregation studies with Auger electron spectroscopy of boron in Ni_3Al alloys, when the surface is exposed to the electron beam for longer periods. Attempts to probe the development of boron with time at the surface require the continuous acquisition of Auger spectra at several sites. This means that a site is exposed to the electron beam for a few minutes, after which the beam is moved to probe other sites before the electron beam returns to the first site again. These measurements lead to enhanced oxidation of the exposed sites, which has been previously observed for pure Ni surfaces under the influence of an electron beam. The areas that are exposed to the electron beam have a different, much brighter, appearance in secondary electron images than the non-exposed areas, where the observed oxide intensities in Auger spectra are smaller. In this chapter, a separate study is devoted to this surface phenomenon.

Oxygen adsorption and oxide formation on Ni_3Al were studied in the past [3-5]. At atmospheric pressure, NiO, $NiAl_2O_4$ and Al_2O_3 are the oxides that are formed on polycrystalline Ni_3Al surfaces [4,5]. In contrast, at low oxygen pressures under ultrahigh vacuum conditions the preferred oxide on these surfaces is Al_2O_3, with a structure that strongly depends on the adsorption temperature. On a Ni_3Al surface, ordered γ'-Al_2O_3 is formed after oxygen adsorption at 1000 K, irrespective of oxygen dose and sample preparation [3]. At this temperature, aluminum surface segregation is not hindered and it controls the formation of aluminum oxide at the surface.

At 300 K (RT), the situation is different. The temperature is too low for significant Al diffusion in the strongly ordered Ni_3Al. Therefore, the oxygen chemisorbs on nickel sites or mixed Ni/Al sites. The observed surface structure is disordered, leading to the conclusion that Al_2O_3 is not formed, although the oxygen starts to be incorporated with increasing oxygen exposure [3]. This was also confirmed by room temperature scanning tunneling microscopy (STM) studies [6,7], which indicated the formation of small oxide nuclei on Ni_3Al (111) surfaces and an oxide formation that is governed by the mobility of O atoms rather than by a substantial transport of metal atoms.

Contrary to pure Ni [8,9,10], the kinetics of the oxidation of Ni_3Al during simultaneous exposure to an electron beam has not been studied before. Fundamental and technological interests in the field of corrosion and catalysis have given an impetus to numerous investigations on the growth of oxide layers on pure Ni [11-14]. Furthermore, these studies are important for lithography techniques in microelectronic device fabrication [15], exchange-bias junctions [16] and aerospace technology [17,18]. Several of these studies have taken into account the electron stimulated oxidation that occurs under the influence of exposure to an electron beam [9,10]. Oxidation of Ni under the influence of an electron beam has been described by a model that assumes that the electron beam creates additional nucleation sites for oxidation [9]. The electron flux and an oxidation rate constant are the most important parameters of this model.

In this chapter, the kinetics of oxidation of Ni_3Al with and without B is recorded. Because electron beam enhanced oxidation is encountered during segregation studies on these alloys, but has been studied before on pure Ni, the oxidation kinetics of pure Ni and Ni with B in solid solution are recorded as well, in order to compare the present data with earlier work. The Auger intensities of oxygen and the other elements present are measured as a function of time. Different models for oxidation will be compared by confronting these to the experimental data. To test the influence of electron flux on the oxidation kinetics, electron beam current and beam size are varied.

Stoichiometric polycrystalline Ni_3Al and Ni_3Al-B are obtained from Highways International. The chemical compositions, weighed before melting, are 75 at.% Ni, 25 at.% Al for the specimens without boron and 74.7 at.% Ni, 24.8 at.% Al and 0.5 at.% B for the specimens containing boron. These specimens are cylindrically shaped and, after notching, ready for in situ fracture. Flat, polished

specimens of this material are used as well to reduce topographic effects. Furthermore, pure Ni (99.999 at.%) and Ni- 9 at.% B (manufactured through arc melting of the pure constituents) specimens are used. These specimens are flat and are not fractured in situ before oxidation. The specimens are inserted into the analysis chamber of the JEOL JAMP 7800F, where the oxidation experiments are executed. The flat, polished specimens are sputter cleaned by 3 keV Ar^+ ions in the analysis chamber of the JAMP 7800F before oxidation.

3.2 THE OXIDATION MODEL

Electron beam enhanced oxidation of pure Ni proceeds through a fast chemisorption stage, followed by rapid oxidation and, finally, by a very slow thickening of the saturated nickel oxide layer, with a saturation thickness of 3 monolayers of NiO [8]. In figure 3.1 the development of the Ni and O peak-to-peak heights with time on a pure Ni specimen is shown. Three sites are exposed sequentially, meaning that during a cycle each site is exposed to the electron beam for three minutes interrupted by six minutes of non-exposure, after which the cycle is repeated. The spot size of the beam is 5 μm, with an accelerating voltage of 10 keV and a primary electron beam current of 2.4 nA. Oxygen is provided by residual gases in the UHV environment of the JEOL JAMP 7800F and therefore the exact partial pressure of oxygen is unknown. Remarkably, the measured intensities of carbon are very low and do not increase during exposure.

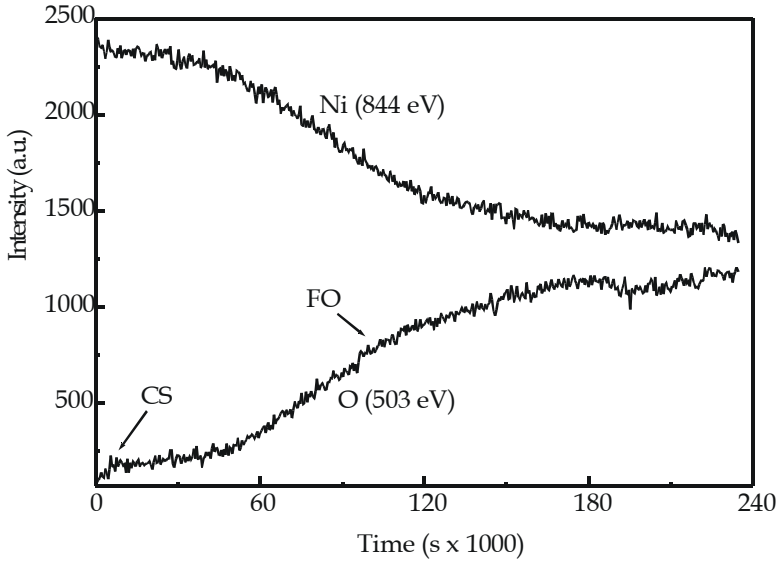

Figure3.1: *Evolution of Ni and O intensities with time on pure Ni*

Clearly visible in figure 3.1 are the fast increase during the first $1 \cdot 10^4$ s (chemisorption stage, CS), the slowly increasing intensity afterwards and the fast increase between $3 \cdot 10^4$ and $1.5 \cdot 10^5$ s, the fast oxide growth regime (FO). Due to the coverage of oxygen, the Ni intensity decreases simultaneously with the increase of O.

The oxidation of Ni has been described in the past by various oxide growth models, which will be the starting point in this section. The island growth oxidation model [8,11,14] assumes lateral growth of oxide islands which depends on various parameters such as the number of initial nucleation sites, the collision rate of O molecules/atoms with the substrate, as well as the rate constant K_1 for perimeter growth of the oxides. Another model, developed by Zion et al. [11], termed as the Langmuir model, is based on the assumptions that the oxidation growth rate depends on the impingement rate of oxygen molecules, Langmuir oxide coverage, and a rate constant. For both models, the O coverage Θ can be described as a function of exposure Φ, from the onset of the fast oxide growth regime

$$\Theta(\Phi) = \Theta_{\mathrm{sat}} - (\Theta_{\mathrm{sat}} - \Theta_{\mathrm{chem}}) \exp[-K_c (\Phi - \Phi_o)^c] \qquad (\Phi > \Phi_{\mathrm{o}}) \tag{3.1}$$

with Φ the O exposure (Langmuir), K_c an oxidation constant, Θ_{chem} the coverage at chemisorption saturation (monolayers), Θ_{sat} the saturation coverage (monolayers) and Φ_0 the oxide onset exposure [8,11,14]. The island growth model has a second order dependence on Φ, $c = 2$ (growth rate dependence on island perimeter), whereas the Langmuir model has a first-order dependence on Φ, i.e. $c = 1$. Both models do not explicitly include electron beam effects. Wei Li et al. [9] proposed a model for electron beam induced oxidation that assumes that incident electrons create additional nucleation sites where oxide growth takes place. Because this model describes oxidation of a surface with chemisorbed oxygen (not more than one monolayer) already present, the electron beam probably induces in-depth oxide growth. Therefore, more than one monolayer can form upon beam irradiation. The oxide nucleation sites probably are some type of electron rich site similar to F-center anion vacancies created by sputtering a NiO surface [10]. The number of nucleation centers, N, created by the electrons follows a first order rate law

$$\frac{dN}{dt} = (N_0 - N)\, \phi_e\, \sigma \tag{3.2}$$

where N_0 is the saturation number of nucleation centers, ϕ_e the electron flux (in electrons per m^2 per second) and σ is the cross section for the creation of nucleation centers by the electron beam. The rate of oxide growth on nickel can then be described as

$$\frac{d\theta}{dt} = k(\theta_{sat} - \theta)\frac{N}{N_0} \tag{3.3}$$

where θ is the oxide coverage, θ_{sat} saturation coverage, t the exposure time and k the rate constant for oxide growth around the nucleation centers. Integration of both equations leads to

$$\Theta(t) = \Theta_{sat} - (\Theta_{sat} - \Theta_{chem})\exp[-kt - (k/\varphi_e\sigma)(\exp(-\varphi_e\sigma t) - 1)] \tag{3.4}$$

with the condition that $\theta = \theta_c$ at $t = 0$, i.e. this model describes the oxygen evolution at a surface where the chemisorption stage is already finished. This model is applicable for the description of the oxidation growth regime of pure Ni, i.e. from the onset of the steep rise in figure 3.1, after $3 \cdot 10^4$ s. Figure 3.2 shows the evolution of oxygen with time on pure Ni, in the regime of oxidation growth. A fit to the data using equation (3.4) is shown as a solid line in figure 3.2.

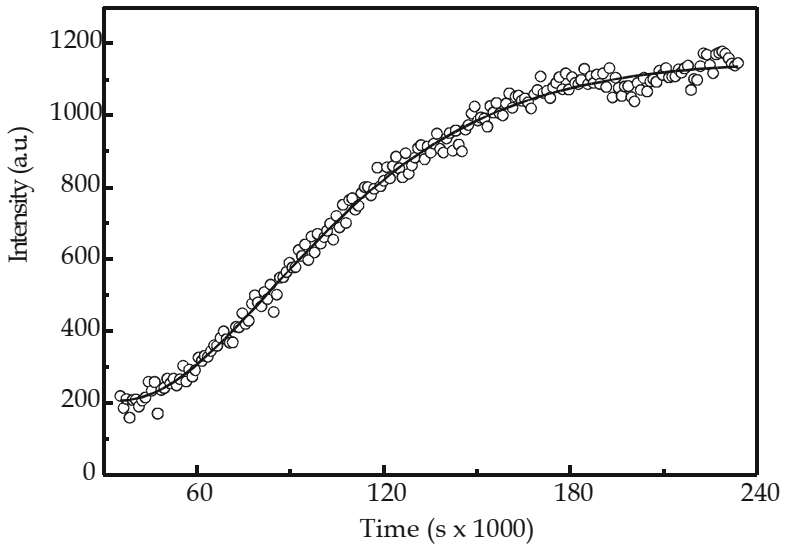

Figure 3.2: *Evolution of O intensity with time on pure Ni (circles) and fit to the data (line)*

It can be seen that the model of Wei Li et al. provides a good description of the kinetics of electron beam enhanced oxidation of pure Ni. The regions that are

not exposed to the electron beam show oxygen intensities that do not exceed the chemisorption intensities, i.e. the intensities that are measured in the first $3 \cdot 10^4$ s in figure 3.1.

3.3 OXIDATION OF Ni_3Al, Ni_3Al-B AND Ni(B)

Electron beam enhanced oxidation of Ni_3Al-B occurred during attempts to monitor the development of B at the surface. The electron beam enhanced oxidation hinders the observation of the B surface segregation, but enables the study of the oxidation kinetics of Ni_3Al at room temperature in an environment with a low oxygen partial pressure. Besides in situ fractured specimens, polished cross sections of Ni_3Al-B are exposed to the electron beam as well. Prior to oxidation the surface is cleaned by means of Ar^+ bombardment. Cleaning is necessary to remove the contaminants present at the surface, but it leads to a Ni-rich surface due to preferential sputtering of Al [19]. On a polished, cleaned Ni_3Al-B surface three sites are exposed subsequently, leading to the three bright spots that can be observed in the SE image in figure 3.3 (left). Figure 3.3 (right) shows the Auger intensity map of oxygen, which clearly reveals the local increase in oxygen intensity. The used beam spot size is 10 μm, which is the size of the bright spots, and the beam current is 2.4 nA. The Auger intensity map displays the ratio *(P-B) / B*, where *P* is the intensity at the peak position of oxygen in the spectrum and *B* is the background intensity at the right side of the peak in the direct spectrum.

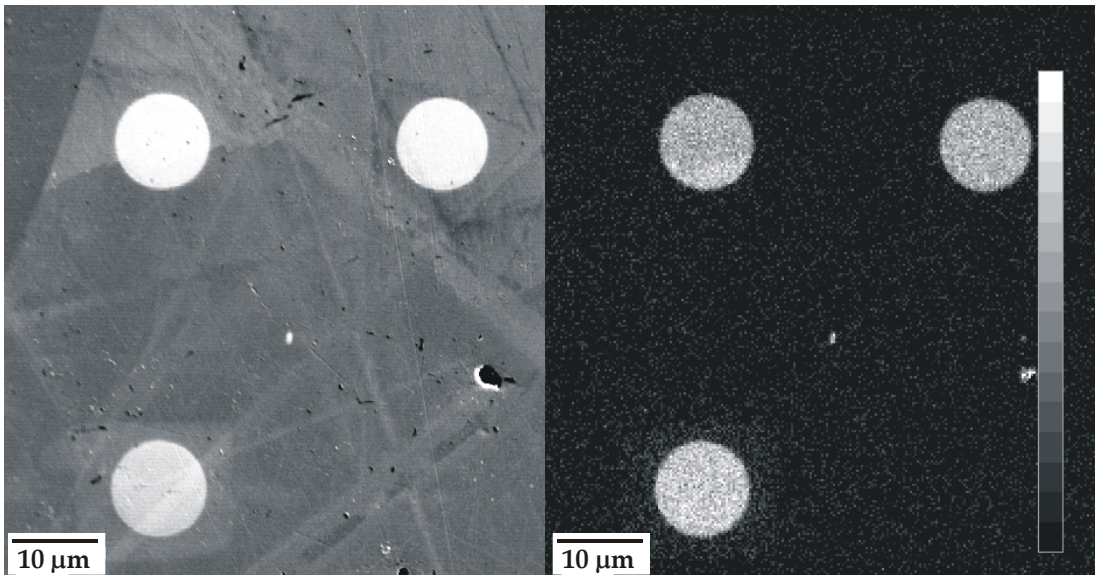

Figure 3.3: *Scanning electron (left) and scanning Auger (right) microscopy images of three oxidized sites on a Ni_3Al-B surface*

The evolution of the observed oxygen intensity is shown as circles in figure 3.4. The difference in oxidation behavior with pure Ni can be discerned immediately, namely the absence of a well defined, separate, chemisorption regime. The fast oxide growth stage immediately starts, surpassing the chemisorption stage. Chemisorption does occur during the first oxidation cycles, but is almost impossible to distinguish due to the simultaneous fast oxide growth. However, when a numerical fit using the model of Wei Li et al. is performed, it can be seen to deviate slightly in the first cycles only (squares in figure 3.4). The model is developed for pure Ni with a completed chemisorption stage; therefore the fit shows the positive curvature in the first cycles that is seen at the onset of fast oxide growth in pure Ni. The chemisorption stage is characterized by a negative curvature. The data in figure 3.4 show an almost straight line at the onset due to simultaneous chemisorption and oxide growth. The fit yields $1/k_{Ni_3Al-B}$ = 1.9·10^4 s and $\varphi_e\sigma$ = 2.2·10^{-4} s^{-1}. Furthermore, fits to the data were performed using equation (3.1) (Langmuir and island growth model), with c as a variable parameter. The best fit to the data is depicted in figure 3.4 as a solid line. This yields a characteristic exponent c = 1.23 ± 0.02. Based on these fitting results the island growth model is disregarded, because fitting with exponent c = 2 does not yield adequate fits. Fitting with exponent c = 1 leads to only minor deviations, which is reasonable because the oxidation data (circles) in figure 3.4 almost form a simple exponential curve.

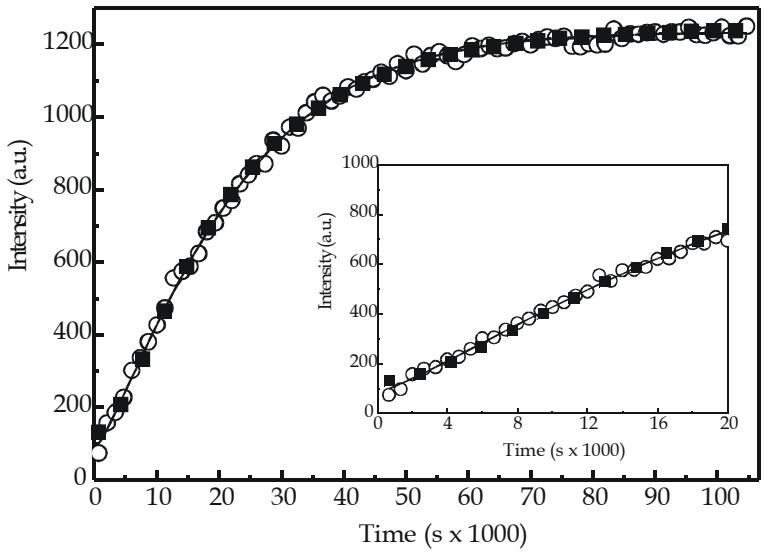

Figure 3.4: *Evolution of oxygen on Ni_3Al-B, averaged over three spots of 10 μm (circles). The solid line represents a fit with equation (3.1) and the squares refer to the model of Wei Li et al.*

Figure 3.5 shows similar data for oxidation of an undoped Ni_3Al surface. The fit yields for undoped Ni_3Al: $1/k_{Ni_3Al}$ = 1.8·10^4 s and $\varphi_e\sigma$ = 2.5·10^{-4} s^{-1}. The fit with

equation (3.1) yields a characteristic exponent c = 1.27 ± 0.03. The obtained values for undoped and doped Ni_3Al do not differ much from each other, yet oxidation of an undoped surface seems slightly faster than a boron doped surface.

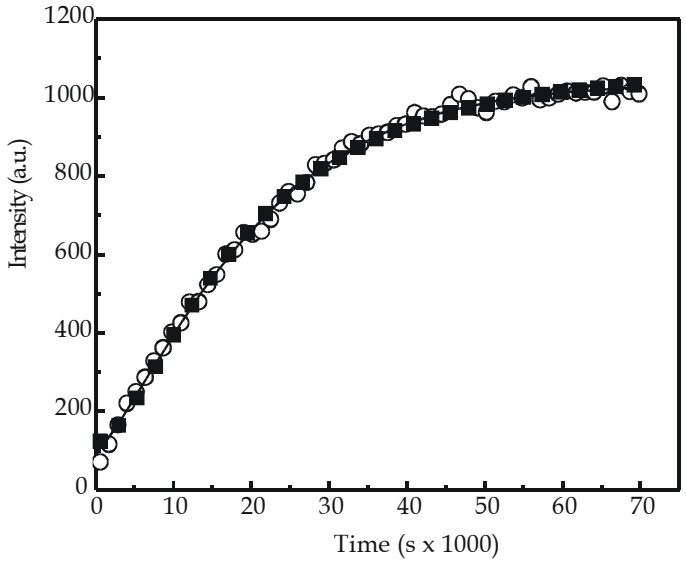

Figure 3.5: *Evolution of O intensity on Ni_3Al, averaged over three spots of 10 μm (circles). The solid line is a fit with equation (3.1), the squares represent the fit by the model of Wei Li et al.*

From the values obtained for $\varphi_e\sigma$ the cross-sections for the creation of oxide nucleation centers may be estimated. The beam current used in all previous oxidation experiments is 2.4 nA, which yields $\varphi_e = 1.9 \cdot 10^{20}$ electrons/m^2·s, for a spot size of 10 μm. For Ni_3Al-B, a cross section of $1.1 \cdot 10^{-24}$ m^2 is obtained, whereas for Ni_3Al the obtained cross section is $1.3 \cdot 10^{-24}$ m^2.

Compared to pure Ni, the oxidation process of Ni_3Al is much faster and, as a result, the obtained cross section for the creation of nucleation centers for pure Ni is orders of magnitude smaller. The fit in figure 3.2 yields for pure Ni: $1/k_{Ni} = 3.1 \cdot 10^4$ s and $\varphi_e\sigma = 1.3 \cdot 10^{-5}$ s^{-1}, which corresponds to a cross section of $1.7 \cdot 10^{-26}$ m^2, using the same beam current and a spot size of 5 μm. Although these values are much smaller than those for pure Ni held at 120 K ($3 \cdot 10^{-21}$ m^2) [9], an adequate comparison is difficult. In that same study a large difference was found between low temperature oxidation, where the electron beam effect was much more pronounced, and room temperature oxidation, where the difference between oxidation of exposed and non-exposed surfaces was negligible [9]. However, adsorption of CO and CO_2 onto a Ni(110) surface was observed to be strongly influenced by electron bombardment, at room temperature (20). In our study, it is unknown how the oxidation itself takes

place, but it is most likely due to dissociation of oxygen containing molecules such as H_2O, which are present in the UHV atmosphere. Therefore, probably the oxide nucleation sites are some type of electron rich site similar to F-center anion vacancies created by sputtering a NiO surface. These sites have shown evidence of dissociative adsorption of molecular O_2[10]. The partial pressure of oxygen in the vacuum chamber may be limiting the process, obscuring the calculation of the cross section.

In figure 3.6, the development of the intensities for all elements present, B, O, Ni and Al, is shown. The large decrease of the Ni intensity accompanied by the increase of O is striking and resembles the oxidation of pure Ni. However, what has to be taken into account is that the surface is Ar^+ bombarded and therefore Ni-rich. Estimations of the quantity of Ni in the outermost atom layer yield, using the ratio of sputter yields [19], concentrations of 82 at.% or more. Therefore, the attenuation effect of oxygen on top of the surface will be the highest for Ni. This effect is amplified by the larger inelastic mean free path (IMFP) of Al Auger electrons. Calculated IMFPs in pure Ni show that Al (1390 eV KLL) electrons have an IMFP of ~ 1.9 nm, whereas that of Ni (842 eV KLL) electrons is ~1.3 nm [21]. Because the Al signal can originate from deeper inside the material, the attenuation effect of a chemisorbed element at the surface on the intensity will be less. Figure 3.6 shows a fast, albeit small decrease in Al intensity in the first cycles, after which it stabilizes.

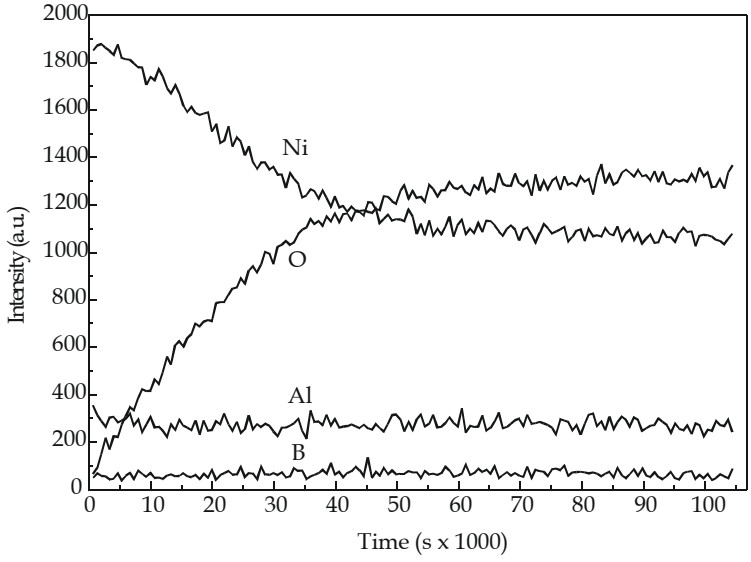

Figure 3.6: *Evolution of the intensities of B, O, Ni and Al*

Contrary to pure Ni, the fast oxide growth starts immediately and is accompanied by a decrease in Al intensity. On elements with a high oxygen

affinity such as pure Al (111) [22] and Mg (0001) surfaces [23], oxide nucleation is observed before the saturation of chemisorption is reached.

This leads to the conclusion that the participation of Al in the oxidation process of Ni_3Al(-B) is rather indirect, compared to high temperature oxidation, where Al can segregate and O can diffuse inwards, leading to Al_2O_3 formation. At room temperature, Al atoms at the surface are immediately covered with oxygen and due to the presence of Al the fast oxide growth starts immediately. However, the most drastic effect of the oxygen coverage is on the Ni intensity, because most of the atoms at the surface are Ni and the oxygen incorporation, without structural changes, only comprises a few atomic layers [8].

As a master alloy for the preparation of Ni_3Al-B, an alloy of Ni-9 at.% B is made by arc melting. The amount of B is far beyond the solubility limit in Ni (~0.1 at.%), which means that the alloy will decompose into two phases, Ni_3B and Ni with B in solid solution, Ni(B). A secondary electron image and Auger map of B are shown in figure 3.7.

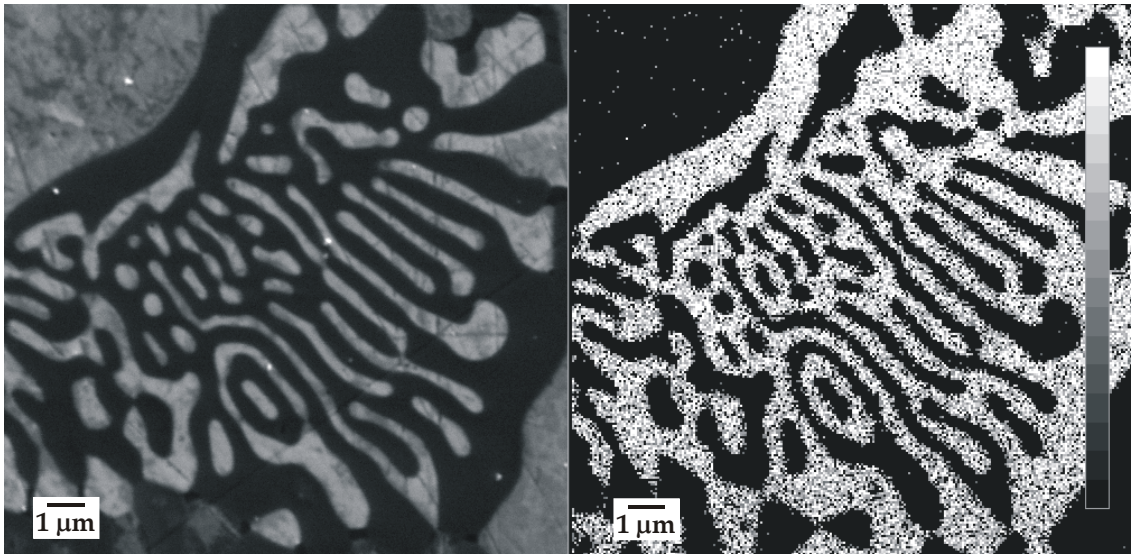

Figure 3.7: *SE image of the Ni-B alloy (left) and Auger map of B (right)*

From the Auger map it is clear that the dark regions in the SEM image correspond to the Ni_3B phase. During the acquisition of the Auger map, the Ni(B) surfaces are oxidized by the electron beam, whereas the Ni_3B surfaces show only minimal oxygen intensities after exposure to the electron beam. The observed oxygen intensities are, relative to the nickel intensities, comparable to the observed intensities on pure Ni after saturation of the chemisorption regime. Ni_3B therefore seems more resistant to electron beam enhanced

oxidation. Figure 3.8 shows the kinetics of the oxidation of the Ni(B) phase, after ion cleaning, with a beam size of 5 μm and a beam current of 2.4 nA.

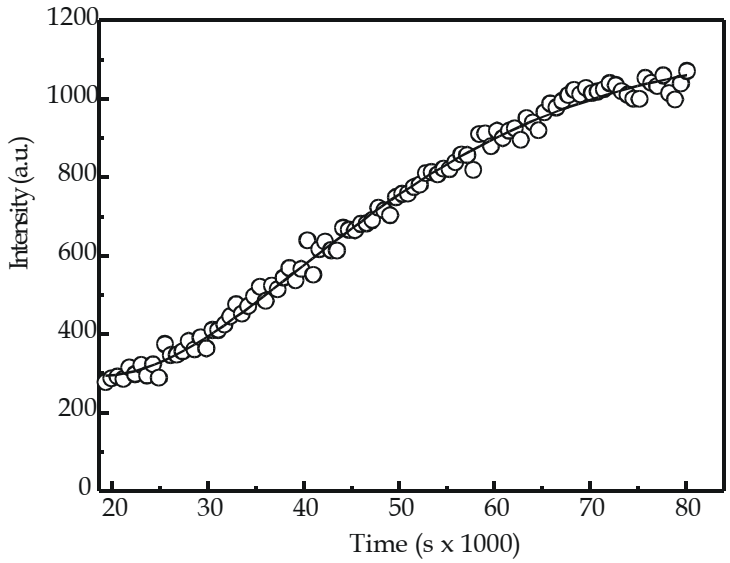

Figure 3.8: *Development of oxygen intensity with time on Ni(B)*

It is clear from figure 3.8 that the development of the oxygen intensity on Ni(B) is similar to that on pure Ni. The presence of boron is causing the process to occur faster, but the oxygen curve retains its characteristic S-shape. The obtained values for the constants in equation (3.4) are: $1/k_{Ni(B)}$ = $2.0 \cdot 10^4$ s and $\varphi_e \sigma$ = $2.8 \cdot 10^{-5}$ s^{-1}, which means that the process is faster than on pure Ni and slower than on Ni_3Al, with accompanying larger and smaller cross-sections for oxidation, respectively.

Figure 3.9 shows a more detailed image of the chemisorption regime in Ni(B). The oxidation curve follows the characteristics of exponential growth, as described by Holloway and Hudson [8]. The line in the figure is an exponential fit to the data, according to

$$I = C(1 - \exp(-k_{ch} t)) \tag{3.5}$$

where C is the intensity at the saturation of chemisorption. This yields a characteristic time of $1/k_{ch}$ ~ $4.5 \cdot 10^3$ s, which shows that the kinetics of the chemisorption regime is faster than the oxide growth regime.

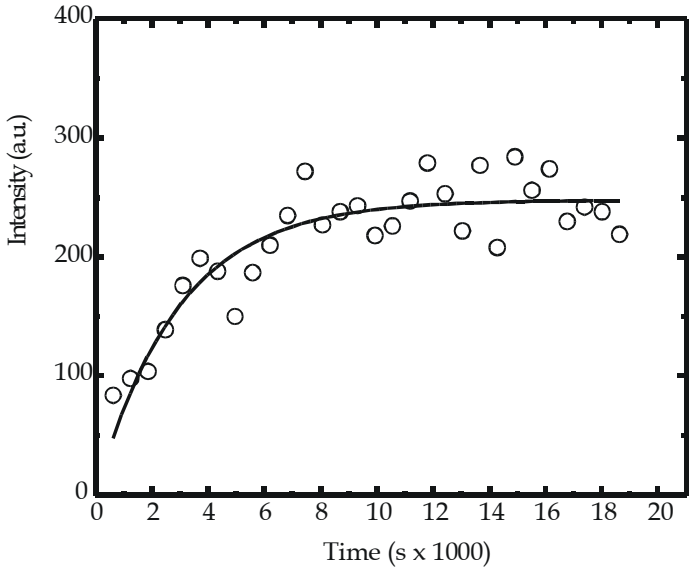

Figure 3.9: *The chemisorption regime in Ni(B)*

3.4 FLUX EFFECTS ON ELECTRON BEAM ENHANCED OXIDATION

One of the most important variables in the model of Wei Li et al. is the incident electron flux. In order to validate this model, a Ni_3Al-B surface is again oxidized, but with different electron fluxes for the different sites. The JEOL JAMP 7800F can vary its beam spot size in discrete steps of 5 μm. Because the primary beam current is always the same during one measurement, the electron flux varies and different sites are oxidized simultaneously with different fluxes. Because beam size and current are known, the flux can be easily calculated.

Figure 3.10 shows the evolution of oxygen peak-to-peak heights during electron beam enhanced oxidation. The six sites of diameters 5, 10, 30, 50, 70 and 100 μm are exposed sequentially every cycle. The beam current is 2.4 nA.

For reasons of clarity, the data for 10 μm are omitted, because they closely resemble the 5 μm data. From figure 3.10, the strength of the Wei Li model becomes clear. The data for 5 and 10 μm can be reasonably fitted with the Langmuir model, because both curves approximately follow a simple exponential behavior. However, for smaller electron fluxes, the curve shapes clearly deviate from a simple exponential form. The data for 5 μm are accompanied by a fit of the Wei Li model, which adequately describes the kinetics. The larger spot sizes (lower fluxes) are characterized by slower oxidation and, eventually, less oxygen intensity. This is confirmed by the Auger

map of oxygen for these six sites (figure 3.11), which shows high intensities for the smaller spots and lower intensities for the larger spots.

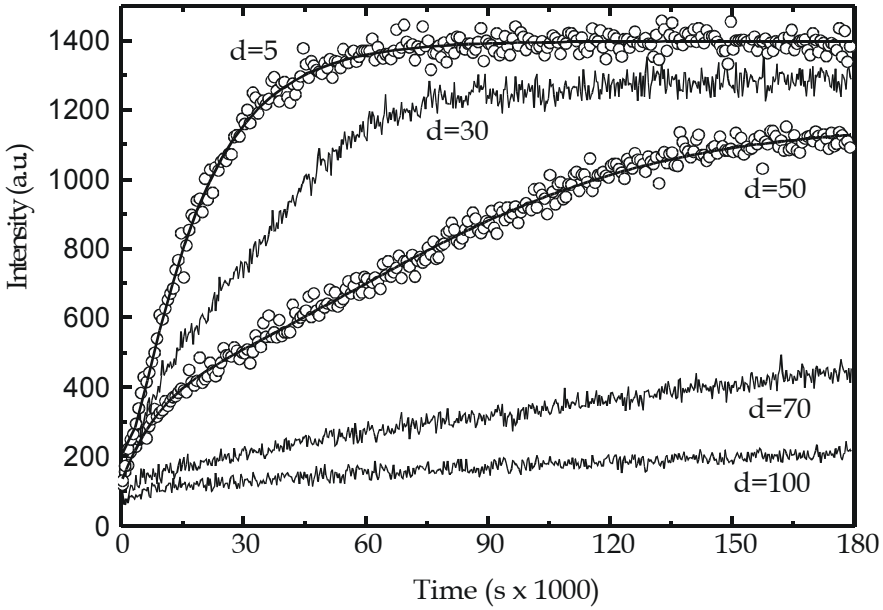

Figure 3.10: *Evolution of oxygen peak-to-peak heights for different beam sizes (different fluxes)*

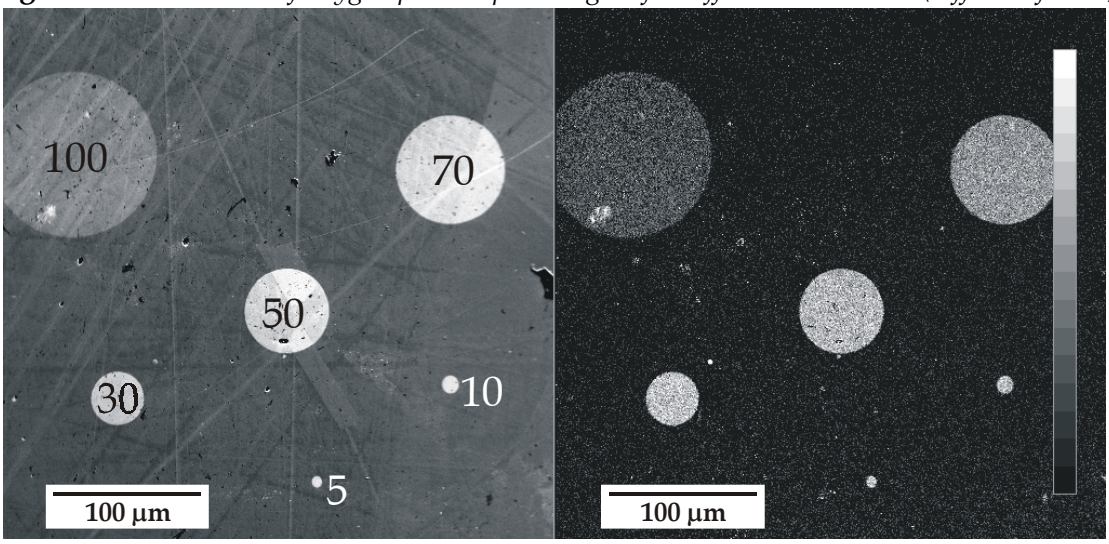

Figure 3.11: *SE image (left) and Auger map of oxygen (right) after electron beam enhanced oxidation with different beam sizes (µm). The dwell time was 100 ms, with minimum spot size*

When the incident electron flux becomes smaller, the chemisorption regime at the very beginning (first $1.0 \cdot 10^4$ s) can be distinguished again, like in pure Ni. In the curves for d = 50, 70 and 100 µm, becoming clearer with increasing spot size, the characteristic curvature of chemisorption in the first cycles can be seen. The fit using the Wei Li model will then deviate from the data, because it assumes a completed chemisorption stage. Therefore, an extra term is added to

equation (3.4) (of an exponential form [8]) to include the chemisorption regime and describe simultaneous chemisorption and oxide growth, which yields

$$I_O(t) = A - (A - B)\exp[-kt - (k/\varphi_e\sigma)\{\exp(-\varphi_e\sigma t) - 1\}] \; - C\exp(-k_{ch}t) \quad (3.6)$$

In this equation k_{ch} is a chemisorption reaction constant and the coverage Φ is rewritten as Auger intensity I (Φ and I are proportional for the first monolayer of O), which was used to obtain the fits to the measured intensities. Fits according to this equation are performed for both 30 and 50 µm but shown only for spot size d = 50 µm and are seen to reproduce the data in all oxidation stages.

The fitting parameters for the 5, 10, 30 and 50 µm spot sizes (for the larger spots the intensities do not reach saturation, which is necessary for a correct fit) are given in table 3.1.

Table 3.1: *Fitting parameters for the oxygen intensity curves of figure 3.10 with equation (3.6)*

d (µm)	A	B	C	$\varphi_e\sigma$ (s^{-1})	k (s^{-1})	k_{ch} (s^{-1})
5	1400	131	0	$7.5\cdot10^{-4} \pm 8.8\cdot10^{-5}$	$5.7\cdot10^{-5} \pm 8.2\cdot10^{-7}$	0
10	1357	157	0	$7.0\cdot10^{-4} \pm 8.2\cdot10^{-5}$	$4.8\cdot10^{-5} \pm 6.7\cdot10^{-7}$	0
30	1294	393	272	$3.0\cdot10^{-5} \pm 6.7\cdot10^{-6}$	$5.2\cdot10^{-5} \pm 4.3\cdot10^{-7}$	$2.2\cdot10^{-4} \pm 4.3\cdot10^{-5}$
50	1164	442	307	$7.8\cdot10^{-6} \pm 2.3\cdot10^{-6}$	$3.7\cdot10^{-5} \pm 3.8\cdot10^{-6}$	$1.0\cdot10^{-4} \pm 1.4\cdot10^{-5}$

From table 3.1 it can be seen that the chemisorption process occurs fast compared to the oxide growth, since $k_{ch} > k$. The fits to the 5 and 10 µm datasets are performed without the chemisorption term, therefore C and k_{ch} are zero. The fitting parameters of the 5 and 10 µm curves in table 3.1 are very similar, as are the curves themselves. Because there is a difference in electron flux from 5 to 10 µm, but not in $\varphi_e\sigma$, there seems to be a difference in cross section. However, for both 5 and 10 µm the term $\varphi_e\sigma$ is much larger than k, meaning that equation (3.4) will be mainly governed by $\exp(-kt)$ after a small period of time, for large fluxes. The oxidation curves will, besides a slight deviation in the first cycles, follow exponential behavior. Physically, this would mean that at sufficiently large electron fluxes the oxide growth rate is less dependent on the number of nucleation sites, which is large enough anyway, but mainly on the present oxygen partial pressure, which is very low in this case. Therefore, independent of the incident electron flux, the oxidation cannot proceed faster than at a certain rate. For smaller fluxes, the creation of nucleation sites is the rate limiting factor and the speed of oxidation decreases with decreasing flux. This will lead to inaccurate estimations of the cross sections at larger fluxes.

After oxidation of the sites in figure 3.11, a depth profile of oxygen is obtained, with a sputtering rate of ~0.15 nm/min, calibrated with respect to SiO_2. The results are shown in figure 3.12.

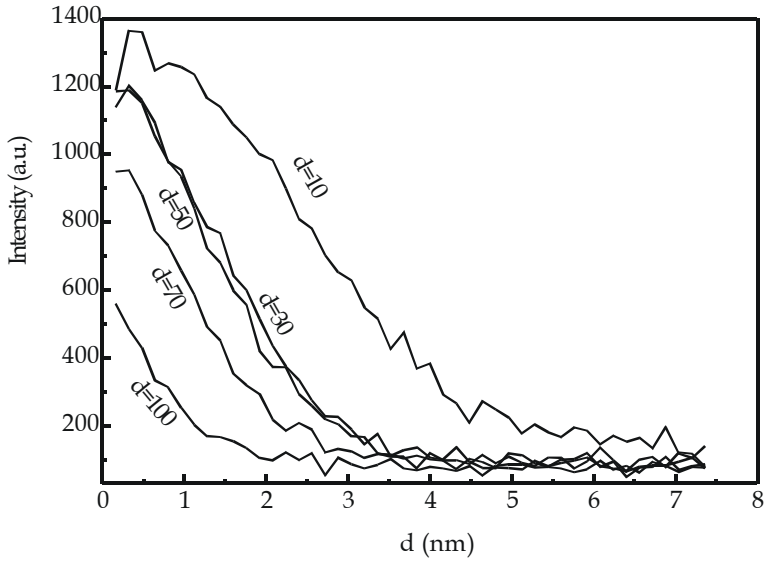

Figure 3.12: *Depth profiles of oxygen for different beam sizes (in μm)*

From figure 3.12, it is clear that smaller spots have thicker oxide layers, but several factors that hinder the quantification of absolute oxide thickness have to be taken into account. From the discussion in chapter 2, it seems that atomic mixing and redeposition of oxides are most important in this case. However, quantification of the amount of O and the absolute oxide thickness is not the main objective of this depth profile, but rather the comparison between the different spots. In the ideal case, the oxide thickness corresponds to the depth where the O intensity reaches the minimum. However, the actual thickness must be smaller than that indicated in figure 3.12, because both effects mentioned overestimate the oxide thickness. Moreover, the distances between the measured sites are about the size of the sputtered area (~500 μm). This makes it doubtful whether the sputtering rate is the same on every site. The spots with different sizes are randomly distributed over the surface; therefore the general trend that emerges from this picture remains clear.

In order to further quantify the effect of the electron flux a series of electron beam enhanced oxidation experiments was performed while increasing the beam current by an order of magnitude (24 nA). Clearly for d=30 and 50 μm spot sizes complete saturation is achieved as is seen in figure 3.13, in comparison with figure 3.10. The time necessary for saturation of the 30 and 50 μm curves using 24 nA is the same as for 5 and 10 μm using 2.4 nA. This, and

the fact that the oxidation of the 5 and 10 μm spots at 24 nA saturated at a similar timescale, confirms the assumption that the oxidation cannot proceed faster than at a certain rate. An estimation of the partial pressure of H_2O molecules of $5 \cdot 10^{-9}$ Pa (~10% of the ambient pressure, which would be rather high) yields the buildup of one monolayer of oxygen in $2 \cdot 10^4$ s. This is of the same order of the time necessary for chemisorption. The oxygen supply from the vacuum chamber is most probably the limiting factor. In the beginning of the oxidation process, the partial pressure of oxygen containing molecules may be higher due to the preceding ion-cleaning of the surface. The data for d = 5 and 10 μm spot sizes are not shown in figure 3.13, because they would obscure the data for 30 and 50 μm For d = 70 and 100 μm the oxidation is weaker and the chemisorption regime can be distinguished.

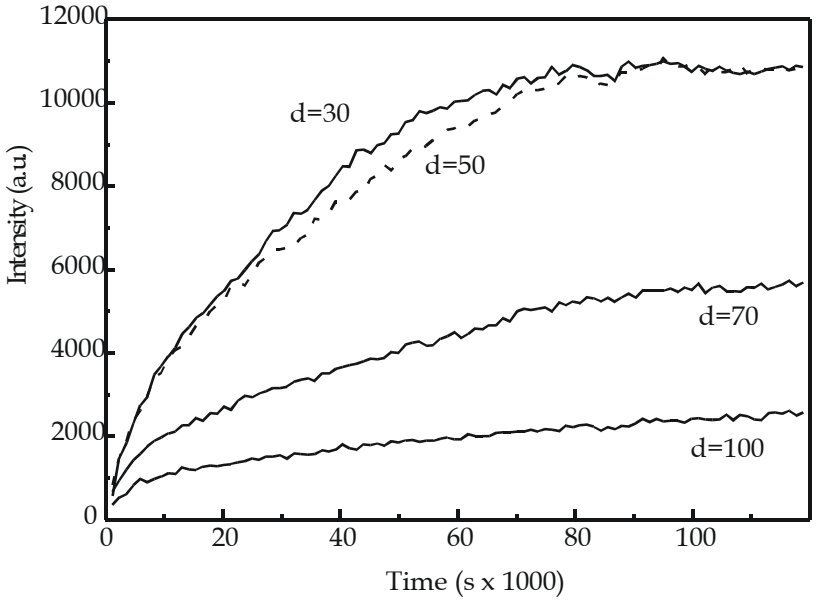

Figure 3.13: *Evolution of oxygen peak-to-peak heights for different beam sizes (different fluxes) using 24 nA beam current*

In figures 3.10 and 3.13 only the acquired data for oxygen, i.e. the oxygen peak-to-peak intensities, are shown. However, intensities depend on topography and (in the case of extremely large areas of measurement, ~ 1 mm^2) place of origin. Therefore, the oxygen intensity has to be compared with the intensity of Ni, which has the same dependence on topography and origin. The absolute O and Ni intensities at the beginning of oxidation and at saturation are similar for all data sites, except for 100 μm, where the absolute Ni intensity is much lower. Therefore, although in figure 3.13 the absolute O intensities differ for 70 and 100 μm, the relative intensities (the O/Ni intensity ratios) for 70 and 100 μm are comparable.

The SE image and Auger map of oxygen are shown in figure 3.14. Minimum spot size was used for the Auger map, with a dwell time of 100 ms.

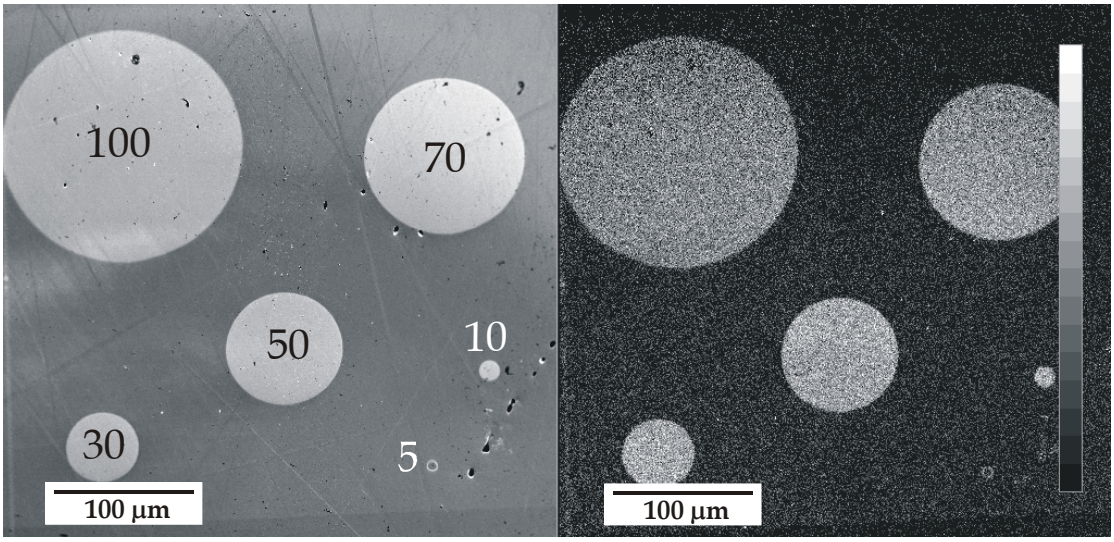

Figure 3.14: *SE image (left) and Auger map of oxygen (right) after electron beam enhanced oxidation with different beam sizes (in µm)*

3.5 DISCUSSION AND CONCLUSIONS

The oxidation kinetics of pure Ni, Ni_3Al, Ni_3Al-B and Ni(B) under the influence of an electron beam can be adequately described by a model assuming the creation of extra oxidation nucleation sites by the electron beam. Because this model describes oxidation of a surface with chemisorbed oxygen (not more than one monolayer) already present, the electron beam probably induces in-depth oxide growth. Therefore, more than one monolayer can form upon beam irradiation. The oxide nucleation sites probably are some type of electron rich site similar to F-center anion vacancies created by sputtering a NiO surface. On pure Ni and Ni(B) the chemisorption regime is separated from the fast oxide growth regime, whereas for Ni_3Al both regimes overlap. The fast oxide growth surpasses the chemisorption regime, which hinders the direct observation of the chemisorption regime, unless lower electron fluxes are used. Different electron fluxes were used to validate the model. At lower fluxes, surface oxidation slowed down and the chemisorption regime could be distinguished. At higher fluxes no faster oxidation was observed. Here, the electron flux and therefore the created number of nucleation sites is so large that the amount of oxygen present in the vacuum chamber becomes the rate limiting factor, determining the oxidation kinetics. In the model, the oxidation rate is then governed by the term $\exp(-kt)$ after the first cycles, which causes the reasonable agreement with

the simple exponential Langmuir model. The strength of the Wei Li model becomes clear upon variation of the electron beam spot size and therefore the incident electron flux. Together with an extra term that describes the chemisorption regime, it can adequately fit all oxidation stages. The addition of the extra term is necessary because, contrary to pure Ni and Ni(B), the chemisorption and fast oxide regimes overlap for Ni_3Al(-B),

It needs to be pointed out that all oxidation curves were obtained with measurement cycles consisting of sequentially exposing several sites to the electron beam while measuring the intensity, after which the next cycle starts. Previous investigations [10,13] have revealed that it is not necessary to expose the sites to an electron beam continuously, because oxidation was already observed after single exposure of a surface to an electron beam and subsequent oxygen exposure. From these observations, it was concluded that created nucleation sites remain metastable for some time after exposure [10], although the number of nucleation sites is decaying with time and depends on the temperature as well. In order to confirm this assumption a comparison was made between the oxidation of undoped Ni_3Al on a single site (continuous exposure) and the oxidation of three sites (alternating exposure / non exposure), as in figure 3.5. Saturation was reached after similar periods of time: ~ $6 \cdot 10^4$ s for three sites and ~ $7 \cdot 10^4$ s for one site. The sequential oxidation even seemed somewhat faster, which may be attributed to different pressures during the measurements. It has to be pointed out that for the sequential oxidation each cycle consisted of ~9 minutes, meaning three minutes exposure and six minutes non-exposure. Longer periods of non-exposure between exposure may lead to differences in oxidation rate, because the number of nucleation sites is assumed to decrease with time when the surface is not exposed. However, it is likely that this effect is only visible at larger spot sizes or smaller incident fluxes, because it is concluded that for the conditions used the amount of oxygen present is the rate limiting factor and not the number of created nucleation sites.

Comparing the fast oxide growth for Ni_3Al(-B) with that of Ni at low temperatures (147 K), where the chemisorption regime is suppressed, we assume that the O sticking coefficient remains close to 1 [8,14]. Only upon saturation, it will decrease below 0.1. An initial sticking coefficient of 1 is assumed. For pure Ni at room temperature, the sticking coefficient already becomes lower than 0.1 during the chemisorption regime and will remain below that value, even during the fast oxide growth [8,14].

The phenomenon of electron beam enhanced oxidation is encountered during boron segregation studies in Ni_3Al and is found to obscure the observation of surface segregation as a function of time. However, a change of the electron flux leads to a decrease of the oxidation rate. Figure 3.15 shows that when a lower incident electron flux is used, some development of B at the surface can be visible. B surface segregation occurs before saturation of the fast oxide growth regime. In figure 3.15, the evolution of Ni, Al, O and B intensities with time is shown. The increase in B intensity is clearly visible, as well as the saturation at ~$9 \cdot 10^4$ s. When larger fluxes are used, the oxidation process is already completed at ~$6 \cdot 10^4$ s (figure 3.5), long before the saturation of B intensity. In figure 3.15, the beam spot size was 100 μm, with a current of 2.4 nA.

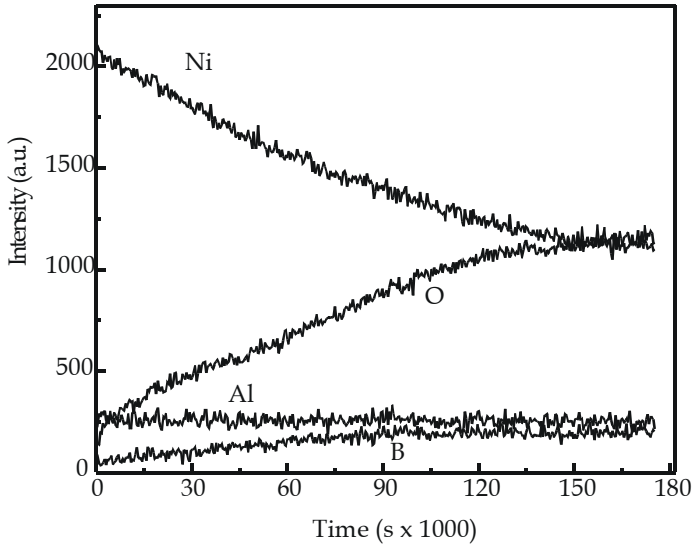

Figure 3.15: *Evolution of the intensities of B, O, Ni and Al, using a low electron flux*

The oxidation process or other electron beam effects may play a significant role during attempts to monitor processes at the surface. Therefore, special care has to be taken in surface segregation studies, because of the irreversible changes that are associated with oxide formation by the electron beam.

REFERENCES

1. J.M. Fontaine, O. Lee-Deacon, J.P. Duraud, S. Ichimura, C. Le Gressus, Surf. Sci. **122** (1982) 40
2. Y. Chen, Y. Luo, J.M. Seo, J.H. Weaver, Phys. Rev. B **43** (1991) 4527
3. C. Becker, J. Kandler, H. Raaf, R. Linke, T. Pelster, M. Dräger, M. Tanemura, K. Wandelt, J. Vac. Sci. Technol A **16** (1998) 1001
4. E.W.A. Young, J.C. Rivière, L.S. Welch, Appl. Surf. Sci. **28** (1987) 7
5. A.M. Venezia, C.M. Loxton, Surf. Interface Anal. **2** (1988) 287
6. A. Rosenhahn, J. Schneider, C. Becker, K. Wandelt, Appl. Surf. Sci. **142** (1999) 169
7. A. Rosenhahn, J. Schneider, J. Kandler, C. Becker, K. Wandelt, Surf. Sci. **433-435** (1999) 705
8. P.H. Holloway, J.B. Hudson, Surf. Sci. **43** (1974) 123
9. Wei Li, M.J. Stirniman, S.J. Sibener, J. Vac. Sci. Technol. A **13** (1995) 1574
10. M.J. Stirnimann, Wei Li, S.J. Sibener, J. Chem. Phys. **103** (1995) 1574
11. B.D. Zion, A.T. Hanbicki, S.J. Sibener, Surf. Sci. **417** (1998) L1154
12. J.A. Slezak, B.D. Zion, S.J. Sibener, Surf. Sci. **442** (1999) L983
13. Wei Li, M.J. Stirnimann, S.J. Sibener, Surf. Sci. **329** (1995) L593
14. P.H. Holloway, J.B. Hudson, Surf. Sci. **43** (1974) 141
15. E.S. Snow, P.M. Campbell, F.K. Perkins, Naval Res. Rev. **XLIX** (1997) 15
16. J. Noguess, I.K. Shuller, J. Mag. Mag. Mater. **192** (1998) 203
17. S.J. Sibener, R.J. Buss, C.Y. Ng, Y.T. Lee, Rev. Sci. Instrum. **51** (1980) 167
18. P.N. Peters, H.C. Gregory, J.T. Swann, Appl. Opt. **25** (1986) 1290
19. S. Hofmann, G. Stepanova, Appl. Surf. Sci. **90** (1995) 227
20. J. Verhoeven, J. Los, Surf. Sci. **82** (1979) 109
21. S. Tanuma, C.J. Powell, D.R. Penn, Surf. Interface Anal. **11** (1988) 577
22. H. Brune, J. Wintterlin, J. Trost, G. Ertl, J. Wiechers, R.J. Behm, J. Chem. Phys. **99** (1993) 2128
23. P.A. Thiry, J. Ghijsen, R. Sporken, J.J. Pireaux, R.L. Johnson, R. Caudano, Phys. Rev. B **39** (1989) 3620

Chapter 4

EMBRITTLING SEGREGANTS IN COPPER

4.1 INTRODUCTION

Grain boundary segregation of impurity elements in copper, such as bismuth or antimony, produces changes in the properties of bulk material. The embrittlement of Cu by Bi is a classic example of grain boundary embrittlement and was first demonstrated by Hampe in 1874 [1]. Only much later, Voce and Hallowes [2] suggested that the embrittlement was due to a film of Bi along the grain boundaries. McLean [3] suggested that segregation was responsible, but the experimental confirmation had to wait for the development of Auger electron spectroscopy. After that, Cu-Bi has been often used as a model system for segregation studies. The reasons are, besides the historical significance, the absence of environmental effects such as hydrogen embrittlement and the relative simplicity of the system [4]. Only two elements are involved, which do not form any intermetallic phase. Cu-Bi was one of the first systems that was extensively studied during the advent of Auger electron spectroscopy [5]. In the course of these studies, large differences in Bi segregation levels between different grain boundaries were found [6,7].

Antimony and bismuth are in the same column of the periodic table, which would imply that the chemistry of these elements is about equal. The main difference between the two elements is then due to the size effects. The metallic radii of the elements are 1.82 Å for Bi, 1.45 Å for Sb and 1.35 Å for Cu [8]. Both Bi and Sb are significantly larger than Cu, which leads to low solubilities in copper and a strong tendency to segregation. The solubility of Bi in Cu is less than 3 ppm at 600° C [9], whereas the solubility of Sb in Cu ranges from 0.5 to 5 at.% between 150° and 700° C, as was estimated from the Cu-Sb phase diagram

[10]. The propensity to brittle failure of a grain boundary for a given segregant apparently cannot be related directly to its size or to the resultant grain boundary structure and crystal orientation. However, these factors do have in common that they determine the equilibrium amount of segregant at the grain boundary [11].

The observation of different segregation levels at different grain boundaries using Auger electron spectroscopy can suffer from some artifacts. Studies of grain boundary segregation with AES require intergranular fracture. If the fracture path follows the grain boundaries, it will most likely follow the most embrittled grain boundaries, which will be those with the highest amounts of segregants. Therefore, the distribution of segregation levels may be biased towards those boundaries with high segregation levels.

Furthermore, the fracture path may have a large influence on the measured segregation levels. Compared to Cu-Bi, the distribution of the extent of segregation that was observed in iron-tin and iron-sulfur was much narrower [12]. In *bcc* materials such as iron intergranular fracture occurs very precisely along the grain boundaries, whereas in *fcc* materials the fracture is usually a mixture of brittle and ductile intergranular fracture [13]. This spreads the fracture path somewhat unpredictably and lower segregation levels will be measured if the fracture path deviates even slightly from the grain boundary plane. The last effect that needs to be mentioned is the fact that the two created surfaces can retain different amounts of segregant, as was observed in carefully controlled experiments on bicrystals [14,15].

Another embrittling segregant in copper is sulfur, which can be present as an impurity in copper. The sulfur content in commercially pure copper is very low, but still above the solubility limit of sulfur in copper. The solid solubility of S in Cu is about 10 ppm at 600° C [10,16]. Application of pure, oxygen-free copper as a construction material with excellent corrosion resistance is limited due to intergranular embrittlement at temperatures above 100-150° C [17]. Intergranular cavitation and fracture, preferentially at random grain boundaries, have been observed with the fracture surface being enriched in sulfur [18]. Sulfur grain boundary segregation is therefore thought to be the cause of embrittlement.

From the phase diagram, it is natural to expect the formation of Cu_2S at the grain boundaries in polycrystalline Cu [10,16]. Stoichiometric Cu_2S can exist in three crystal structures: low chalcocite (αCh, monoclinic), high chalcocite (βCh,

hexagonal) and high digenite (Dg, cubic). The temperatures of the structural transformations correlate with the embrittlement temperatures of copper [17]. At high temperatures, the solid solution of S is in equilibrium with the high digenite phase. This phase has the sulfur atoms arranged in an *fcc* lattice and the Cu atoms occupy all tetrahedral interstitial sites [17]. Experiments [19,20] have shown that additional copper vacancies form easily in the off-stoichiometric digenite $Cu_{2-x}S$. Because of the formation of this very stable Cu_2S phase the solubility of S in Cu is limited.

Due to the large vacancy content the coordination number of Cu atoms in Cu_2S is reduced compared to that in *fcc* Cu, which leads to a faster diffusion of Cu in copper sulfides [21]. The diffusion of S in Cu is very fast as well; of all substitutional impurities considered in [22] S has the largest bulk diffusion coefficient. The abovementioned processes are attributed to strong interactions between vacancies and impurities [17]. For the Cu-S system, strong interaction between vacancies and sulfur atoms leads to the formation of bound complexes that have a low dissociation probability and a high mobility in the crystal [17]. Sulfur-vacancy complexes will segregate to grain boundaries, dislocations and surfaces, thereby increasing the concentration of vacancies in the close vicinity of these defects. Sulfur-vacancy complexes diffuse along the defects and form extended arrangements by meeting each other. Upon incorporating Cu, precipitates of copper-sulfide are formed at defects.

The presence of copper sulfide precipitates at grain boundaries is rather undesirable due to the structural transformations they experience with changing temperatures. In combination with the mechanical properties of copper sulfide, crack nucleation and propagation at grain boundaries under creep conditions are favored.

In this chapter, segregation studies are performed on Cu-Sb systems, containing S as an impurity. The driving force for segregation of antimony is mainly the size effect. Therefore, it is plausible that Sb preferentially segregates to higher index grain boundaries, where it is easier to accommodate the size difference than at the more densely packed lower index planes. The segregation of sulfur occurs through another mechanism, described above. Therefore, the influence of the presence of sulfur impurities on the segregation behavior of antimony, to grain boundaries and surfaces, may be investigated. On the other hand, the presence of another element can have an influence on the precipitation of copper sulfides. In previous studies [17], the presence of silver or phosphorous

in Cu-S systems was shown to considerably reduce the copper sulfide precipitation due to site competition of silver or phosphorous with sulfur. Furthermore, Cu-Bi alloys with Bi contents far above the solubility limit will be fabricated. In these alloys, precipitation will certainly occur.

Cu-Sb and Cu-Bi are prepared by melting the pure constituents together in a graphite crucible, in an evacuated quartz tube. The material is heated to 1100° C for one hour, after which the specimens are slowly cooled. The graphite crucible is constructed in such a way that after melting, the specimens had the right dimensions for in situ fracture in the JEOL JAMP 7800F. After the fabrication of these alloys, sulfur is present as an impurity. The cylindrical specimens are circularly notched and are in situ fractured at liquid nitrogen temperature, to promote intergranular fracture.

Prior to the heat treatments for the segregation studies, the specimens are homogenized at 750° C for 5 hours. Specimens with Sb contents ranging from 0.3 to 2.0 at.% are heated at different temperatures for different times, after which they are water quenched. In all cases of Auger imaging the Cu LMM (916 eV), Sb MNN (452 eV) and S LVV (146 eV) peaks in the direct spectrum are used. The ratio *(P-B)/B* was recorded, with *P* the intensity at the peak position and *B* the intensity at the background at the right end of the peak, to reduce topography effects. The corresponding escape depths are, assuming a copper matrix, λ_{Cu} ~ 1.5 nm, λ_{Sb} ~ 0.9 nm and λ_{S} ~ 0.6 nm [23]. In the Cu-Bi alloys, the bismuth content was 1 or 2 at.%.

4.2 SULFUR AND ANTIMONY ON FRACTURE SURFACES

4.2.1 Site competition in pits

The in situ fractured Cu-Sb specimens show very irregular fracture surface morphologies. The height differences of the fracture surface are large, as can be seen in figure 4.1, where the fracture surface of Cu-1.4 at.% Sb is displayed. The fracture direction, in this image, is almost vertical, in the direction of the arrow in figure 4.1. Before intergranular failure, significant deformation must have occurred, which is expressed through the height differences and the slip lines on the fracture surfaces, visible at higher magnification. It is necessary to cool the specimen with liquid nitrogen to induce intergranular failure.

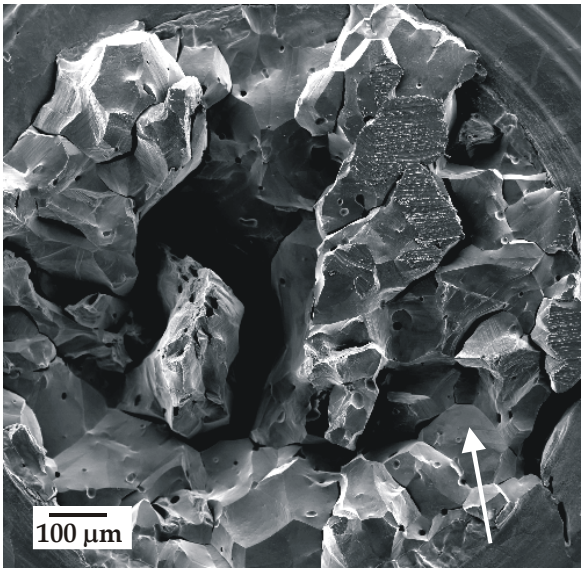

Figure 4.1: *Fracture surface of Cu-Sb. The lateral size of the image is ~ 1 mm*

Upon fracture, the exposed surface, i.e. the previous grain boundaries, reveal the existence of localized pits with a well-defined structure that is composed of facets and step-terrace structures, as can be seen in figure 4.2. Also visible are the slip lines on the exposed surface.

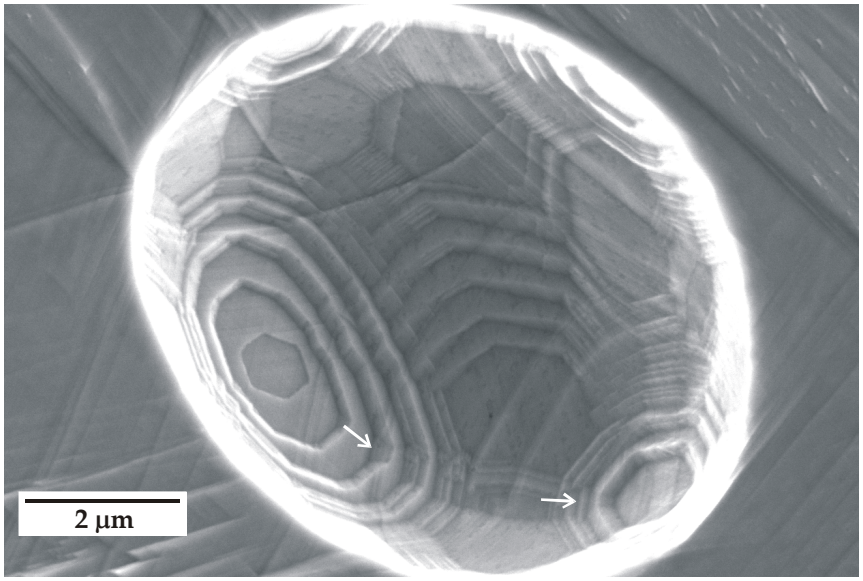

Figure 4.2: *Structure of a pit that appeared after fracture. The arrows indicate that the seemingly hexagonal facets actually have twelve sides.*

Every pit contains distinct facets. The arrows in figure 4.2 indicate that the seemingly hexagonal facets actually have twelve sides. This becomes clearer with increasing distance from the central 'hexagonal' facet. When several pits are present on the same former grain boundary, the arrangement of the facets

with respect to each other is similar, which is shown in figure 4.3(right). Hexagonal and square facets can be distinguished in the center and top left corner of the pits, respectively. This leads to the conclusion that the pits are formed during fabrication and that the formation of the facets is governed by minimization of surface energy of the sulfur covered copper matrix.

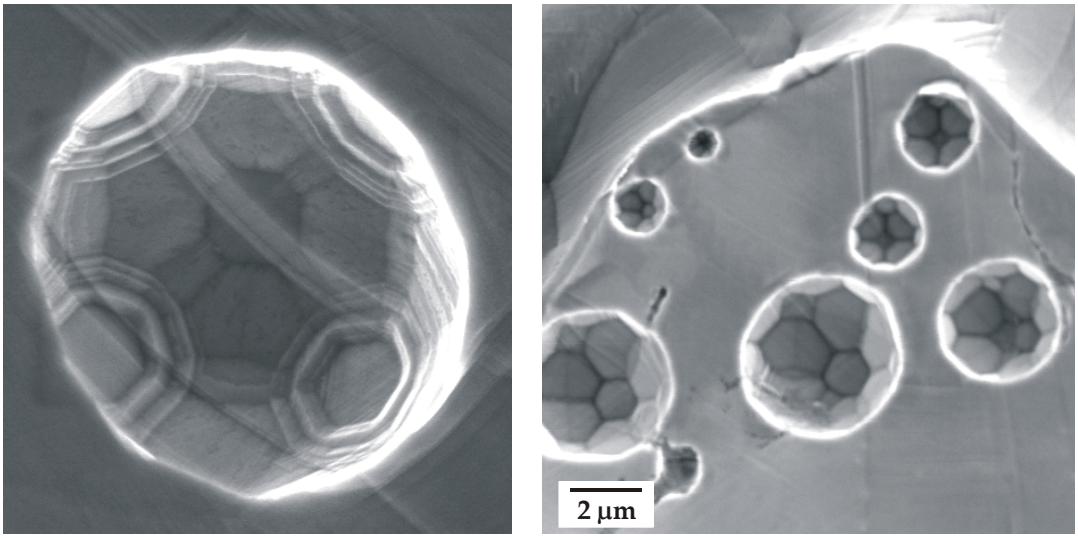

Figure 4.3: *Arrangement of facets inside the pits*

In a few cases, precipitates were observed on the fracture surface. One of these precipitates is shown in figure 4.4, while figure 4.5 shows Auger spectra obtained on the surface of the precipitate and next to it, on the Cu surface.

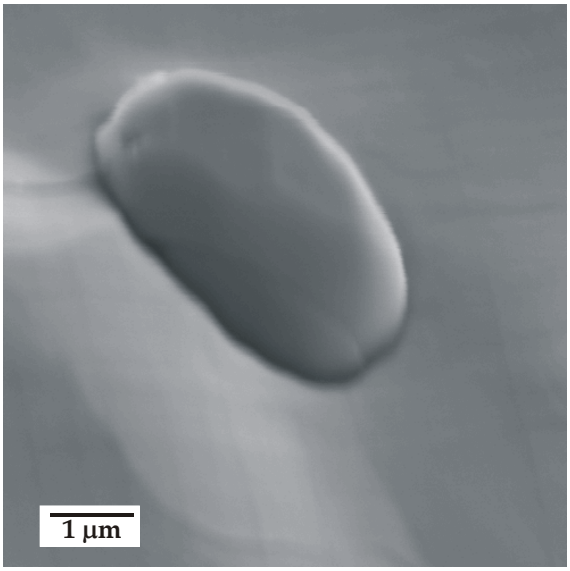

Figure 4.4: *Cu_2S precipitate on a former grain boundary*

The intensity of the spectrum on the Cu surface is shifted upwards in figure 4.5, to prevent overlap of the two spectra.

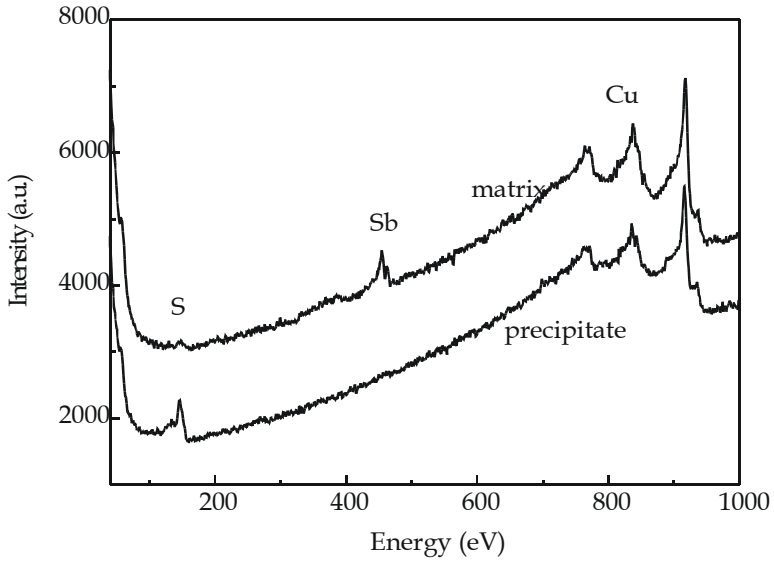

Figure 4.5: *Auger spectra on the precipitate and the surrounding matrix*

The differential spectra of figure 4.5 are used to obtain the concentrations of Cu and Sb next to the precipitate, using equation (2.19) for the Cu surface with segregated Sb, assuming monolayer segregation of Sb. The used parameters and quantification results are shown in table 4.1. The amount of segregated Sb is ~ 1 monolayer.

Table 4.1: *Quantification parameters and results*

I_{Sb}	I_{Cu}	r_{Sb}	r_{Cu}	K	Γ_{Sb}
129	458	1.0	0.8	3.3	0.9

Energy dispersive X-ray spectroscopy analysis in the Philips XL 30 SEM on a similar precipitate yields a composition of (32 ± 1) at.% S and (68 ± 1) at.% Cu. This supports the assumption that Cu_2S precipitates are formed during the processing of the Cu-Sb alloys. The melting temperature of Cu_2S is ~1131° C [10,16], which is an indication of the stability of this phase, because pure Cu melts at 1085° C. During the fabrication of the alloy, fast diffusion of sulfur-vacancy complexes is possible, leading to the formation of Cu_2S.

Only in a few cases, precipitates like in figure 4.4 are observed. More often, pits are observed with a small sulfur-rich part on the outside of the pit. As an example, figure 4.6 shows a large pit with a clear structure of facets and steps,

accompanied with an Auger image of sulfur. This shows that the small part on the right side of the pit is sulfur-rich, presumably Cu_2S.

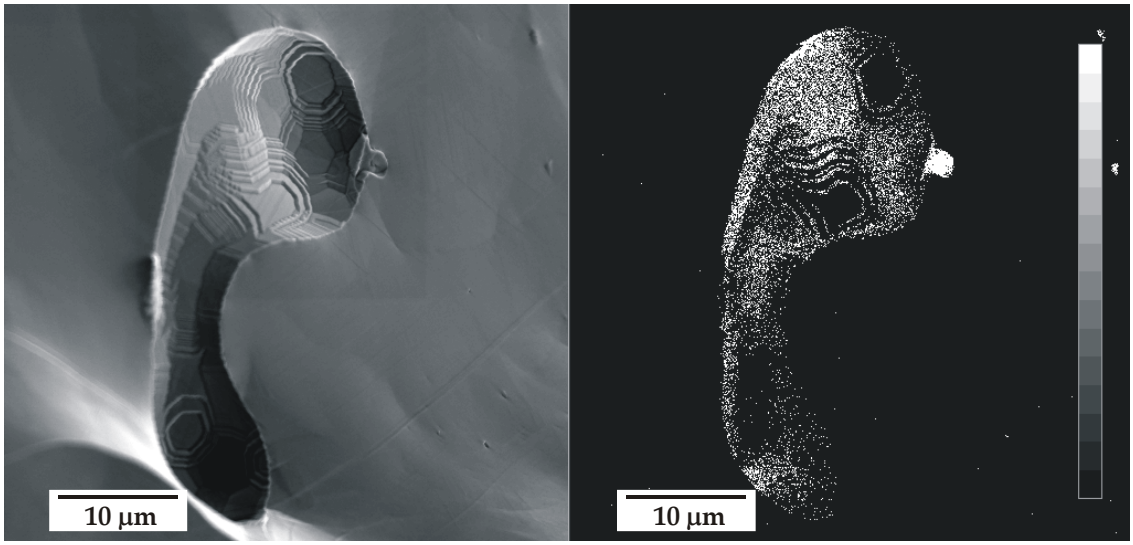

Figure 4.6: *SEM image of a large pit (left) and scanning Auger image of sulfur (right)*

On the Cu surface, no sulfur is observed. However, within the pit sulfur is detected locally, except on the hexagonally shaped facets and the terraces surrounding these facets. In order to examine the sulfur distribution, scanning Auger images of sulfur were acquired for several pits. In figure 4.7 it can be seen that the sulfur intensity in the Auger map varies from facet to facet and is almost zero on the hexagonal facets. Furthermore, it can be observed that in the small pits of figure 4.7 and those in figure 4.3 (right), only facets are present and no step-terrace structures are surrounding the facets. The size of the facets linearly increases with the pit size [24]. Only inside pits larger than ~ 5 μm, step-terrace structures are observed and the sizes of the facets no longer increase with the pit size. From this it can be concluded that in small pits the minimization of surface energy can be accomplished by the creation of facets only. In larger and irregularly shaped pits, a transition between the low energy surfaces in the form of steps and terraces is needed. Presumably, the steps and terraces between two low energy surfaces are parallel to those surfaces. In figure 4.6, sulfur is absent on the almost hexagonal facet in the center of the image. On the steps and terraces that form the transition to the facet above that, sulfur is alternatively absent or present. In the SEM image (figure 4.6, left), the terraces where sulfur is absent seem parallel to the middle facet and the steps may have the same orientation as the upper facet. Figure 4.8 shows a higher magnification image of a part of another, larger pit, accompanied by a scanning Auger image of sulfur. Again, sulfur is not present on the hexagonal facets and

the terraces surrounding it. On the steps, sulfur is present, but even between differently oriented steps differences can be observed. The central facet seems hexagonal, but actually has 12 sides, six large and six small ones. The steps parallel to the large sides yield a larger sulfur intensity than the steps parallel to the small ones, which is the almost black part of the Auger image on the left of the central facet.

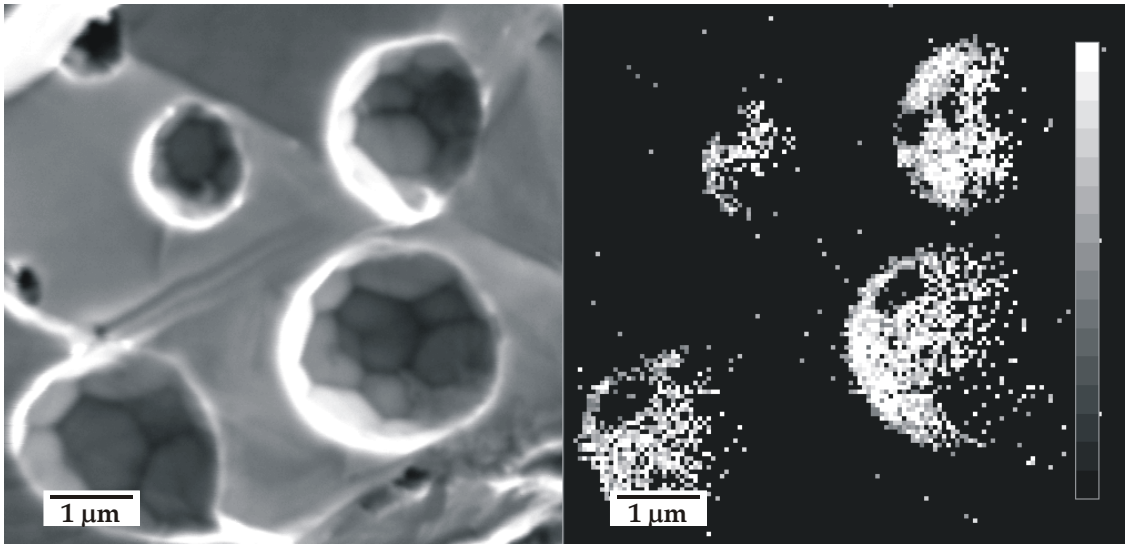

Figure 4.7: *SEM image of small pits containing only facets (left) and scanning Auger image of sulfur (right)*

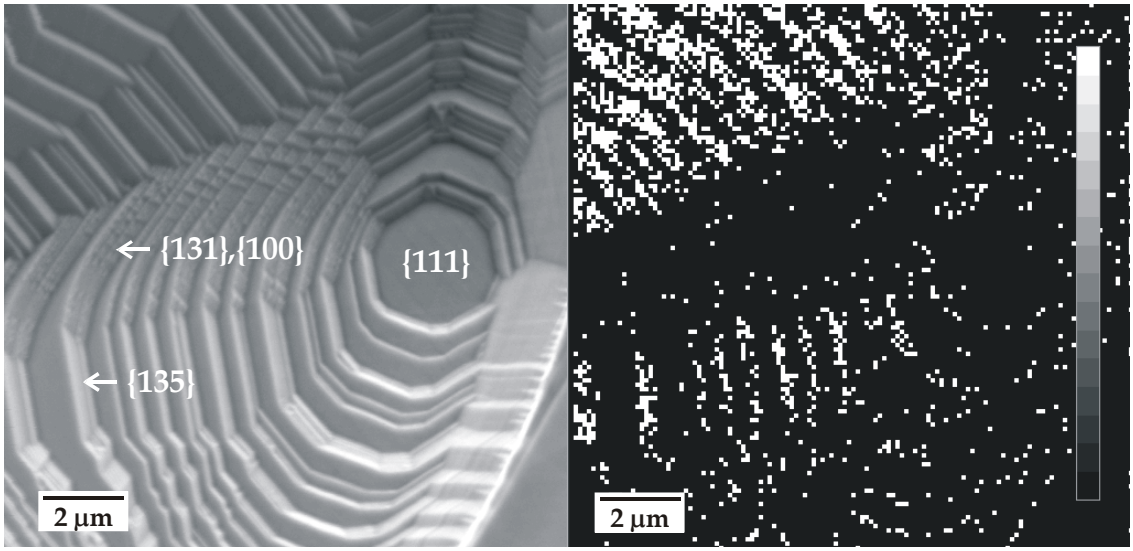

Figure 4.8: *SEM image of a step-terrace structure in a large pit (left) and scanning Auger image of sulfur (right). The indices are estimated, based on the geometry of the facets*

To clarify this, figure 4.9 shows a scanning electron of a hexagonal facet, surrounded by step-terrace structures and other facets. The small sides of the

'hexagon' become larger in the structure surrounding the central facet. A few more step-terraces are observed between the central hexagonal and the facet extending to the right. The scanning Auger image of sulfur in figure 4.9 shows that this facet, which is parallel to the small side of the hexagonal structure, has lower sulfur intensity.

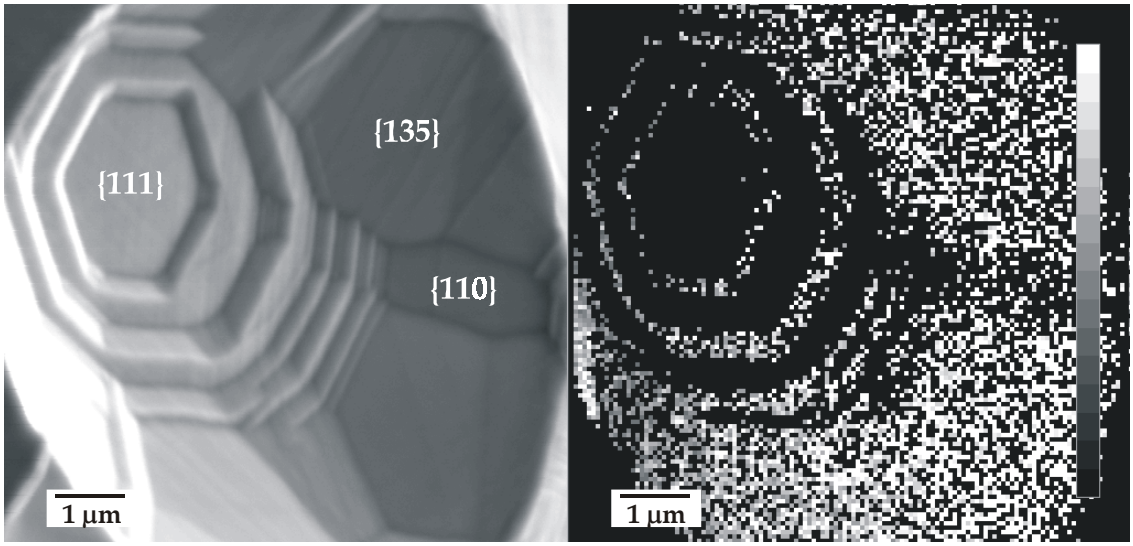

Figure 4.9: *SEM image of a hexagonal facet surrounded by step-terraces and facets, with estimated indices (left) and scanning Auger image of sulfur (right)*

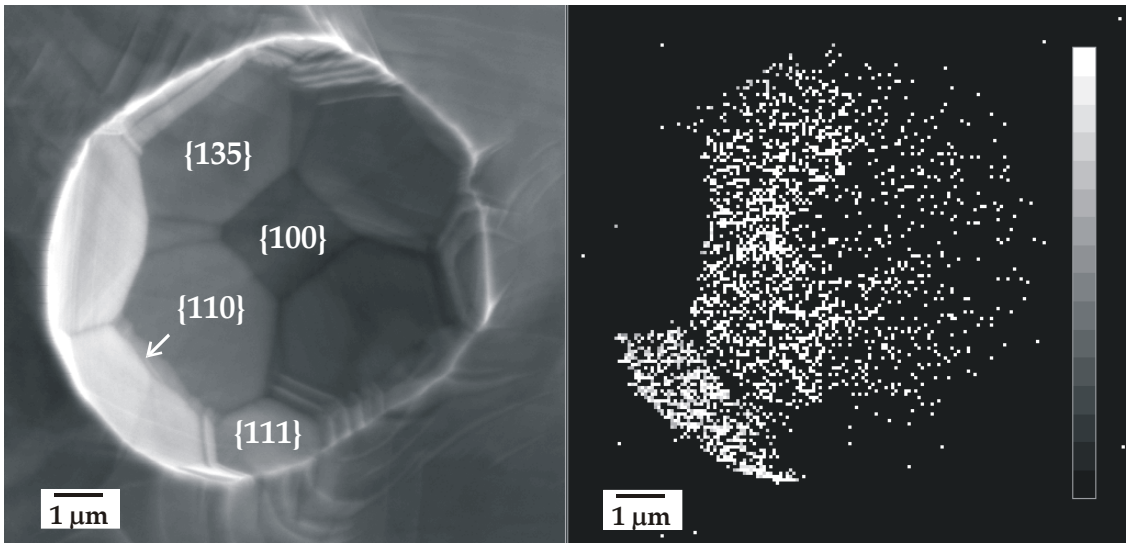

Figure 4.10: *Square facet in a pit, surrounded by four hexagonal facets on the edges, with estimated indices (left) and scanning Auger image of sulfur (right)*

Figure 4.10 shows a square facet in the middle of a pit and four hexagonal facets on the outside of the pit. The scanning Auger image shows that the four hexagonal facets yield a lower intensity of sulfur than the surrounding facets.

However, the sulfur intensity is lower on the square facet as well. Furthermore, the narrow facet between the left and bottom hexagonal facets, which is comparable to the facet on the right in figure 4.9, yields low sulfur intensity. Finally, figure 4.11, which is a high magnification image of the top left side of figure 4.8, shows that the differences in sulfur intensities between the steps and terraces can be resolved up to very small length scales, in the order of ~ 100 nanometer.

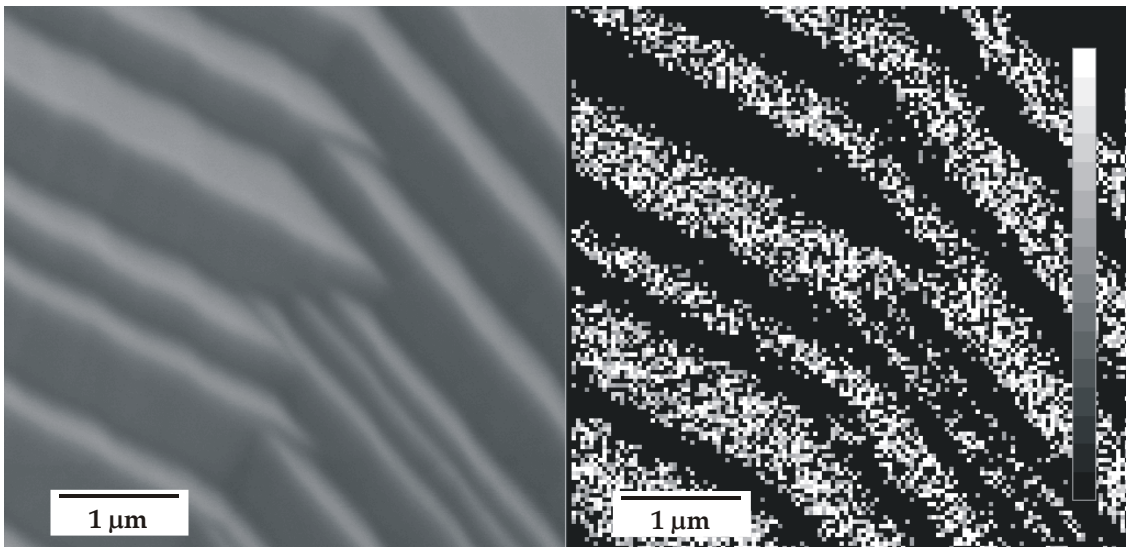

Figure 4.11: *High resolution SEM image of steps and terraces (left) and scanning Auger image of sulfur (right)*

It is assumed that the presence of facets is due to minimization of free energy of the internal surfaces, which leads to the assumption that the observed facets are low index surfaces. Combining this with symmetrical arguments emanating from the face centered cubic structure of the copper matrix, we assume that the hexagonally shaped surfaces and the terraces parallel to them are {111} planes. From this, it is concluded that the square facet in figure 4.10 is a {100} surface.

4.2.2 Determination of the orientations by Atomic Force Microscopy

The fact that sulfur is present preferentially at the steps of the step-terrace structures and that the intensity varies with the precise crystallographic orientation of the steps (figure 4.8) indicates that the presence of sulfur might be strongly correlated with some preferential orientations. The Auger images in figures 4.7 to 4.11 suggest, together with the shapes of the facets where almost no sulfur is observed, that sulfur is absent on low index planes like {111} and {100}. Atomic force microscopy (AFM) imaging allows further determination of

the orientation of the facets surrounding the hexagonal ones. The inclinations of the facets with respect to the hexagonal planes can be measured to index the planes. The inclinations can be computed by taking the derivative of the slope of the facets [25]. More precisely, Hegeman et al. [25] developed a tool for the analysis of facets detected by scanning probe microscopy, adapting a method of radial-histogram transform as proposed by Schleef et al. [26]. The scanning probe microscopy image, e.g. a height image obtained with AFM, is converted first into a derivative of height image and then into a histogram, which exhibits the distribution of the relative amount of image area as a function of its surface normal. The surface normal is described in spherical coordinates θ (inclination angle) and ϕ (azimuth angle). In the original work [26], the first derivative of height z with respect to x and y around each pixel with (x,y) position (i,j) is obtained by taking the derivative over a length scale of three pixels,

$$(z_{i+1,j} - z_{i-1,j})/2 \quad \text{and} \quad (z_{i,j+1} - z_{i,j-1})/2 \tag{4.1}$$

In the presence of noise and particularly in combination with grazing inclination angles of facets, the ability of this three-pixel filter to detect facets is rather questionable. Furthermore, since facets are generally characterized by length scales much larger than three pixels, the filter used for determining the first derivative can clearly be taken larger than three pixels. An efficient convolution filter for differentiation of data over variable length scales is a filter proposed by Savitsky and Golay [27]. Therefore, direct plane fitting to facets making use of the Savitsky-Golay type filter is an alternative approach.

AFM height images of the inside of the pit shown in figure 4.12 are obtained using the Nanoscope II. The images are obtained in air. Due to tip size effects, only a small part of the inside can be imaged, which is depicted in figure 4.12 by the rectangle. Figure 4.13 shows a contour plot of the histogram obtained from the AFM height image, for which a seven-point filter is used. The poles in figure 4.13 depict relatively large areas of the image with the same orientation. The pole situated at $\phi \sim -100°$ and $\theta \sim 11°$ at the bottom right of figure 4.13 corresponds to the central hexagonal facet in figure 4.12 and the terraces that have the same orientation. The inclination is only ~ 11° with respect to the surface surrounding the pit where $\theta = 0$, which is confirmed by the SEM image, figure 4.12. The central hexagonal facet seems almost parallel to the surface surrounding the pit. Besides the central hexagonal facet, five other facets and steps parallel to them are in the region of analysis. These five facets correspond

to the three other poles and two shoulders in figure 4.13. It is calculated from the histogram that the angles between these facets and the central facet range between 26° and 35°.

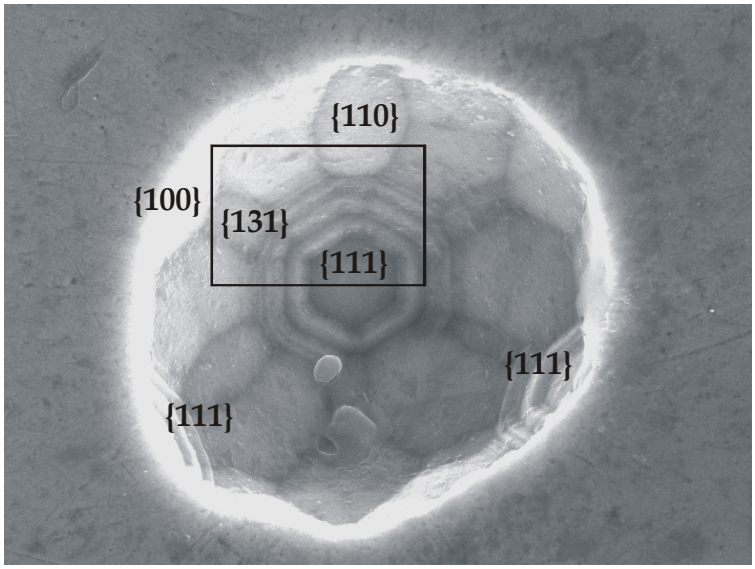

Figure 4.12: *SEM image of the pit used for AFM analysis. The rectangle indicates the analyzed region inside the pit*

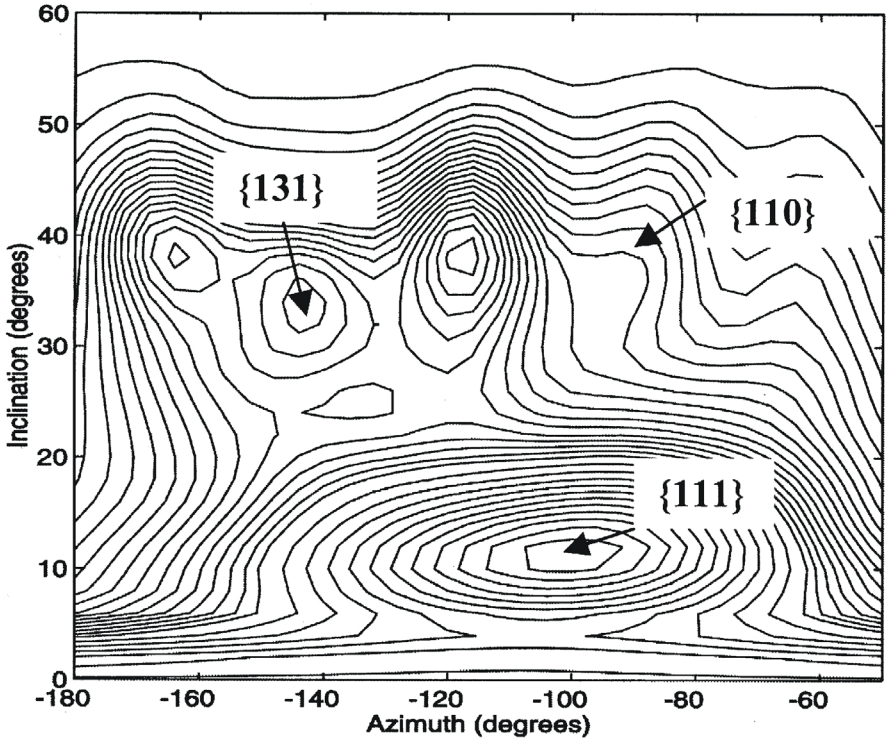

Figure 4.13: *Contour plot of the histogram obtained from the AFM height image, with the inclination angle θ versus the azimuth angle ϕ*

Now, combining shape and symmetry arguments with the AFM results, we can determine the orientations of all twelve facets surrounding the central facet in figure 4.12. It is again pointed out that there are six facets parallel to the large sides of the 'hexagon' and six other facets parallel to the small sides. The three facets between the central {111} facet and the three other hexagonal {111} facets visible have to be {110} surfaces. The three facets between the central facet and the three square {100} facets in this pit might be {131}, as depicted in figure 4.12. These are the six facets parallel to the six small sides. Based on symmetry arguments, the six remaining unknown facets have to be of the same family of planes and must have an angle between 26 and 35° with the {111} plane. Therefore, it is assumed that these facets and the accompanying steps are {135} planes, which make an angle of ~29° with {111} planes. The poles and shoulders in figure 4.13 then correspond to, from left to right {135}, {131}, {135}, {110} and {135} facets and steps. In figure 4.8, the steps parallel to the large sides have to be {135} surfaces and can accommodate more sulfur than the steps parallel to the small sides, which are {131} or {100} planes. In figure 4.9, the facet on the right with a lower sulfur intensity is likely to be a {110} facet in between two {111} facets, which is the same for the narrow facet in the bottom left corner of figure 4.10. The surfaces with the highest amount of sulfur are the highest index planes, where it is easier to accommodate impurities.

In the pits, antimony is present as well. On the surfaces where almost no sulfur is found, antimony is present. The intensities of antimony inside pits are higher on surfaces where almost no sulfur is found and lower when sulfur is observed. This implies that the variations in sulfur intensity are not caused by topographical effects like shadowing or variations of inclination angle with respect to the Auger detector, because all element intensities would experience these effects in a similar manner. Figure 4.14 shows an image of a structure on a Cu-Sb fracture surface, together with scanning Auger images of sulfur and antimony. In this figure the competition between sulfur and antimony is clearly visible. The antimony intensity is never zero, which is different from the sulfur intensity. Besides smaller variations in the antimony content from surface to surface, this can also be caused by the larger inelastic mean free path of antimony, compared to sulfur, causing the antimony signal to originate from deeper inside the material.

So far, the question whether all pits were filled with precipitates before fracture remains unanswered. The number of intact precipitates on the fracture surface, as in figure 4.4, is very small. In most cases, small sulfur rich parts are found on

the outside of irregularly shaped pits, as in figure 4.5. Two reasons are adduced to assume that most pits were empty. Firstly, the number of pits is very large and the sulfur content is probably too low to fill all pits with Cu_2S precipitates. The observation of the number of Bi precipitates in a Cu – 1 at.% Bi alloy yields a fair comparison, as will be shown below. Secondly, the intact precipitates that are observed are quite small (~ 2 to 3 μm), whereas pits extending over several tens of microns are observed (e.g. figure 4.6).

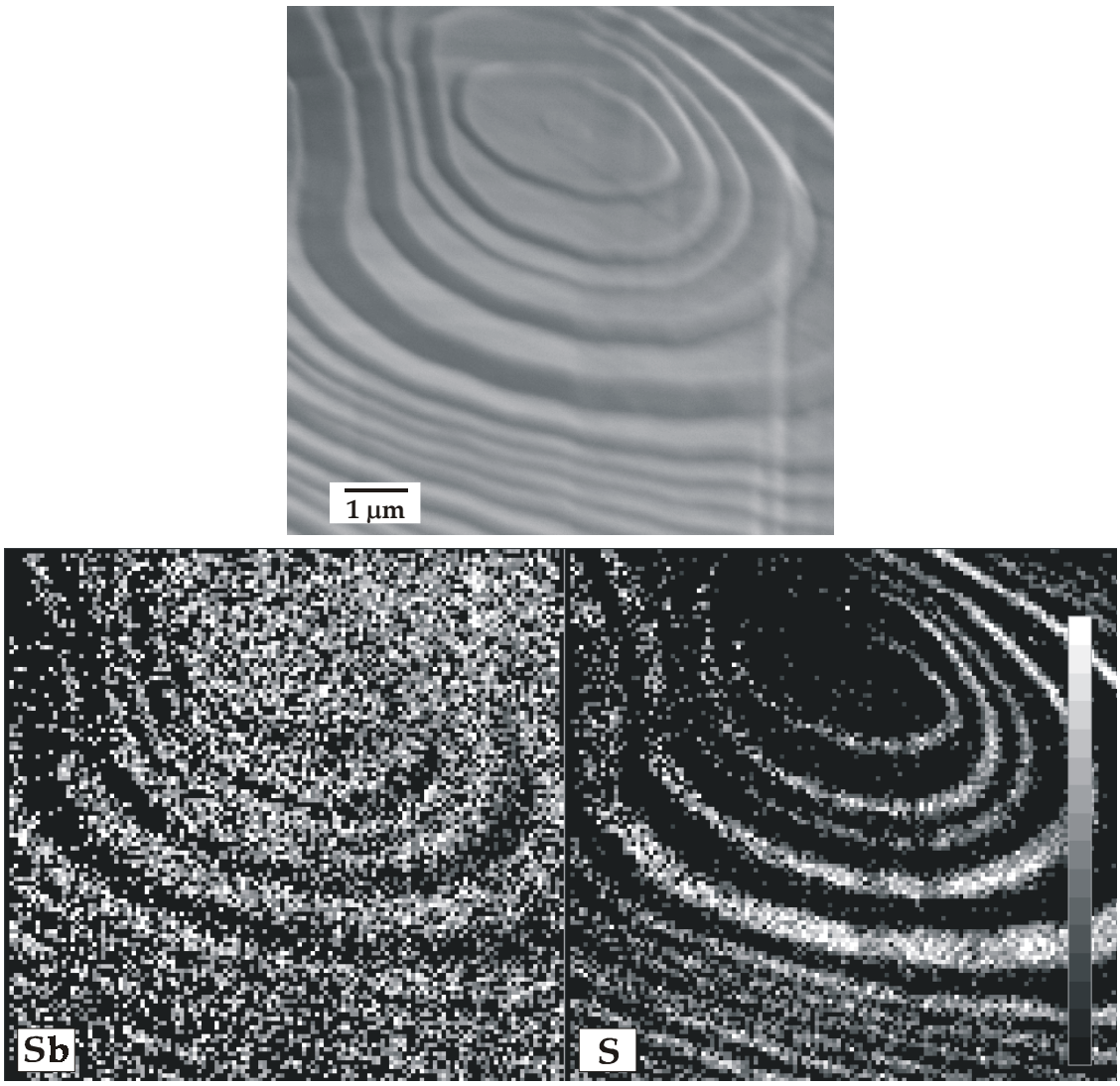

Figure 4.14: *SEM image of a structure on the fracture surface (top) and scanning Auger images of Sb (left) and S (right)*

4.3 PRECIPITATION IN CU-BI ALLOYS

The results from the previous section are compared with the fracturing and precipitation behavior of Cu-Bi alloys, containing either 1 or 2 at.% Bi. Because the fabrication procedure is similar to that of the Cu-Sb alloys, the presence of sulfur as an impurity is expected as well. Figure 4.15 shows SEM images of Bi precipitates that are observed after fracture of a Cu-2 at.% Bi alloy. The fracture surfaces of Cu-Bi alloys are similar to those of Cu-Sb, with large height differences. The surroundings of the precipitates in figure 4.15 indicate that large deformation has preceded fracture.

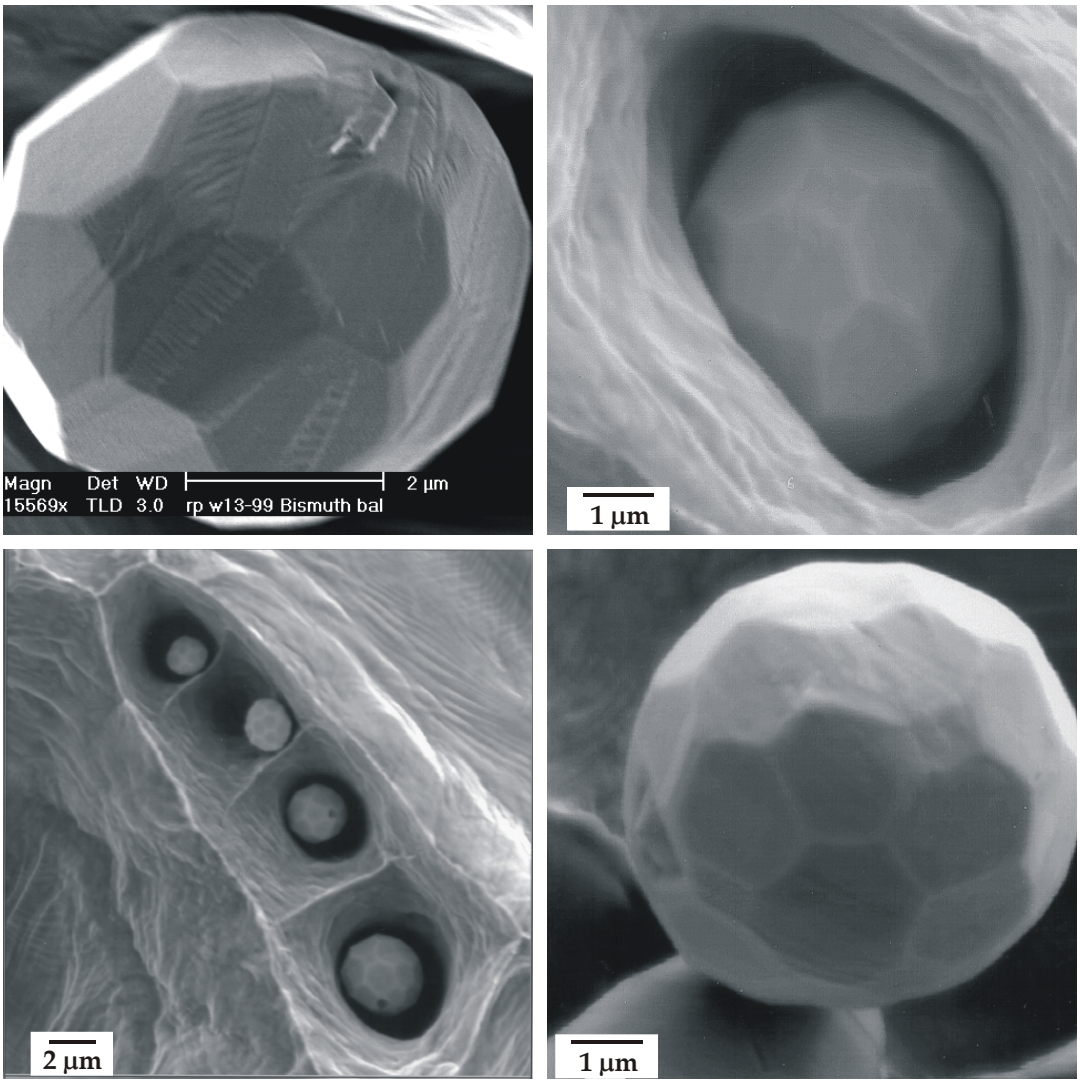

Figure 4.15: *Precipitation of Bi in Cu-2 at.% Bi alloys*

Because of the extremely low solubility of Bi in Cu, almost all present Bi will form precipitates. Auger electron spectroscopy on the precipitates shows,

despite difficulties in obtaining spectra due to the positions of the often partly embedded precipitates, that they consist of pure Bi. The sizes of the Bi precipitates are similar to the sizes of the observed small pits in the Cu-Sb alloys, i.e. several μm. However, at the Cu-Bi fracture surface almost no empty pits are observed. The number of precipitates on the fracture surface was of the same order as the number of pits in Cu-Sb, while there is much more Bi available (~ 2 at.% Bi, compared to impurity levels of S) to form the precipitates, which confirms the assumption that most pits in Cu-Sb must have been empty.

The enormous size difference between Cu and Bi atoms is the cause of the extremely high grain boundary enrichment ratio, i.e. the ratio between grain boundary and bulk composition. In the dilute limit, the ratio is inversely proportional to the solid solubility [28]. Since the grain boundary enrichment ratio for Bi in Cu is larger than 10^4 and the amount of Bi ~ 1 at.%, the ratio cannot be determined from the present observations. The amount of Bi is much larger than the solubility limit, which will lead to strong accumulation of Bi at grain boundaries where Bi will form its own lattice. Since the melting temperature of Cu is much higher than that of Bi ($T_{m,\,Cu}$ = 1085° C and $T_{m,\,Bi}$ = 271° C), Bi will still be in the liquid phase when Cu is solidifying during the fabrication process and it will wet the grain boundaries. When Bi is present in a liquid form, it has been observed to proceed rapidly along the grain boundaries [29]. In the same experiment, it was found that after cooling, Bi appeared not only in the form of particles, but as a layer of bismuth at grain boundaries as well, leading to grain boundary embrittlement [29]. Our experiments did not show a layer of Bi on the fracture surface. However, it is possible that the intergranular fracture path deviates slightly from the grain boundaries, obscuring the observation of segregated Bi.

In the fabrication process, during slow cooling of the alloy, Bi can accumulate and separate from the surrounding Cu matrix due to the shrinkage of Bi during solidification and weak adhesion between Cu and Bi. This leads to the formation of voids, which may strongly alter stress fields locally and form weak spots that promote fracture [30]. This is confirmed by the large amount of precipitates in voids that is observed at the fracture surface. Around the precipitates, significant deformation has occurred, as can be seen in the bottom left corner of figure 4.15, even if the in situ fracture took place at liquid nitrogen temperature. In comparison with Cu-Sb, it can be inferred from observations of the fracture surface that the main embrittling effect of Bi is the formation of precipitates in voids, creating weak spots during fracture. Any effect of sulfur

was obscured by the precipitation of Bi, because the inside of a void could not be examined. In Cu-Sb, the fracture path is seen to follow the grain boundaries more closely, because of the presence of segregated Sb at the boundaries.

4.4 GRAIN BOUNDARY SEGREGATION OF ANTIMONY

In this section the effects of heating temperature and time on the segregation of antimony to grain boundaries, where there is no competition with sulfur, will be explored. After specimen fabrication and homogenization, the material was subjected to different heat treatments before quenching. The heat treatments consist of heating Cu-1.4 at.% Sb for 1 hour at 250, 400 and 700° C and heating at 250° C for different times: 1, 2.5, 4 and 10 hours, respectively. Furthermore, Cu containing between 0.3 and 1 at.% Sb is heated at 400° C for 1 hour. Afterwards, the specimens are in situ fractured in the JEOL JAMP 7800F, after which depth profiles of Cu and Sb are obtained.

The driving force for the segregation of Sb is the size effect. Upon segregation of Sb to a grain boundary, the elastic strain energy that is released, assuming total relaxation at the boundary, is [31]

$$w = \frac{24\pi K_{Sb}\,\mu_{Cu}\,r_{Cu}\left(r_{Sb}-r_{Cu}\right)^2}{3K_{Sb}+4\mu_{Cu}} \tag{4.2}$$

with r_{Cu} = 0.135 nm and r_{Sb} = 0.145 nm, K_{Sb} (=42 GPa) the bulk modulus of Sb and μ_{Cu} (=48 GPa) the shear modulus of Cu [31]. This yields $w \approx 8.0\ 10^{-21}$ J and thus a contribution to the total segregation energy of '$-w$'.

In order to estimate the time and temperature necessary to obtain equilibrium, McLean's approach is used to describe the kinetics of Sb segregation in Cu [32],

$$\frac{X_{GB}(t)-X_{GB}(0)}{X_{GB}(\infty)-X_{GB}(0)} = 1-\exp\left(\frac{FDt}{\beta^2 f^2}\right)erfc\left(\frac{FDt}{\beta^2 f^2}\right)^{1/2} \tag{4.3}$$

Calculations were performed using the Sb GB-enrichment ratio $\beta \sim 4.3/X_B^0$ [33] with X_B^0 the solubility of Sb in Cu, D (= $D_0 \exp(-Q/RT)$ with D_0=3.4 10^{-5} m^2 s^{-1} and Q = 176 kJ/mol [34,35]) the diffusivity of Sb in Cu and f (~ r_{Cu}^3 / r_{Sb}^2) the thickness of the grain boundary. $X_{GB}(\infty)$ is the boundary atom fraction of

segregant at equilibrium and $X_{GB}(t)$ is the boundary content at the annealing time t. $X_{GB}(0)$ is the grain boundary content after the homogenization process. In the temperature range 150-700° C the solubility of Sb is in the range 0.5 at.% ≤ X_B^0 ≤ 5 at.% as was estimated from the phase diagram of Cu-Sb [10,16]. It is concluded that for 1 hour annealing at ≥ 400° C the system is in an equilibrium state. However, other mechanisms such as pipe diffusion along edge dislocations might accelerate solute equilibration (especially for low solute concentrations, as recent studies in Cu-Bi alloys have shown [36]).

Figure 4.16 shows an image of the fracture surface of Cu-1.4 at.% Sb, heated to 400° C for 1 hour and the corresponding scanning Auger images of Sb and Cu. The Auger images display the ratio of intensities *(P–B)/B* to reduce topographical effects on the intensity. Of the four planes visible in figure 4.16, the two on the right yield a higher Sb intensity, whereas the two planes on the left yield a higher Cu intensity. Of all factors that can influence the measured amounts of segregants at grain boundaries, i.e. overestimation of segregation levels since only the weakest boundaries are probed, deviation of the fracture path from the grain boundary and effects of the crystallographic structure of the grain boundary, the latter seems to have the largest influence. However, obtaining many Auger images for planes with a geometry similar to figure 4.16 shows that the planes with similar inclination as the planes on the right in figure 4.16 always yield higher Sb intensities.

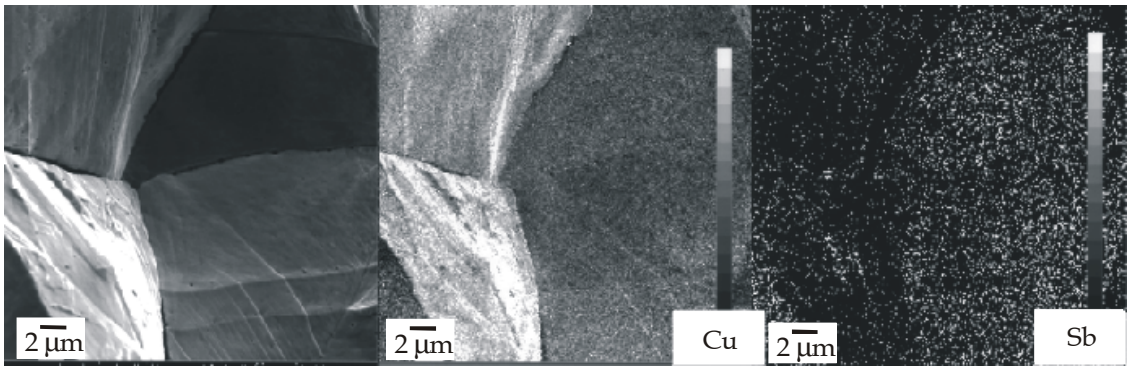

Figure 4.16: *SEM image of four planes on a Cu-Sb fracture surface (left) and scanning Auger images of Cu and Sb (middle and right)*

The geometry of the planes and its influence on the detected Auger intensities in the case of non-homogeneous materials have to be considered. As described in chapter 2, the intensity for both elements present varies as

$$I_A \propto \int_0^{\infty} X_A(z) \exp\left[\frac{-z}{\lambda_M \cos\phi}\right] dz \tag{4.4}$$

where $X_A(z)$ is the concentration of element A as a function of depth z and ϕ is the angle between detector and surface normal. If the material is homogeneous, the Auger intensities that stem from planes with different inclinations will vary with $\cos(\phi)$ only. In that case, it is sufficient to calculate and plot the Auger intensity ratio $(P-B)/B$, since both peak and background intensities have the same variation. This would enable a direct comparison between surfaces with different inclinations. However, when segregation has occurred the material is strongly inhomogeneous in the surface region, from where the Auger electrons originate. The assumption, to be confirmed later by depth profiling, is made that Sb enrichment is present in a few atomic layers at the surface. The Sb concentration profile is assumed to follow an exponential behavior

$$X_{Sb}(z) = X_{Sb}(0)\, e^{-z/\Lambda} \tag{4.5}$$

where Λ is the depth over which the concentration of Sb decreases by a factor $1/e$ and $X_{Sb}(0)$ is the concentration of Sb at the surface. From here onwards we shall refer to Λ as the effective segregation depth. Substituting this in equation (4.4) and calculating that integral for different values of ϕ, one may conclude that the ratio of Sb intensities for different surface orientations is not

$$\frac{I_{Sb,1}}{I_{Sb,2}} = \frac{X^1_{Sb}(0)\cos(\phi_1)}{X^2_{Sb}(0)\cos(\phi_2)} \tag{4.6}$$

as would be the case for a homogeneous Sb distribution, $\Lambda >> \lambda$, but

$$\frac{I_{Sb,1}}{I_{Sb,2}} = \frac{X^1_{Sb}(0)}{X^2_{Sb}(0)} \frac{1+\left[\Lambda/\lambda\cos(\phi_2)\right]}{1+\left[\Lambda/\lambda\cos(\phi_1)\right]} \tag{4.7}$$

This shows that correcting intensities by taking a ratio of peak and background intensities, which is correct when the sample is homogeneous, leads to errors when the sample is inhomogeneous in the surface region. In figure 4.16, the Auger detector is located on the right side of the image. The left planes in figure

4.16 are almost perpendicular to the detector, whereas the planes on the right are almost parallel to it. This leads to an overestimation of the amount of Sb on the boundaries on the right side. Physically, this can be explained by the smaller $\cos(\phi)$ of these boundaries. This causes the amount of Auger electrons originating close to the surface, where the Sb concentration is higher, to be relatively high, leading to an overestimation of the actual Sb concentration. An example, similar to the situation in figure 4.16 shows that the results from equations (4.5) and (4.6) can differ a factor two. Surface normal angles ϕ = 20° and 70° for left and right planes are assumed together with an effective segregation depth of 0.3 nm and an escape depth of Sb Auger electrons in Cu, λ, of ~ 0.9 nm.

Because the exact angles of the different planes with respect to the detector are unknown, it is difficult to determine the variation in Sb concentration with crystallographic orientation of the grain boundaries. It is however most likely that differences in the absolute amounts of Sb do occur. In the remainder of this section, depth profiles are obtained on similarly inclined surfaces, almost perpendicular to the Auger detector. This enables, to some extent, a comparison of segregation levels and depths in different specimens.

Figure 4.17 shows depth profiles of Cu-1.4 at.% Sb specimens heated to 400 and 700° C for 1 hour. The ratio of Sb and Cu intensities is displayed as a function of etching time. The etching rate of 1 keV Ar^+ ions is determined using a SiO_2 overlayer on Si and is ~ 4 nm/min. The etching rate on Cu-Sb will change, because of the elements present and an unknown surface inclination. By probing similarly inclined planes on all fracture surfaces, at least a comparison between sputter times on different specimens is valid.

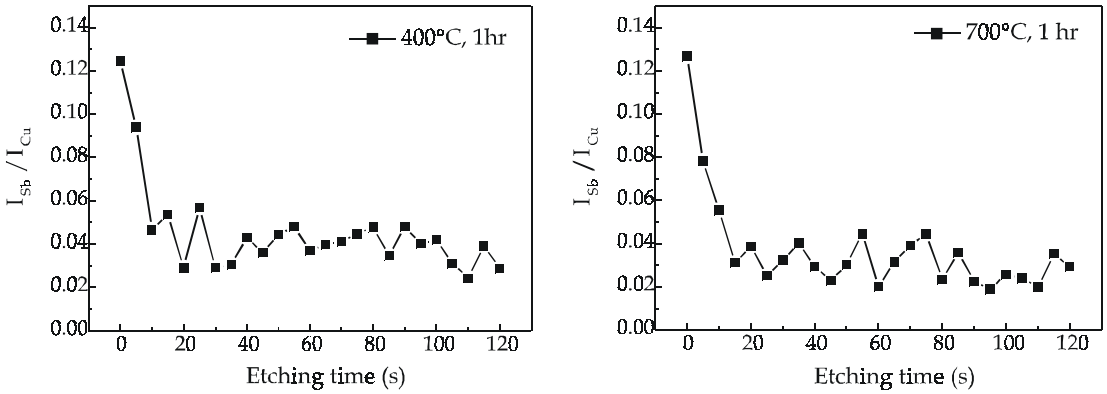

Figure 4.17: *Depth profiles on Cu-1.4 at.% Sb, heated at 400° (left) and 700° C (right) for 1 hour*

The two profiles in figure 4.17 show a similar decay of I_{Sb}/I_{Cu} with etching time, becoming constant after 20 seconds of Ar^+ etching. The intensity ratios at $t = 0$ are similar as well and are therefore unaffected by the heating temperature. An unaffected Sb content at the grain boundary is not in agreement with classical segregation theory that predicts a decrease of the amount of segregant with increasing temperature, due to a higher solid solubility and therefore a lower grain boundary enrichment ratio. However, it has to be pointed out that the content of Sb is rather high, which means that the amount of Sb at the boundary is not limited by the bulk amount, but by other factors such as the kinetics and the number of available segregation sites. Although the absolute segregation depth cannot be determined, it is clear that Sb enrichment exists over several atomic layers, justifying the assumption made in equation (4.5).

Figure 4.18 shows depth profiles of Cu-0.3 at.% Sb and Cu-0.8 at.% Sb, heated for 1 hour at 400° C.

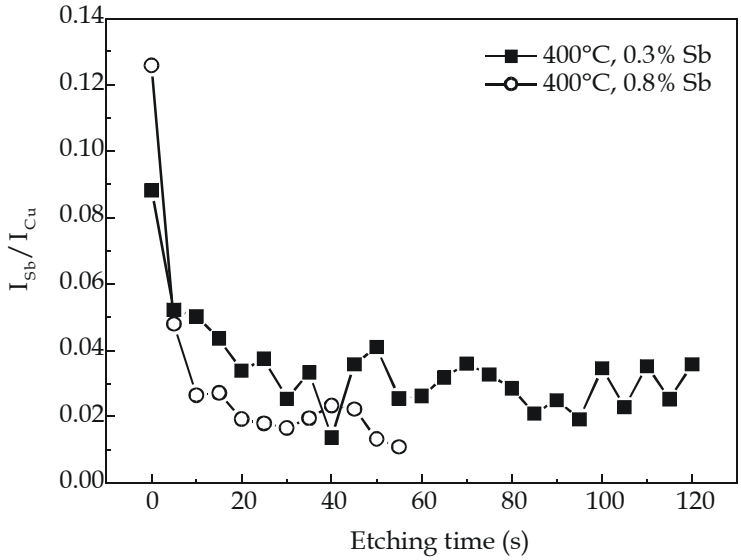

Figure 4.18: *Depth profiles of Cu containing 0.3 and 0.8 at.% Sb, heated at 400° C for 1 hour*

Figure 4.18 shows that both profiles decay similarly, the only difference being the higher amount of Sb at the surface with increasing bulk amount of Sb. Since equilibrium should be attained for the depth profiles of figures 4.17 and 4.18, monotonic exponentially decaying depth profiles are expected [37]. Depth profiles deviating from simple exponential have also been reported in the literature including Gaussian as well as more complicated forms [38,39]. On differently inclined surfaces, like the planes on the right in figure 4.16, the etching time necessary to obtain a constant Sb/Cu intensity ratio is more than

twice as high as that depicted in figures 4.17 and 4.18. This is caused by the grazing incidence of these surfaces with respect to the ion-gun.

With decreasing Sb concentration, the amount of transgranular fracture increases, as was concluded from observations of the fracture surfaces. This indicates the significant effect of the presence of Sb on the fracture mode of Cu, even at low temperatures.

Finally, figure 4.19 shows depth profiles after heating to 250° C for 1 and 10 hours. A broadening of the profile after longer heating times can be observed, together with a lower amount of Sb at t = 0 after heating for 10 hours. After heating for 1 hour, the Sb intensity at t = 0 is higher than after heating to 400 and 700° C, as expected.

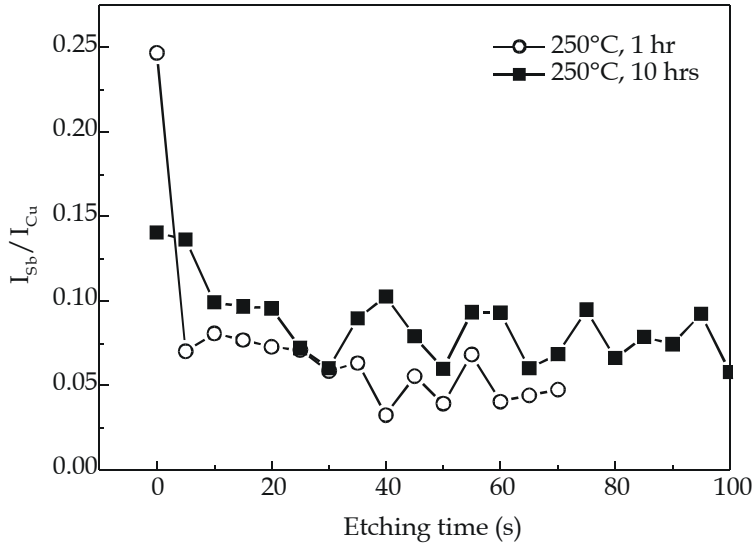

Figure 4.19: *Depth profiles on Cu-1.4 at.% Sb after heating at 250° C for 1 and 10 hours*

After 1 hour annealing at 250° C, the boundary composition is probably not much different from that achieved by the slow cooling process after homogenization at 750° C.

4.5 CONCLUSIONS

In conclusion, it can be stated that segregation of Bi and Sb to grain boundaries in Cu leads to embrittlement. At grain boundaries in Cu-Sb, there is no site competition between the solute, Sb, and sulfur that was present as an impurity in this material. In pits that are exposed by in situ fracture, site competition

between S and Sb is observed. The pits show facets and step terrace structures surrounding the facets, with shapes and symmetry that resemble the *fcc* structure of the copper matrix. In small pits, only facets are observed, whereas in larger pits step-terrace structures are necessary to accommodate to the larger pit size and still minimize the surface energy. The pit size therefore forms a lower boundary for the presence of step-terrace structures. S is found to segregate preferentially to high index surfaces. The sulfur intensity is higher on {135} planes than on {111} planes. The crystallographic orientations of the surfaces within the pits are determined by a combination of scanning Auger microscopy, atomic force microscopy and crystallographic arguments based on shape and symmetry of the surfaces. AFM height images can be used to obtain the angles between facets by converting the height derivatives in a histogram. Because sulfur-vacancy complexes have a very high mobility in copper and sulfur has a strong tendency to segregate to free surfaces, it is believed that sulfur segregates faster than antimony and occupies the high index planes first.

The addition of 1 at.% Bi to Cu leads to precipitation of Bi. At fracture surfaces of Cu-1 at.% Bi, the density of Bi precipitates that is observed is higher than the density of pits on a Cu-Sb surface, but of the same order of magnitude. This leads to two conclusions. Firstly, precipitation of Bi in voids leads to the formation of weak spots, promoting fracture. Secondly, not all pits in the Cu-Sb specimens could have been filled with Cu_2S precipitates before fracture, because the sulfur content is at an impurity level, whereas 1 at.% Bi is available to form precipitates.

Finally, the quantification of the amount of Sb in grain boundary segregation studies is hampered by the inhomogeneity of the region of analysis. A correction factor is introduced, for which the Sb segregation depth and inclinations of the measured surfaces have to be known. Estimations of the correction factor indicate significant errors in the *(P–B)/B* Auger images. Segregation studies on similarly inclined planes, to minimize these errors, show that the amount of Sb at the grain boundary increases with increasing bulk content and with decreasing heating temperature. Comparing 700 and 400° C, the Sb amount at the grain boundary does not change. At 250° C, the profile broadens and $I_{Sb}(0)$ decreases with increasing heating time.

REFERENCES

1. W. Hampe, Z. Berg-, Hütten- u. Salinen-Wesen **22** (1874) 93
2. E. Voce, A.P.C. Hallowes, J. Inst. Metals **73** (1947) 323
3. D. McLean, J. Inst. Metals **73** (1947) 791
4. V.J. Keast, D.B. Williams, Acta Mater. **47** (1999) 3999
5. A. Joshi, D.F. Stein, J. Inst. Metals **99** (1971) 178
6. B.D. Powell, H. Mykura, Acta Metall. **21** (1973) 1151
7. B.D. Powell, D.P. Woodruff, Phil. Mag. **34** (1976) 169
8. H.L. Meyerheim, H. Zajonz, W. Moritz, I.K. Robinson, Surf. Sci. **381** (1997) L551
9. D.J. Chakraborti, R.E. Laughlin, Bull. Alloy Phase Diag. **5** (1984) 148
10. M. Hansen, Constitution of Binary Alloys, McGraw-Hill (1958)
11. J. Bruley, V.J. Keast, D.B. Williams, Acta Mater. **47** (1999) 4009
12. M.P. Seah, E.D. Hondros, Proc. Roy. Soc. **A335** (1973) 191
13. R.W. Balluffi in Interfacial Segregation (Eds. W.C. Johnson, J.M. Blakely), American Society for Metals, Metals Park, OH (1979)
14. M. Menyhard, C.J. McMahon Jr, Scripta Metall. **25** (1991) 935
15. M. Menyhard, C.J. McMahon Jr, P. Lejcek, V. Paidar, Acta Metall. **39** (1991) 1289
16. D.J. Chakrabarti, D.E. Laughlin in Binary Alloy Phase Diagrams, 2nd edn, ed. T.B. Massalski, ASM International (1990) p.1467
17. P.A. Korzhavyi, I.A. Abrikosov, B. Johansson, Acta Mater. **47** (1999) 1417
18. M.P. Butron-Guillen, J.G. Cabanas-Moreno, J.R. Weertman, Scripta Metall. **24** (1990) 991
19. D. van Dyck, C. Conde-Amiano, S. Amelinckx, Physica Status Solidi **A58**, (1980) 451
20. J.N. Gray, R. Clarke, Phys. Rev. B **33** (1986) 2056
21. R. Berger, R.V. Bucur, Solid St. Ionics, **89** (1996) 269
22. O. Madelung (ed.), Diffusion in Solid Metals and Alloys, Springer-Verlag, Berlin (1991)
23. S. Tanuma, C.J. Powell, D.R. Penn, Surf. Interface Anal. **11** (1988) 577
24. D.T.L. van Agterveld, G. Palasantzas, J.Th.M. De Hosson, Acta Mater. **48** (2000) 1995
25. J.B.J.W. Hegeman, B.J. Kooi, H.B. Groen, J.Th.M. De Hosson, J. Appl. Phys. **86** (1999) 3661
26. D. Schleef, D.M. Schaefer, R.P. Andres, R. Reifenberger, Phys. Rev. B **55** (1997) 2535
27. A. Savitsky, M.J.E. Golay, Anal. Chem. **36** (1964) 1627
28. M.P. Seah, J. Vac. Sci. Technol. **17** (1980) 16
29. B. Joseph, F. Barbier, G. Dagoury, M. Aucouturier, Scripta Mater. **39** (1998) 775

30. D.E. Mouzakis, F. Stricker, R. Mulhaupt, J. Karger-Kossis, J. Mater. Sci. **33** (1998) 2551
31. A.P. Sutton, R.W. Balluffi in Interfaces in Crystalline Materials, Oxford University Press, New York (1995)
32. D. McLean, Grain Boundaries in Metals, Oxford University Press, London (1957)
33. M.P. Seah in Practical Surface Analysis, Vol. 1 (Eds. D. Briggs, M.P. Seah), John Wiley & Sons Ltd., Chichester, UK (1983)
34. H. Giordano, O. Alem, B. Aufray, Scripta Mater. **28** (1993) 257
35. V.A. Gorbatchev, S.M. Klotsman, YA.A. Rabovskev, V.K. Talinskiy, A.N. Timofeyev, Phys. Met. Metall. **35** (1973)
36. L.-S. Chang, E. Rabkin, S. Hofmann, W. Gust, Acta Mater. **47** (1999) 2951
37. S. Ouannasser, L.T. Wille, H. Dreysse, Phys. Rev. B **55** (1997) 14245
38. J.L. Morán–López, F. Mejía–Lira, K.H. Bennemann, Phys. Rev. Lett. **54** (1985) 1936
39. V. Drchal, J. Kudmovský, A. Pasturel, I. Turek, P. Weinberger, Phys. Rev. B **54** (1996) 8202

Chapter 5

BORON SEGREGATION IN Ni_3Al

5.1 INTRODUCTION

The nickel-aluminide Ni_3Al is an $L1_2$ (*Strukturbericht* notation, i.e. Pm3m) ordered intermetallic compound that remains ordered up to the melting temperature [1,2]. The unit cell of Ni_3Al is *fcc* based. The face centered cubic structure can be regarded as consisting of four interpenetrating simple cubic sublattices, all occupied with the same atoms. In the $L1_2$ structure, nickel atoms occupy three sublattices and Al atoms the remaining one.

The aluminide bears unique properties that make it especially attractive for high temperature applications [2]. Unlike disordered alloys, the flow stress of single crystalline Ni_3Al increases with increasing temperature, reaching a maximum value at 900 – 1000 K. The generally accepted model that describes this anomalous behavior is the formation of Kear-Wilsdorf locks at elevated temperatures [1]. Furthermore, at high temperatures the base material is protected from corrosion by the formation of a protective aluminum oxide film on the surface. Ni_3Al forms the most important strengthening constituent up to about 1100 K, the γ'-phase, in modern Ni-base superalloys, where it forms small precipitates that affect the motion of dislocations, making the alloy more difficult to deform. The temperature dependence of the flow stress is valid for single crystalline Ni_3Al, which possesses a high ductility. However, polycrystalline Ni_3Al exhibits low ductility and brittle fracture at room temperature, which limits its applicability.

At room temperature, polycrystalline Ni_3Al undergoes brittle intergranular fracture after about 2% elongation in tensile tests [2,3]. This is not accompanied by any appreciable plastic deformation within the grains. This intergranular

fracture is not caused by impurity segregation to the grain boundaries, because Auger electron spectroscopy measurements indicate impurity free grain boundaries after in situ fracture [1,4]. The absence of harmful impurities at the grain boundaries and the fact that Ni_3Al slips on {111}<110>, which means that it has more than enough slip systems and therefore should not experience slip incompatibility at the grain boundaries, have lead to the assumption that grain boundaries in Ni_3Al are 'intrinsically weak' [5]. The low ductility at room temperature is an intriguing phenomenon, especially when it is compared to the high ductility of Cu_3Au, which has the same crystal structure.

Microalloying processes have been used in attempts to increase the ductility of Ni_3Al. Microalloying involves the addition of minute amounts of dopants, usually in the ppm range, to change and control the grain boundary chemistry and cohesion. A large number of dopants was added, amongst which were boron, carbon, titanium, magnesium, manganese and silicon. The addition of boron was found to be the most effective way of improving the ductility of polycrystalline Ni_3Al [2] and resulted in a large improvement of the formability and tensile ductility (up to 35% elongation at room temperature) [6]. Combined with thermomechanical treatments, a tensile elongation of more than 50% was reported [2]. Auger electron spectroscopy results showed that boron segregates to the grain boundaries in polycrystalline Ni_3Al [2]. Furthermore, it was observed that boron addition is most effective with respect to ductility if the bulk material is Ni-rich [2]. After the first observations of this phenomenon, the beneficial effect of boron grain boundary segregation has been the subject of several debates.

In this chapter, possible mechanisms for the improvement of mechanical properties of Ni_3Al by the addition of boron will be discussed, i.e. effects on grain boundary cohesion, slip transmission at boundaries and grain boundary character distribution. The effects of varying grain size, boron concentration, Ni-enrichment and grain boundary character distribution on the fracture behavior of Ni_3Al will be investigated by manufacturing specimens for in situ fracture in the JEOL JAMP 7800F. After in situ fracture, the Auger intensities of all elements present can be obtained. The material that shows appreciable ductility during in situ fracture will be used to manufacture specimens for tensile tests. With Orientation Imaging Microscopy (OIM) observations on these specimens before and after tensile testing, the deformation inside the grains and the processes near the grain boundaries can be examined.

Furthermore, a comparison between grain boundary and surface segregation of boron and sulfur, especially under the influence of chemisorbed oxygen at the fracture surface, will be performed. In earlier studies, boron was observed to segregate more strongly to grain boundaries than to free surfaces, a behavior that is opposite to that of sulfur, which is a common embrittling impurity in Ni_3Al [7]. Boron surface segregation was only observed after Ar^+-bombardment of a Ni_3Al surface (leading to Ni-enrichment due to preferential Al sputtering [8]) and annealing at high temperatures (~1100K) [7]. However, knowledge of boron segregation phenomena to clean surfaces under the influence of present oxygen at ambient temperatures and under ultra high vacuum (UHV) conditions is only scantly available. Surface oxidation of an alloy can influence surface segregation, because the presence of oxygen can act as a driving force leading to preferential segregation of one of the constituents [9].

5.2 THE BENEFICIAL EFFECT OF BORON

Ni_3Al without impurity segregation exhibits low ductility, while there are enough slip systems present, like in ductile *fcc* materials. The fact that the addition of B, which segregates to the grain boundaries, increases the ductility and changes the fracture mode to transgranular, indicates a change in properties at the grain boundary. A number of possible effects will be discussed separately, although it may be necessary to consider combinations of these effects.

5.2.1 Grain boundary cohesion

Grain boundaries in the strongly ordered Ni_3Al are intrinsically brittle, whereas this is not the case in pure or disordered *fcc* alloys, such as Ni and Al. A possibility is that the grain boundary cohesion is lower in the compound than in the corresponding *fcc* metal [10]. The grain boundary cohesive energy, or the ideal work of fracture, $2\gamma_{int}$ is defined as

$$2\gamma_{\text{int}} = 2\gamma_s - \gamma_b \qquad (5.1)$$

where γ_s is the energy of one of the free surfaces formed during fracture and γ_b is the grain boundary energy. Calculations of $2\gamma_{int}$ for a large number of boundaries in pure Ni and Ni_3Al using embedded atom type potentials did not show large differences between the two materials [11]. However, equation (5.1)

only applies to completely brittle materials for which there is no plastic deformation at all. Most metals do experience some plastic deformation during fracture, leading to blunting of the crack tip and subsequently an increase in the fracture strength. Therefore, the critical energy release rate of fracture, G_c, is given by

$$G_c = 2\gamma_{\text{int}} + \gamma_p \tag{5.2}$$

The energy associated with plastic deformation in the vicinity of the crack tip is given by γ_p. In order to determine the influence of the addition of boron, its influence on all terms has to be considered. Electron energy loss spectroscopy (EELS) results showed that boron lowered the Ni-Ni binding energy at a grain boundary [12]. Upon boron segregation, the L_2 edge of Ni (and therefore presumably the bonding) at the grain boundary was found to become like that of bulk Ni_3Al [13]. Because single crystalline Ni_3Al (with Ni_3Al bulk bonding only) is ductile, this was thought to enhance the ductility. The effect of boron on the surface energy has been studied by means of embedded atom methods [14]. Boron was found to decrease the surface energy as well, but to a lesser extent than the grain boundary energy. This is in agreement with experimental observations, which showed that boron segregates more strongly to grain boundaries than to surfaces [2]. The cohesive energy of a grain boundary is therefore expected to be higher in the presence of boron. Changes in the grain boundary cohesion with alloying have been correlated with the valency and atomic size differences between the constituents [15] and with the differences in electronegativity [16]. Both approaches are based on earlier work [17,18], in which it was suggested that the charge transfer between Ni and Al atoms withdraws charge from Ni-Ni bonds and weakens them. Segregated boron was assumed not to weaken the Ni-Ni bonds, but enhances bonding in the grain boundary region via Ni-B bonding. However, this is based on quantum mechanical calculations for small clusters of atoms and its validity for metallic solids is questionable [19]. The term γ_p is not a constant, but is usually much larger than the cohesive energy.

It was concluded by Chen et al. [11] that the grain boundary energies and cohesive energies of Ni and Ni_3Al do not differ much. The performed simulations yielded the lowest cohesive energies for Al-rich boundaries, because of a relatively large number of high energy Al-Al nearest neighbors across the boundary. The ordered $L1_2$ structure of Ni_3Al does not contain Al-Al

nearest neighbors. Although the bonding energies may be similar, the difference between pure Ni and Ni_3Al lies in the yield stress. The yield stress is much larger for Ni_3Al, which may lead to a lower γ_p. If the grain boundary cohesion is similar for two materials, the one with the higher yield stress will have a higher propensity toward brittle fracture [11,20]. Although this is based on the assumption that failure is controlled by either plastic flow or intergranular fracture, it indicates why Ni_3Al fractures intergranularly whereas pure Ni does not.

5.2.2 Bulk composition of Ni_3Al

The bulk composition of Ni_3Al-B is of crucial importance for the formability and ductility of the material. Without boron, all aluminides cracked during cold rolling [2]. Boron doped Ni-rich material with 24 at.% Al could be easily fabricated into sheets by cycles of cold rolling and annealing [2]. When the Al concentration increased to more than 25 at.%, sheet fabrication became impossible. Between 24 and 25 at.% Al, a decrease in tensile elongation from more than 50 % to less than 10 % was observed. This was accompanied by a change in fracture mode from transgranular to intergranular. A specimen containing 24.8 at.% Al and 0.3 at.% boron, with an average grain size of ~ 40 μm, yielded a tensile elongation of 18.5 %, whereas the fracture surface showed mainly intergranular fracture [2].

The amount of boron was observed to have a marked influence on the tensile properties. Ni-rich material containing less than 0.05 at.% B could not be fabricated without cracks. The solubility limit of boron in Ni_3Al is about 1.5 at.%; beyond this limit second phase particles were observed, with a composition of $Ni_{20}Al_3B_6$, together with a drop in ductility [2]. Between 0.1 and 1 at.% boron, the observed tensile elongation at room temperature was roughly the same (~ 40 – 50 %), with a maximum at ~ 0.5 at.% boron (52% elongation).

Due to the very high ordering tendency of Ni_3Al the $L1_2$ structure of the material remains preserved up to the grain boundaries [10]. As a consequence, the grain boundary structure is different from that in materials with lower ordering tendencies, where relaxation takes place in the boundary region and atoms cannot be uniquely assigned to one of the grains [21]. In Ni_3Al, relaxation of atoms near the boundary is very small and atoms can be clearly assigned to one of the grains. This leads to the formation of atomic size cavities at the grain boundary [21,22]. The cavities can serve as nuclei for intergranular cracks,

which can easily propagate because the dislocation mobility is low, due to the high ordering tendency. At high temperatures they can lead to void formation. When the bulk material is Ni-rich, the grain boundaries become enriched with Ni and chemical disorder can occur at the boundary. The atomic structure of the grain boundary becomes more like that of an *fcc* material and the number of cavities decreases. The disorder spreads into several layers adjacent to the boundary, leading to less nuclei for cracks and enhanced dislocation mobility in the direct vicinity of the boundary [10].

Experiments on Al-rich material yielded very low ductilities. Grain boundary segregation of Al is much more difficult than that of Ni, because of the large difference in lattice parameter between Al (4.05Å) and Ni_3Al (3.52 Å), while the difference between Ni (3.57 Å) and Ni_3Al is much smaller. Therefore, it is easier to attain a Ni-rich boundary without significant mismatch [10]. The beneficial effect of boron can consist of attracting Ni to the boundaries by co-segregation [23], leading to more *fcc*-like grain boundaries.

5.2.3 Grain size and grain boundary character distribution

The effects of grain size and grain boundary character distribution are studied simultaneously, because it has been observed that the fraction of special boundaries, where a CSL lattice and parameter Σ can be defined, increases with decreasing grain size [24]. The effect of boron on the hardness and ductility of Ni_3Al is different for large and small grained specimens [25]. Experiments on stoichiometric Ni_3Al with or without 0.35 at.% boron showed that upon boron addition the measured hardness increases for coarse grained material, but decreases for fine grained Ni_3Al, with a transition at average grain sizes of ~ 10 μm. The effect of boron addition on the measured yield strengths of Ni_3Al was the same. Both experiments were performed at room temperature [25]. Many materials show a variation of yield strength σ_y with size according to

$$\sigma_y = \sigma_0 + k_y d^{-1/2} \tag{5.3}$$

where σ_0 and k_y are constants for a particular material and d is the average grain size. This means that with decreasing grain size both hardness and yield strength increase. Although the yield strength of Ni_3Al has been observed to be proportional to $d^{-0.8}$ [26], the variation in hardness was proportional to $d^{-0.5}$. The effects of interstitial boron are an increase in the constant σ_0, through the effect

on lattice friction and a decrease of k_y, which was assumed to be caused by a decrease of the grain boundary resistance to slip.

Grain refinement of undoped Ni_3Al did not lead to an increase in ductility at room temperature, whereas decreasing the grain size of boron doped Ni_3Al below 20 μm lead to an increase in ductility. The undoped specimens fractured intergranularly after less than 3% tensile elongation. The elongation of boron doped specimens increased from ~10% to ~30% upon grain refinement [25].

Although, as discussed in chapter 2, the classification of grain boundaries by its Σ value is incomplete because of the lack of knowledge of the grain boundary plane, the correlation between Σ value and boundary properties has been studied. The first experiments in this direction showed that the relative amount of Σ3 boundaries was lower along an induced crack than in the rest of the material [27]. Similar experiments with a large number of grains showed that only the Σ3 boundaries are resistant to cracking. All other low Σ boundaries did not appear very strong [28]. The geometry of Σ3 boundaries is such that the number of atomic size cavities at the grain boundary is zero. In addition, the number of energetically unfavorable (compared to Ni-Al) Al-Al nearest neighbors across the boundary is low.

Through unidirectional solidification by zone melting, a fraction of 29% of Σ3 boundaries could be obtained in undoped Ni_3Al [29]. This material yielded a tensile ductility of more than 50%. When these specimens were rolled and recrystallized, the fraction of Σ3 boundaries in undoped Ni_3Al boundaries decreased, accompanied with a decrease in ductility. If the fraction of 'strong' boundaries is higher than 1/3, a propagating crack can be halted at a triple junction (the place where three grain boundaries meet), because, on average, at least one Σ3 boundary adjoins every triple junction [24].

The shape of the grains can be important as well. It has been shown that undoped, directionally solidified Ni_3Al with columnar grains can yield a reasonably high ductility without a large fraction of Σ3 boundaries, as long as it is tested parallel to the growth direction [30].

5.2.4 Dislocation motion in Ni_3Al

The aforementioned effects can be related to the extreme ordering tendency, the difficulty with which dislocations move within Ni_3Al and the reactions that

take place at the grain boundaries. The plastic work term in equation (5.2) is governed by the ease with which cracks can be blunted by the emission of dislocations. Dislocation motion is much more difficult in strongly ordered $L1_2$ compounds than in *fcc* metals, because it will introduce energetically unfavorable anti-site defects. The effects of deviation from stoichiometry have been interpreted by a calculation of the energies of anti-site defects [22]. In the bulk, it is energetically unfavorable to deviate toward a surplus of Ni, whereas it is favorable to accommodate a surplus of Al. This means that in Al-rich material the grain boundary will remain almost stoichiometric, whereas in Ni-rich material the grain boundary will be Ni-rich, leading to chemical disorder. This facilitates dislocation motion, because no anti-site defect has to be introduced.

The decrease of k_y in equation (5.3) after the addition of boron has to be considered in the light of dislocation reactions at the grain boundary. Upon grain refining, a material becomes harder and has a higher yield strength, because grain boundaries hinder dislocation motion. When a moving lattice dislocation meets a grain boundary, it can either be absorbed (i.e. dissociated into grain boundary dislocations) or transmitted. This mechanism is the same for *fcc* and $L1_2$ ordered materials, but the resistance to dislocation movement increases with increasing ordering tendency [31-34]. In the case of absorption, the movement of grain boundary dislocations creates anti-site defects in the grain boundary plane. Transmission occurs at high stress levels, leading to stress concentrations at the grain boundary, which increase with increasing ordering tendency.

The influence of boron addition, which is only effective in Ni rich material, can therefore be attributed to the chemical disorder at the grain boundary. Boron can attract segregating Ni, which leads to even more disorder in the grain boundary plane. Therefore, the movement of a grain boundary dislocation does not longer create anti-site defects, facilitating absorption, and slip can be transmitted under reduced stresses.

5.3 MATERIALS PREPARATION

Stoichiometric polycrystalline Ni_3Al and Ni_3Al-B specimens are obtained from Highways International, whereas Ni-rich Ni_3Al-B is homemade by arc melting the pure constituents. The dimensions of the stoichiometric specimens are such that the specimens are ready for in situ fracture in the JAMP 7800F. Apart from

a homogenization treatment, no further rolling and recrystallization treatments are performed. The homemade specimens are subjected to different homogenization and thermomechanical treatments, in order to manufacture material that possesses some ductility.

The chemical compositions of all used specimens, weighed before melting, are shown in Table 5.1. Also given are the homogenization heat treatments and subsequent cold rolling (R, ~10% thickness reduction for every rolling cycle) and annealing treatments, performed to optimize parameters such as boron segregation and average grain size [35]. If the reduction in thickness during cold rolling is more than ~10%, cracks become visible at the specimen surface. Therefore, several thermomechanical cycles are necessary. The numbers given for homemade material indicate batch numbers, because not every batch is used. Cylindrical samples, suitable for in situ fracture, are cut out of the ingot and inserted into the JEOL JAMP 7800F, where the in situ fracture experiments are executed. Both stoichiometric and Ni-rich specimens are cylindrically notched to localize fracture. Except for the specimens of batch 2, which are fractured at liquid nitrogen temperature, all other specimens are fractured at room temperature.

Table 5.1: *Weighed compositions and heat treatments of Ni_3Al(-B) alloys.*

	Ni_3Al Highways	Ni_3Al-B Highways	Ni_3Al-B Homemade		
Batch #			2, 4	5, 6, 7	18, 21
Ni (at.%)	75	74.7	76.5	75.2	75.9
Al (at.%)	25	24.8	22.5	24.0	23.9
B (at.%)	-	0.5	1.0	0.8	0.2
Homogeni-zation	1100° C, 24 h	1100° C, 24 h	1100° C, 24 h	1050° C, 8 h 900° C, 12 h 750° C, 8h	1050° C, 8 h 900° C, 12 h 750° C, 8h
Thermo-mechanical treatment				R, 1050°C, ½ h R, 700°C, 1h R, 700°C, 1h	R, 1050°C, ½ h R, 1050°C, 3 h R, 700°C, 1h

5.4 BORON AND SULFUR SEGREGATION IN Ni_3Al

Because boron segregation to grain boundaries has a beneficial effect on the room temperature ductility in polycrystalline Ni_3Al, the first objective is to

measure the amount of boron at grain boundaries. By fracturing the specimens intergranularly, which is facilitated by a circular notch around the specimens, former grain boundaries become fracture surfaces. A micrograph of an in situ fractured (at room temperature) boron doped specimen is shown in figure 5.1.

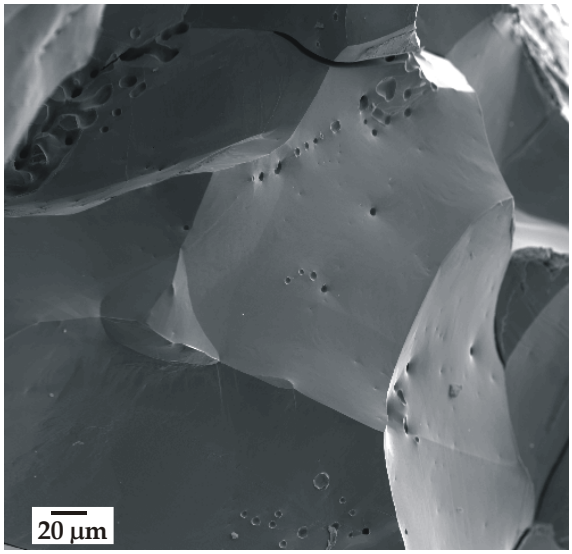

Figure 5.1: *In situ fractured boron doped Ni_3Al specimen (Highways material)*

All Ni_3Al specimens without boron fracture intergranularly, both at liquid nitrogen and at room temperature. The addition of boron does not drastically improve the ductility, i.e. the specimens still show, besides areas of transgranular fracture, mostly intergranular fracture. Also visible in figure 5.1 are the small pores on the surfaces, which are internal surfaces during processing. The B, Ni and Al Auger peak-to-peak heights are measured immediately after in situ fracture on a large amount of different facets, which yields an average relative boron intensity at the surface, i.e. the previous grain boundary. Within an hour after fracture, oxygen peaks start to develop. Furthermore, the pores can be used to study the difference between grain boundary and surface segregation of boron and sulfur. The presence of substitutional sulfur at grain boundaries has been calculated to be detrimental to the grain boundary cohesion in Ni_3Al, leading to embrittlement [36].

The probe size of the electron beam is found to have a drastic effect on the measured boron peak-to-peak height (at 180 eV in the differential spectrum). When the smallest possible probe size is used (i.e. ~15 nm), hardly any boron can be detected. An increase of the probe size to 5 or 10 µm causes the measured boron peak-to-peak height to become higher with respect to Ni, due to increased sampling and averaging of boron over larger areas. This can be

attributed to two phenomena. Firstly, the inhomogeneous distribution of boron at a grain boundary as was observed using electron energy loss spectroscopy [13]. Therefore, the use of a larger probe size yields a spatially averaged amount of boron. Secondly, the peak-to-peak height of boron decreases under the influence of a focussed electron beam, caused by electron beam enhanced surface oxidation [37].

The detected boron intensity is small immediately after fracture, but after several hours of exposure to the ambient pressure in the analysis chamber at room temperature, boron is observed to segregate to the surface. In figure 5.2 direct Auger spectra obtained one hour after fracture (oxygen chemisorption is already occurring) and 24 hours later (with the electron beam shut off during this time) are compared. The increase in the intensity of boron is clearly visible. Depth profiling by Ar^+-bombardment shows that boron-enrichment is only present within the outermost atomic layers. The Auger transitions used during these measurements are B (172eV, KLL), Ni (844 eV, LMM), O (503 eV, KLL), S (146 eV, LVV), and Al (1390 eV, KLL).

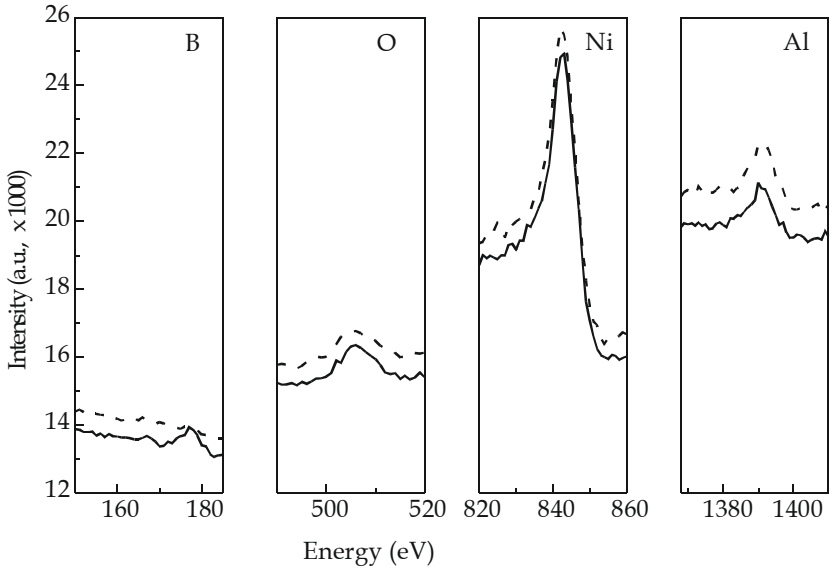

Figure 5.2: *Spectra of B, O, Ni and Al, one hour (dotted) and 24 hours after fracture (solid)*

Because the electron beam is directed away from the specimen between the measurements of figure 5.2, the oxygen intensity does not increase between 1 and 24 hours. Sulfur is present inside the small pores on the fracture surface visible in figure 5.1, whereas outside the pores it is absent. Figure 5.3 shows that the inside of a pore consists of facets, similar to pores in Cu-Sb that contained sulfur as well, as observed in chapter 4 of this thesis [38].

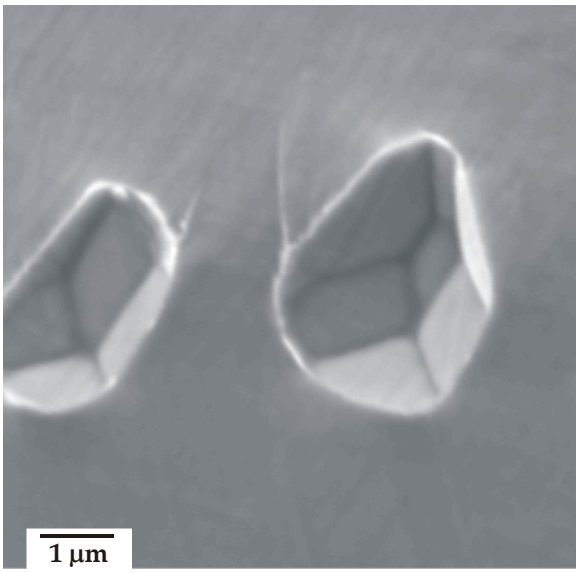

Figure 5.3: *SE image of the inside of pores in Ni_3Al*

The presence of sulfur on the pore surface in Ni_3Al is consistent with earlier observations [7], because the interior of a pore consists of free surfaces toward which sulfur preferably segregates during the heat treatment. Boron is not observed inside the pores. After prolonged exposure to the ambient pressure, the measured intensity of oxygen (relative to nickel) inside the pores is lower than that outside the pores. The presence of sulfur hinders oxidation, as was observed earlier [39]. Figure 5.4 shows an Auger map of sulfur, in which it is clearly visible that sulfur is localized inside the pores.

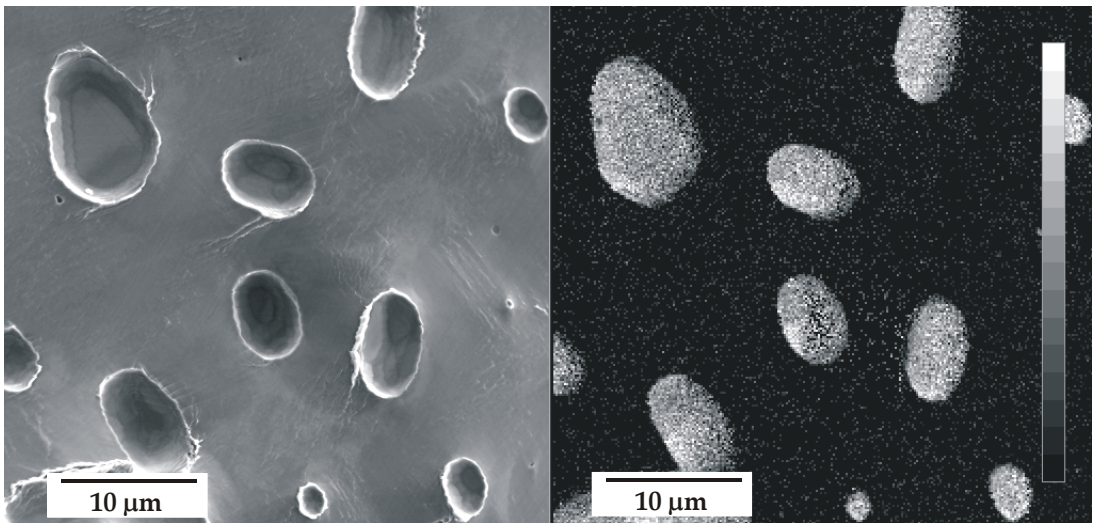

Figure 5.4: *SE image of pores on a Ni_3Al surface (left) and Auger image of sulfur (right)*

Similarly, on the only occasion where sulfur is found to be distributed over a grain boundary (instead of being localized in pores) the amount of oxygen and the boron enrichment after 24 hours exposure are less than on S-free surfaces (Figure 5.5, dotted lines).

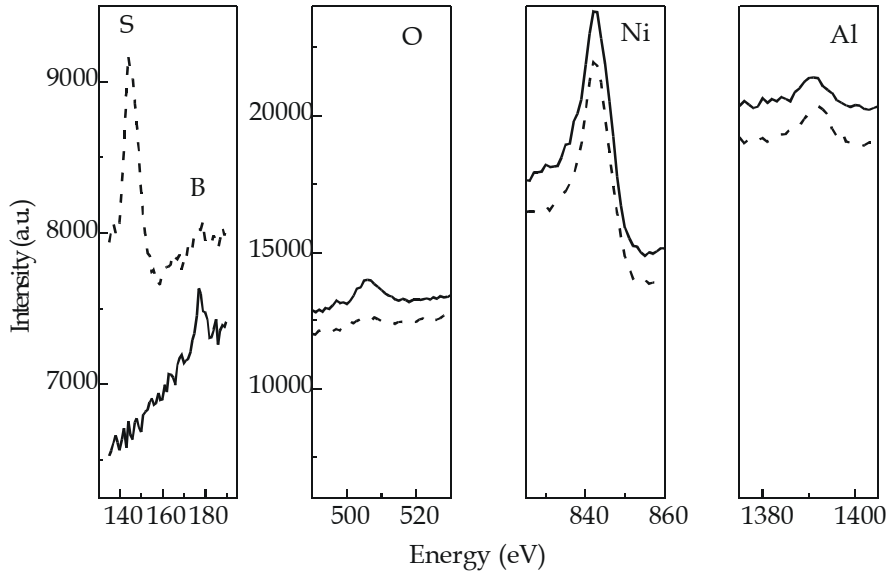

Figure 5.5: *Auger spectra of S, B, O, Ni and Al, after fracture and 24 hours exposure (dotted lines) and after subsequent Ar^+ sputtering followed by 24 hours exposure (solid lines)*

Upon sulfur removal by Ar^+-sputtering, which shows that it is confined to the topmost atomic layers of the material, followed by 24 hours exposure, a large increase in oxygen and boron intensities is observed (Figure 5.5, solid lines). The prolonged exposure (~24 hours with the e-beam shut off) to the ambient vacuum leads to oxygen chemisorption. The latter suggests a strong relation between boron surface segregation and oxygen chemisorption, as shown in chapter 3 of this thesis.

Figures 5.2 and 5.5 show direct spectra of all elements present. In order to obtain some quantitative information, Auger peak-to-peak heights are extracted from the differential spectra. In the past, the observed increase in ductility of Ni_3Al by boron addition was shown to be related to Ni enrichment at the grain boundaries [2]. In order to determine whether boron and Ni co-segregate to grain boundaries, which is an important assumption in several theories that explain the ductilizing effect of boron, the boron and Ni concentrations at grain boundaries have to be obtained.

Therefore, in figure 5.6 the B/Ni ratio of peak-to-peak heights is plotted as a function of X_{Ni}, the 'concentration' of Ni at the grain boundary.

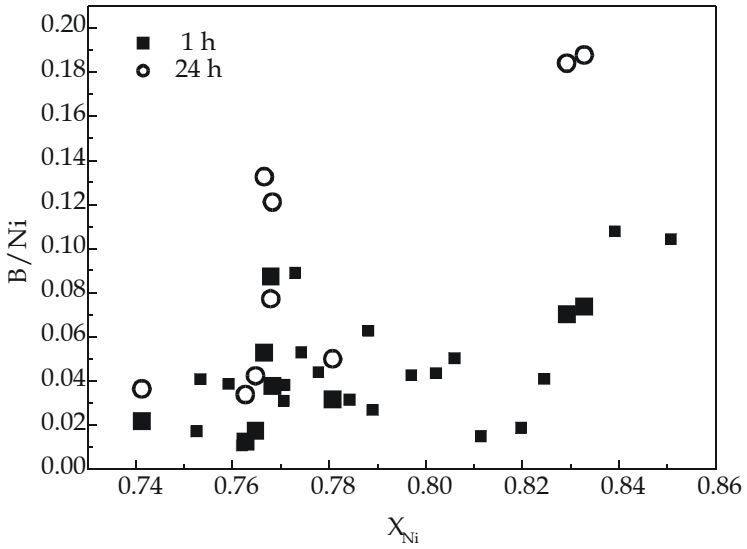

Figure 5.6: *Ratio of boron and nickel peak-to-peak heights as a function of the calculated X_{Ni} at the grain boundary / surface for homemade material, #21.*

X_{Ni} is calculated using equation (2.13) for a binary Ni-Al system, taking only Ni and Al intensities into account and assuming a homogeneous distribution of Ni and Al. Because of these simplifications, the absolute values of X_{Ni} are approximations, but higher values do mean that there is more Ni present at the boundary. The ratio of intensities B/Ni is plotted versus X_{Ni}, which means that at points where X_{Ni} is higher, the amount of boron is relatively higher. Black squares in figure 5.6 represent measurements during the first hours after fracture. The larger squares symbolize measurements within the first hour on some surfaces that are repeated 24 hours later, on the same surfaces. The results after 24 hours are represented by the circles in figure 5.6. In this way, the increase in B/Ni ratio as a function of Ni-enrichment at the boundary can be visualized. It seems that the increment in B/Ni ratio between 1 and 24 hours after fracture is higher for grain boundaries with a higher X_{Ni}.

This material (batch #21, ~76 at.% Ni) is Ni-rich, which explains the Ni-enrichment at most grain boundaries. In most cases the B/Ni ratio increases drastically after 24 hours exposure to the ambient vacuum in the analysis chamber. During the time between the measurements, the surface is not irradiated by the electron beam. The scattering in B/Ni ratios is most probably caused by the distribution of grain boundary structures in the polycrystalline alloy, statistical effects (e.g. noise in the obtained spectra) and the inclinations of the exposed surfaces with respect to the detection unit, combined with the presence of more than two elements, as discussed in chapter 4.

Similar measurements on stoichiometric material containing boron (Highways material) yield figure 5.7. The distribution of X_{Ni} in figure 5.7 is centered around the stoichiometric composition, X_{Ni} = 0.75. It is clear that for X_{Ni} > 0.75 the amounts of B at the grain are higher than for X_{Ni} < 0.75. The increase in B/Ni ratio after 24 hours is also higher on the Ni-rich side of the graph. This clearly shows that there is a strong correlation between Ni-enrichment at a grain boundary or surface and the facility with which boron atoms can segregate to the boundary or surface. The observed B/Ni ratios are quantified using

$$\Gamma_A = m\, K_{AB} \frac{I_A}{I_B} \tag{5.4}$$

assuming a binary Ni-B system, monolayer B coverage and a Ni concentration of 75 at.%. Averages of the points measured within the first hour and those measured 24 hours later are used. An average inclination of 30° is assumed (specimen tilt angle) and the parameters are λ_B(180 eV) = 5.7 Å [40], a_B = 1.9 Å, r_B(180 eV) = 0.37, r_{Ni}(180 eV) = 0.90, I_{Ni}^{∞} = 1859 and I_B^{∞} = 592. For the quantification of the points within the first hour after fracture m = 2 is used. This yields the amount of boron that was present at the original grain boundary. However, what is left on the surface is half of that amount, on average. After 24 hours, extra boron has segregated to the surface. Therefore, the increase in B/Ni ratio is converted to coverage using equation (5.4) with m = 1. The results are shown in table 5.2.

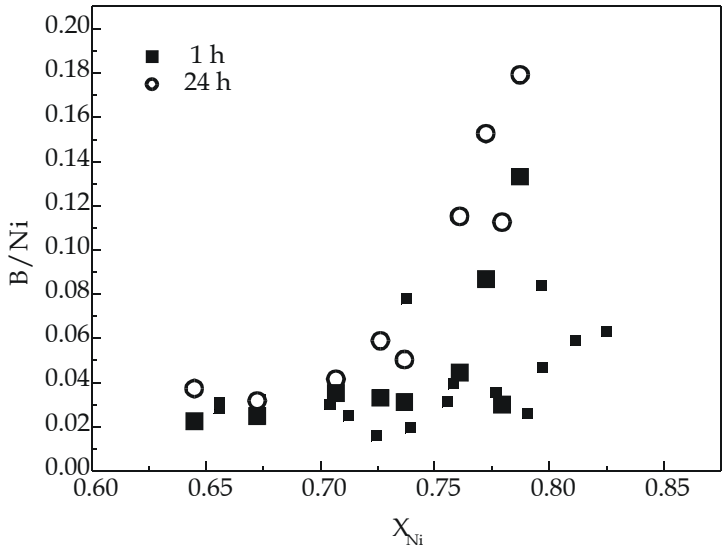

Figure 5.7: *Ratio of boron and nickel peak-to-peak heights as a function of the calculated X_{Ni} at the grain boundary / surface in a stoichiometric alloy*

Table 5.2 shows that, although the B/Ni intensity ratios are rather low, the calculated boron coverages are significant. It is assumed that during the fracture process each of the separated surfaces retains on average half of the amount of segregants. The calculated boron coverage after 24 hours is increased due to surface segregation at room temperature and is almost twice as high as immediately after fracture. It was observed earlier that boron diffusion in Ni_3Al can become 10^4 times faster than Ni self-diffusion [41].

Table 5.2: *Measured B/Ni intensity ratios and calculated coverages*

	Within 1 hour after fracture (GB: m = 2, S: m = 1)			24 hours after fracture (m = 1)	
	I_B/I_{Ni}, avg	Γ_B GB (ML)	Γ_B S (ML)	I_B/I_{Ni}, avg	Γ_B (ML)
Ni_3Al-B (Highways)	0.050	0.44	0.22	0.082	0.36
Ni_3Al-B (Homemade)	0.045	0.40	0.20	0.090	0.40

In order to explain the surface segregation of boron at room temperature, the terms influencing surface segregation are considered. In the presence of oxygen on a surface, a description of the free energy of surface segregation in terms of bond energy and strain release terms is no longer sufficient [42]. When chemisorbed gaseous species are present, the chemisorption energies of that species on the different constituents of the covered material have to be taken into account. The driving force for surface segregation becomes higher for the elements with higher chemisorption energies. The influence of chemisorbed oxygen at the surface can therefore be best expressed by comparing the bond energies of B-O (195 kcal/mol), Ni-O (87 kcal/mol) and Al-O (107 kcal/mol) [43]. From the high B-O bond energy, it is clear that the presence of oxygen at the surface can lead to chemisorption induced segregation of boron. However, the effect is more pronounced when Ni enrichment is present as well, which is an indication of interaction between the two elements.

Boron segregation to a Ni-rich surface will, depending on the crystallography of the surface, lower the surface energy by locally restoring Ni-Al bonding, with boron acting as a small Al atom [44]. This explains that when $X_{Ni} < 0.75$ the measured intensities of boron are smaller and the increase after 24 hours is not so drastic, compared to $X_{Ni} > 0.75$, because that will lead to Ni-rich grain boundaries and thus to Ni-rich fracture surfaces. Furthermore, Ni-enrichment causes chemical disorder close to the grain boundary (i.e. structural order is

preserved until the boundary, but some Ni atoms occupy Al sites), facilitating boron diffusion through the aforementioned bonding arguments. At Al-rich bulk compositions, the grain boundaries remain almost stoichiometric [10,22]. This anisotropy in grain boundary composition makes boron segregation to grain boundaries in Al-rich material less likely, which is confirmed experimentally [2].

In order to clarify the effects of the presence of sulfur, the present results are compared to earlier work of White and Choudhury [7]. In their work, only bulk concentrations of sulfur of 50 ppm or more yielded detectable amounts of sulfur at grain boundaries. However, sulfur was present in pores (internal surfaces) and segregated to the surface during annealing at 1273 K. Only after 16 cycles of heating to 1273 K and Ar^+ bombardment a sulfur-free surface could be obtained. When this surface was again heated to 1273 K, no boron surface segregation was observed. Boron did however segregate to the surface when the sulfur-free surface was sputtered and subsequently heated to temperatures between 873 and 1073 K. This effect was assumed to be caused by remaining sputter damage or Ni-enrichment by preferential sputtering, enabling boron surface segregation. Indeed, preferential sputtering of Al was found to occur in Ni_3Al. The ratio of sputtering yields of Ni and Al was found to be ~0.7 [8]. Upon heating to 1273 K, long-range structural order was re-established and boron was not observed to segregate to the surface [7].

In our study, segregation of boron to the surface is also only observed on sulfur-free surfaces, such as previous grain boundaries or pores after the removal of sulfur. This is attributed to a change in surface energy by the presence of sulfur, which diminishes the tendency for boron segregation and the absence of another driving force for boron surface segregation: chemisorbed oxygen. The presence of sulfur leads to considerably less oxygen coverage, because both elements have similar electronegativities [45].

During processing of the Ni_3Al alloys the temperature is high enough for substitutional sulfur to diffuse to the pore surfaces. However, at room temperature the tendency for sulfur surface segregation may still be present, but the kinetics of segregation are limiting the process. Furthermore, both driving forces mentioned for boron segregation, i.e. an oxidized surface and the presence of Ni-enrichment, are not effective for S surface segregation. Therefore, at room temperature, with chemisorbed oxygen and Ni-enrichment present, B will segregate to the surface whereas S will not.

5.5 MECHANICAL PROPERTIES OF Ni_3Al

In this section, the influences of the addition of boron on the mechanical properties of Ni_3Al will be discussed within the framework of section 5.2.

5.5.1 Bulk composition of Ni_3Al-B

All stoichiometric specimens fracture intergranularly in the JAMP 7800F, irrespective whether boron is added or not. The homemade Ni-rich specimens show mixed transgranular and intergranular fracture. Boron doped material can be cold rolled to some extent (~10% reduction in thickness), whereas it is impossible to deform undoped Ni_3Al without cracking. Therefore, the addition of boron imparts some ductility to the material.

The modest increase in ductility raises the question whether the assumed amount of boron, determined by weight before melting, is indeed present in the material. The bulk content of boron is too low to be measured with the JAMP 7800F (~0.8 at.% B). Therefore, both Atom Probe Field Ion Microscopy (APFIM) and Neutron Depth Profiling (NDP), based on the very effective reaction of boron with incident neutrons [46,47], are employed to determine the bulk content of boron. Both techniques yield a boron concentration of ~1 at.%, which is constant throughout the measured depths. The batches with lower desired boron contents indeed yield lower bulk concentrations with NDP. Furthermore, APFIM reveals that boron is preferably surrounded by Ni atoms and that some hydrogen is detected in the bulk, irrespective of the surroundings.

The most important difference between the first (2,4) and following (5-7) batches is the addition of several thermomechanical cycles. After each cycle, the alloy is slowly cooled to optimize boron grain boundary segregation. Still, all these specimens can be fractured in-situ at room temperature, even when the specimens are not circularly notched. The obtained intensities of boron, relative to nickel, on the fracture surface are comparable to the values in table 5.2.

Only upon reducing the boron content to 0.2 at.% in the last batches (18,21), with similar thermomechanical treatments, specimens without a notch cannot be fractured in situ. Several attempts to fracture the specimen in situ lead to a large deformation of the cylindrical rod. A specimen that has been tried to fracture in situ is depicted in figure 5.8. From figure 5.8, it is clear that this material is fairly ductile, although the exact amount of deformation cannot be

determined. However, when the remainder of the rod is cylindrically notched and is inserted again, it fractures rather easily and the fracture mode is mixed.

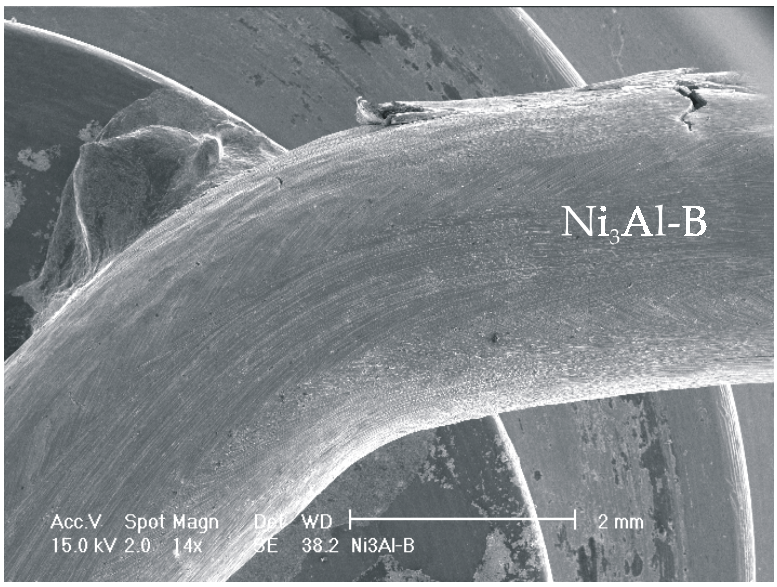

Figure 5.8: *Deformed Ni_3Al-0.2 at.% B rod after in situ fracture attempts*

Energy Dispersive X-Ray Spectroscopy measurements yield Ni-rich bulk compositions (76 ± 1 at.% Ni) for all homemade alloys. Figure 5.6 indicates Ni-enriched grain boundaries, where it has to be taken into account that a homogeneous composition with depth is assumed. Therefore, although several effects lead to a less accurate quantification, the grain boundary composition can even be higher than the values indicated in figure 5.6, which are averaged over several inelastic mean free paths of Ni ($\lambda \sim 1.3$ nm [40]).

5.5.2 Grain size and grain boundary character distribution

Figure 5.9 shows an example of the average grain size of as-cast undoped stoichiometric Ni_3Al, used for the experiments in this chapter. It is clearly visible in figure 5.9 that the average grain size is much higher than 100 µm. The original solidification structure is clearly visible as well. In order to compare the present results on segregation and ductility with previous work [2,25] the average grain size is reduced through several thermomechanical cycles, as indicated in table 5.1.

The evolution of grain size and shape distribution of Ni_3Al-0.2 at.% B is visible in the four backscattered electron images of figure 5.10, from homogenized as-cast material to material subjected to three thermomechanical cycles. All images

are polished cross sections of Ni_3Al-B and are obtained with the same magnification.

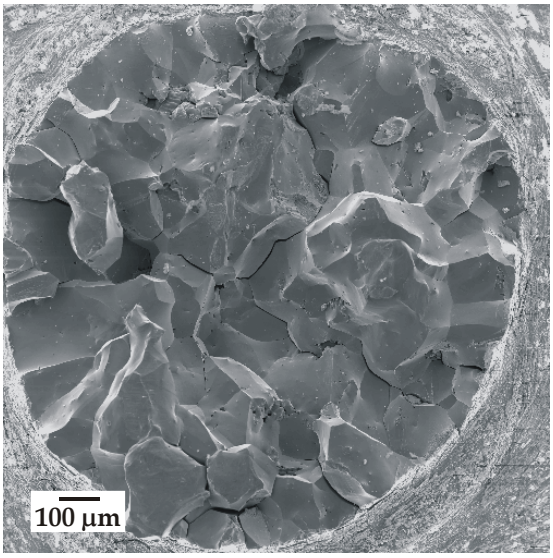

Figure 5.9: *Fracture surface of as-cast undoped Ni_3Al*

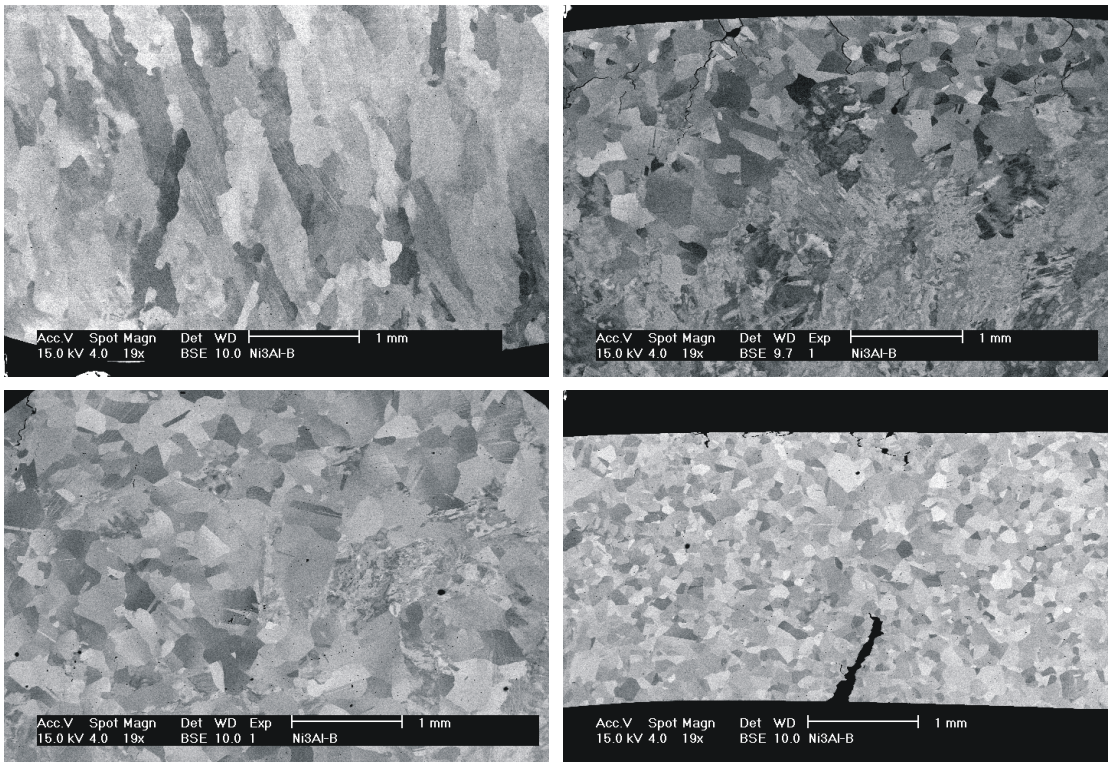

Figure 5.10: *Evolution of grain size and shape of Ni_3Al-0.2 at.% B after casting and homogenization (top left) + cold rolling, ½ h 1050° (top right) + cold rolling, 3 h 1050° (bottom left) + cold rolling, 1 h 700° (bottom right)*

After three thermomechanical cycles, grain refinement has occurred and the original solidification structure has disappeared. The deformation during cold rolling is higher near the surfaces than in the center, which leads to faster recrystallization but to the formation of cracks at the surface as well. The surface cracks are partly removed by grinding the specimens between thermomechanical cycles. The crack in the bottom right image is of an extreme size, which is only observed in this case. Although cracks are already present before introduction in the JAMP 7800F, this is the material that can be heavily deformed, as is visible in figure 5.8.

The reduction of the average grain size upon thermomechanical treatments is apparent from figure 5.10, eventually leading to average grain sizes of ~100 μm. However, the SE image by itself can sometimes be misleading. For example, figure 5.11 shows an image of a cross section of Ni_3Al-B after cold rolling (~10% reduction in thickness) and annealing at 700° C for one hour (batch 7). The surface is etched prior to insertion in the SEM.

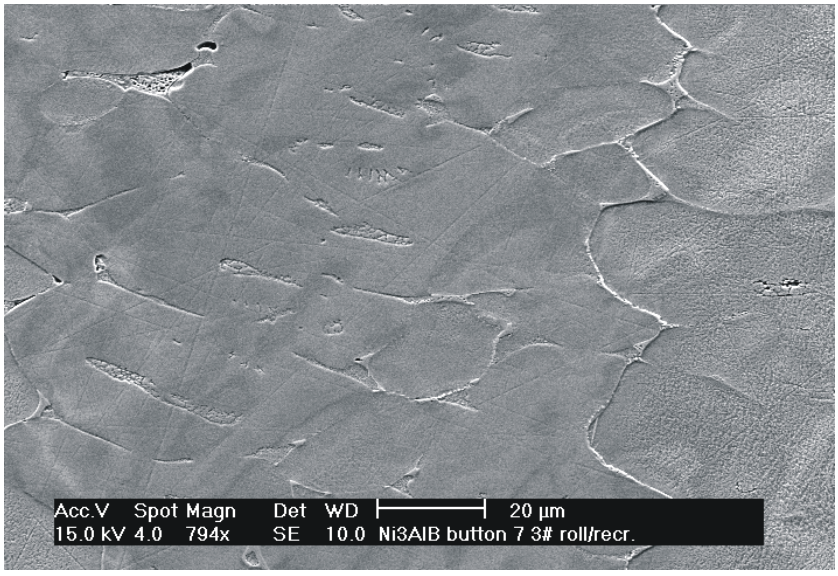

Figure 5.11: *SE image of cold rolled and annealed Ni_3Al-B*

Although it seems that grains of ~ 40 μm are present, possibly with a second phase decorating the grain boundaries, Orientation Imaging Microscopy (OIM) analysis in the Philips XL30S SEM reveals that this is an image of incomplete recrystallization. Figure 5.12 shows an Image Quality map obtained with OIM on this surface. The image quality of a point is a measure of the quality of the backscattered pattern and is therefore sensitive to changes in the lattice in the diffraction volume, such as grain boundaries, strained regions and different phases. The thick black lines are recognized as a grain boundary, i.e. a line that

separates next neighbors with a misorientation angle of more than 15°. The features that appear in the SE image as grain boundaries are actually band-like structures that exhibit a certain misorientation with respect to the undeformed large grain, which becomes clear through figure 5.13.

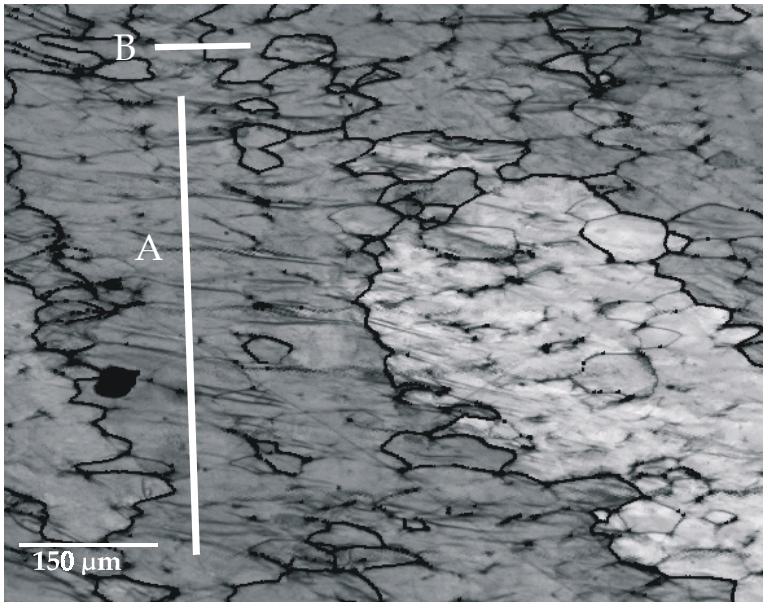

Figure 5.12: *OIM image quality map of cold rolled and annealed Ni_3Al-B*

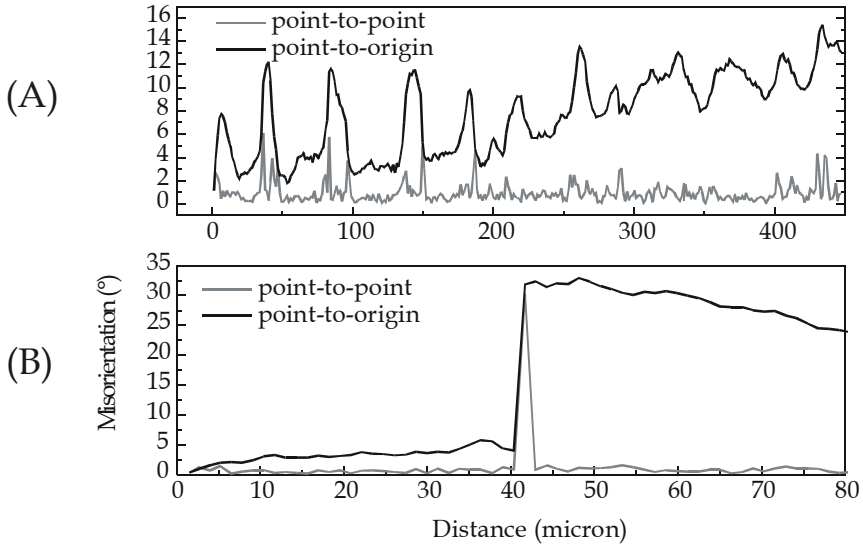

Figure 5.13: *Misorientation profiles inside a large grain (A) and across a grain (B)*

Figure 5.13 shows misorientation profiles inside a grain along the vertical line in figure 5.12 and across a grain boundary, along the horizontal line in figure 5.12. In order to be classified as a grain boundary, the point-to-point misorientation has to exceed 15°, which is not the case in the upper profile, but is clear in the lower profile. The upper profile shows that the bands are characterized by a

steep increase and decrease of point-to-origin misorientation, superimposed on a gradual increase in point-to-origin misorientation, which is indicative of an orientation gradient within a grain. The lower profile shows a gradient as well.

The occurrence of cracks after cold rolling and annealing treatments allows the observation of the influence of the grain boundary character distribution on crack propagation in Ni_3Al-B. Polished cross sections of Ni_3Al-B, containing cracks after cold rolling and annealing, are analyzed with OIM. The grain boundaries are classified according to their Σ value. Although some grains are separated by a crack, the OIM software can treat the grains as if they were adjacent and determine the Σ value of the cracked grain boundary, although the separation of the boundaries leads to a small rotation. In figure 5.14, an OIM image quality map of Ni_3Al-B after the last thermomechanical cycle is shown. The Σ3 boundaries are indicated by white lines. Although the determined fraction of Σ3 boundaries is rather high (22%), many of them are observed inside grains and are annealing twins instead of grain boundaries. Along the crack, which mainly follows the grain boundaries, the fraction of Σ3 boundaries is lower than in the rest of the material, which confirms earlier results [27,28,34].

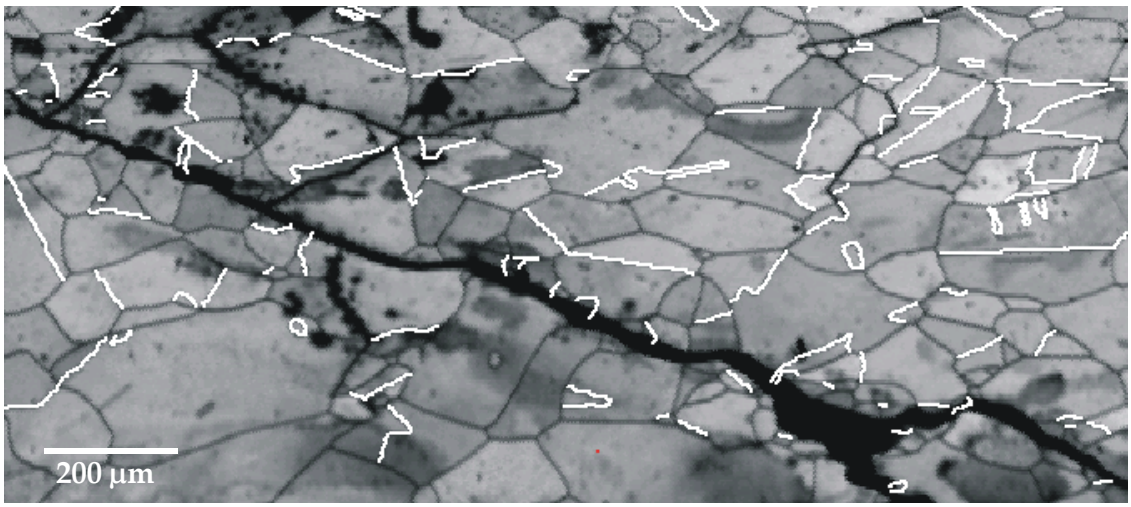

Figure 5.14: *OIM image quality map of cold rolled and recrystallized Ni_3Al-B*

5.5.3 Tensile tests on Ni_3Al-B

In order to obtain quantitative information about the ductility of homemade Ni_3Al-B, which can be compared with earlier results, specimens for tensile tests are manufactured out of the batches of material that showed some ductility during impact fracture (batch 18-21). Before and after tensile deformation, OIM analysis is performed on the same position on the polished surface of the tensile

specimens. In this way, the influence of deformation on the misorientations from grain to grain and inside a particular grain can be studied.

Because of the very small specimen sizes (a cross section of 1.8×0.8 mm^2 and a length of 17 mm), an accurate determination of the elongation is necessary. Therefore, a video-extensometer system is used, consisting of a CCD camera and accompanying image processing software that record the separation of two horizontal bars attached to the vertically placed tensile specimen. The distance between the two bars before any load is applied is referred to as l_0 and is ~ 5 mm. The two crossheads of the Instron 1195 move apart with a speed of 0.05 mm/min and the stress is recorded as a function of the strain ε, the elongation Δl divided by l_0. This leads to a stress-strain curve as is shown in figure 5.15.

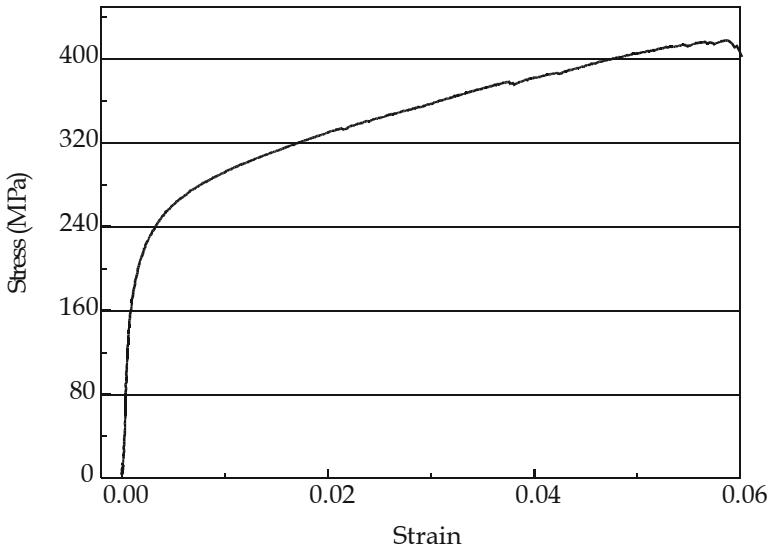

Figure 5.15: *Stress-strain curve of Ni_3Al-0.2 at.% B*

The yield strength of this material is determined by the 0.002 strain offset method, i.e. the stress at the intersection between the curve and a line parallel to the elastic portion, starting at 0.002 strain. The obtained yield strength of this specimen (~233 MPa) is comparable to earlier results on stoichiometric Ni_3Al-0.35 at.% B with a grain size of 100 μm, at room temperature [25]. Some other tensile specimens showed somewhat lower yield strengths (~170 MPa).

Furthermore, it can be seen in figure 5.15 that the elongation reaches 6%. Another specimen is deformed to 8% strain, which is more than any similarly processed undoped Ni_3Al specimen [25], but remains far from ductilities previously obtained on B-doped Ni-rich material [2]. However, the amount of elongation is sufficient to study deformation processes inside the grains. Figure

5.16 shows an OIM image quality map before deformation (left) and an indication of the misorientations inside the grains (right). Inside a grain, the misorientation with respect to the center of the grain is indicated by the brightness. It is clear from figure 5.16 that, except for the single central grain, the misorientations inside the grains are very low before deformation is applied. The direction of deformation is indicated by the arrows in figure 5.16. The white grain boundaries are again Σ3 boundaries.

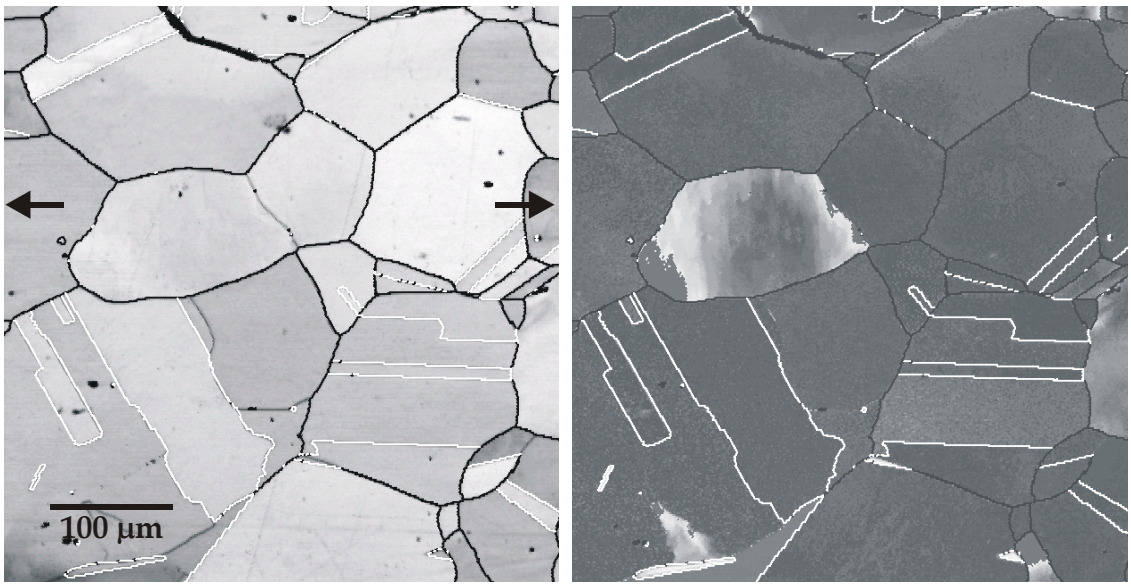

Figure 5.16: *OIM image quality map of undeformed Ni_3Al-B (left) and relative misorientations within the grains (right), with the arrows indicating the direction of deformation*

In figure 5.17, OIM data are acquired on the same part of the surface, after the tensile test shown in figure 5.15. The relative misorientation within the grains, as is depicted by the misorientation profile along the black line in figure 5.17 (left), is larger after deformation than before. Before deformation, the misorientation within that particular grain did not exceed 1°. The surface normal of this grain is approximately parallel to the <112> direction. As in the deformed specimens, the formation of bands seems to occur in several grains, indicative of a higher ductility response on loading.

Similar experiments are performed on a polished cross section of the deformed rod in figure 5.8, because the tensile elongation in the highly deformed part of the rod is much higher than in the tensile tests. Because it is impossible to compare the same region before and after deformation, two regions in the cross section are analyzed: the center of the rod, where deformation is supposed to be minimal, and the tensile deformed part of the rod.

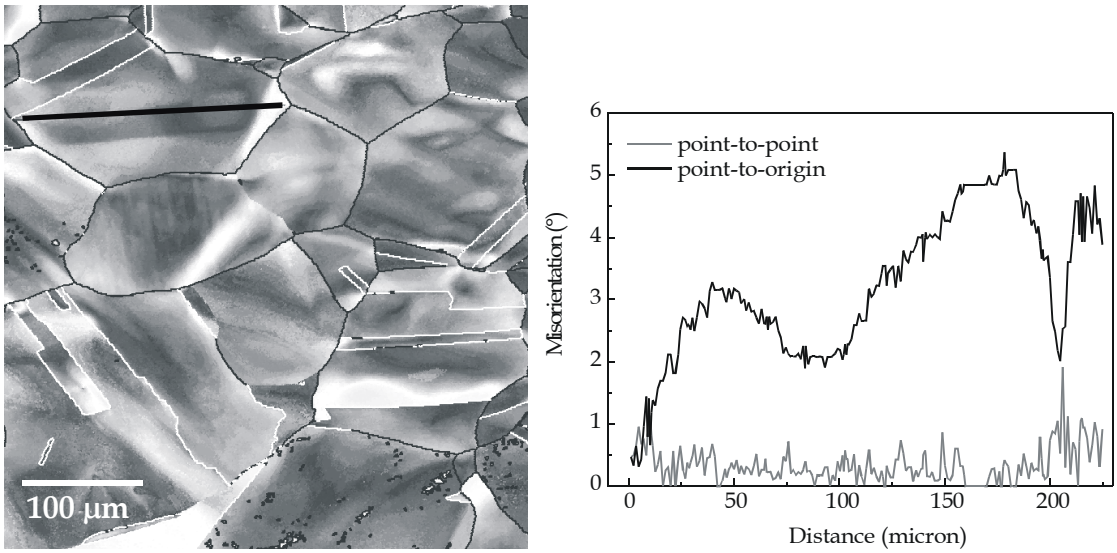

Figure 5.17: *Relative misorientations within the grains after deformation (left) and misorientation profile inside a particular grain (right)*

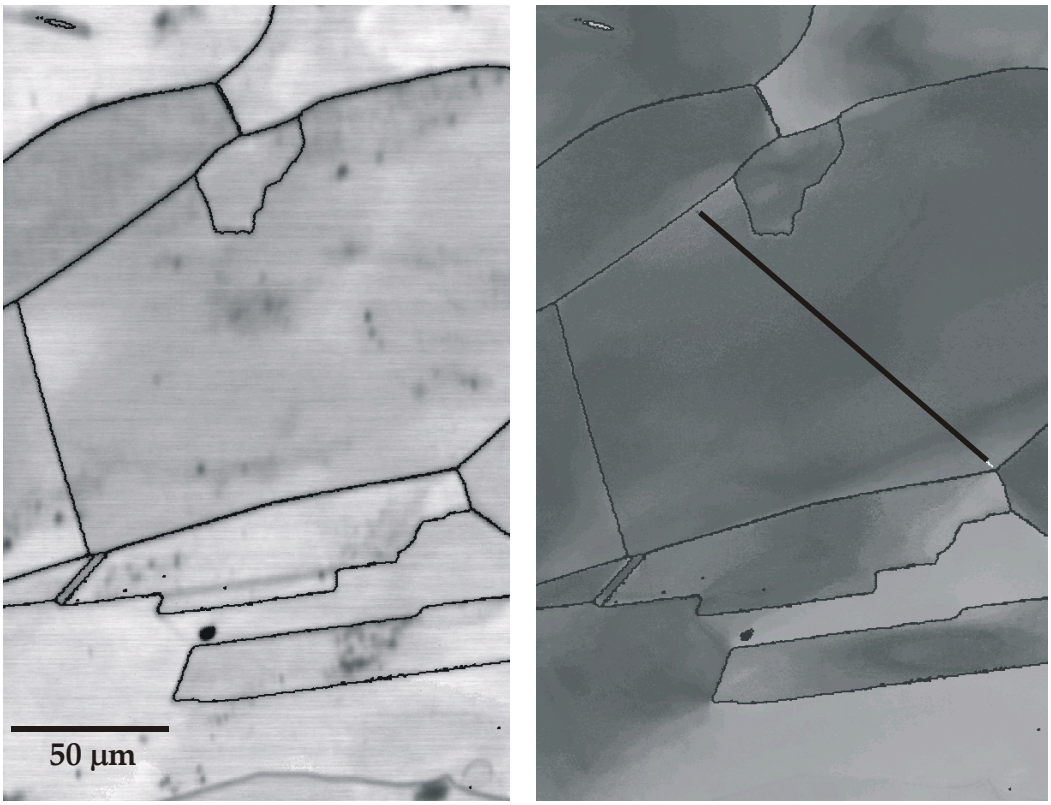

Figure 5.18: *OIM image quality map of the center of the deformed rod (left) and relative misorientations inside the grains (right)*

Figure 5.18 shows an OIM image quality map of the region near the neutral axis of the bent rod (left), together with an image of the relative misorientations within the grains (right). There are no Σ3 boundaries present in this small region. Figure 5.19 shows similar images, obtained from the tensile deformed region of the rod. In figure 5.20, a more quantitative comparison between both regions is given by the combination of the misorientation profiles along the diagonal black lines in the region near the neutral axis (figure 5.20, left) and the deformed region (figure 5.20, right).

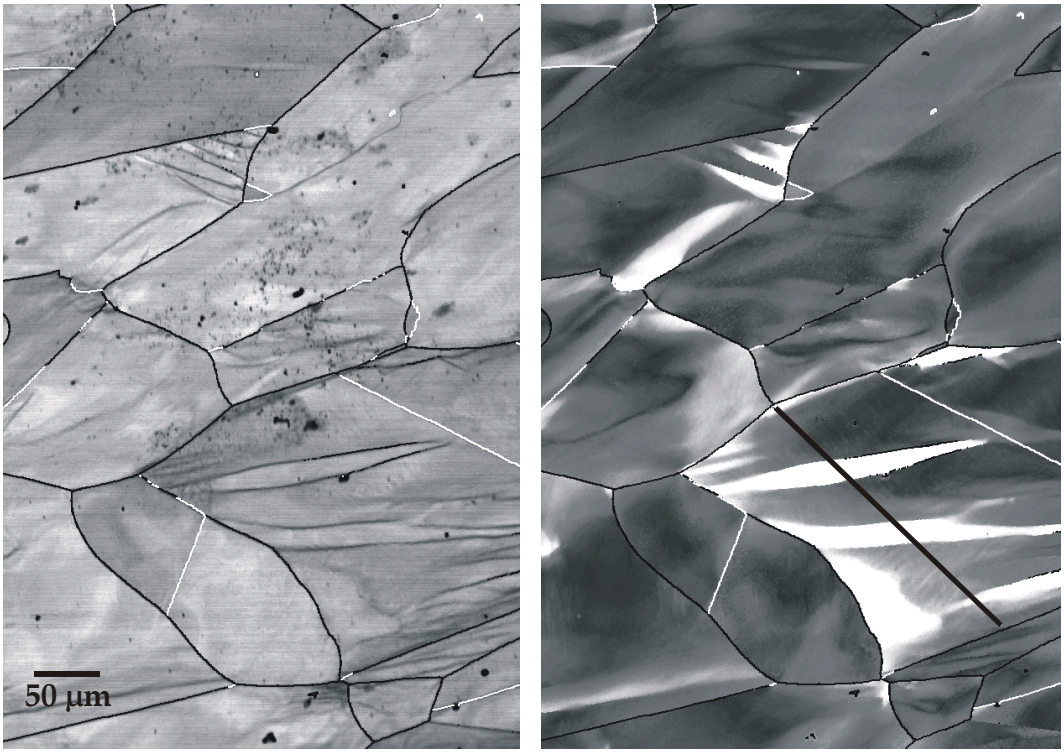

Figure 5.19: *OIM image quality map of the tensile region of the deformed rod (left) and relative misorientations inside the grains (right)*

In figure 5.19, the image quality map clearly indicates strained regions (dark lines within the grains), which is confirmed by the relative misorientations on the right. The misorientation profile of figure 5.20 shows the occurrence of bands with relatively high misorientation within the grain. It is found that the transition from the 'matrix' to the band is a rotation around a <110> axis. Compared to the tensile tests, bands occur more frequently and are more pronounced (i.e. the misorientation is higher), which indicates a higher ductility.

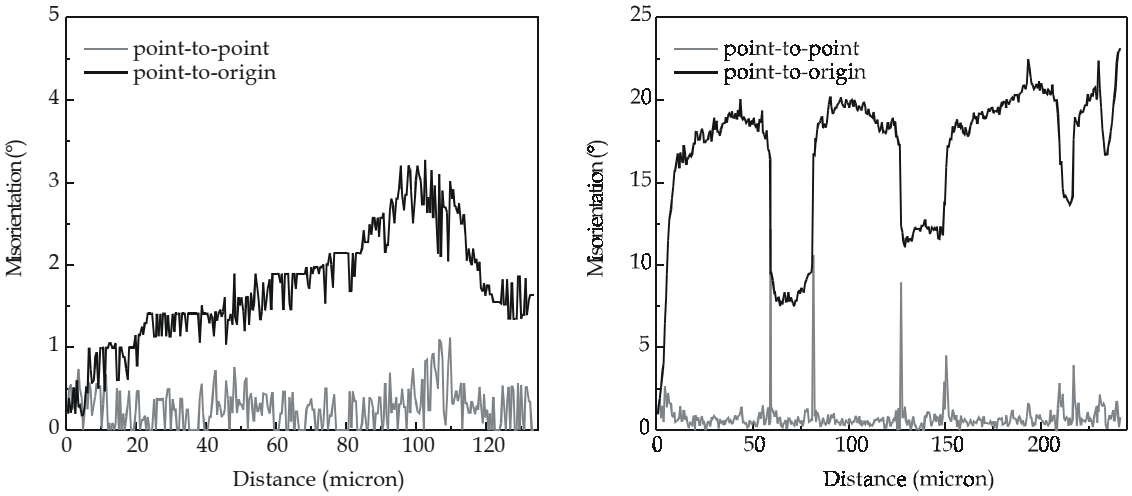

Figure 5.20: *Misorientation profiles inside grains, along the black lines in figure 5.18 (left) and figure 5.19 (right)*

5.5.4 Discussion

The fact that all notched Ni_3Al-B specimens fracture easily and mostly intergranular in the JAMP 7800F means that the grain boundaries remain weak points in these alloys, although they are strengthened by the addition of boron. Earlier results indicated moderate tensile ductilities (~18.5%) for boron doped Ni_3Al specimens that predominantly showed intergranular fracture at RT [2]. This means that the occurrence of intergranular fracture does not necessarily mean that a specimen cannot be deformed plastically at all. The homemade specimens considered in this chapter may be compared with these results, because severe deformation without fracture is observed for specimens without a notch, whereas the notched remainder of the same rod fractures easily and mostly intergranular. Therefore, in contrast to the specimens without a notch, there is no dependence of fracture mode on boron concentration in specimens with a notch.

5.5.4.1 The effects of a notch

To elucidate the effects of the presence of a notch, the stress fields in the vicinity of a notch are examined first. The approach of Williams is followed [48], where a notch with angle β is subjected to symmetrical (mode-I) loading. The notch faces are traction free. A cylindrical coordinate system (r,φ) is introduced where $\varphi = 0$ coincides with the symmetry plane (figure 5.21). Stresses are represented by an Airy stress function, χ. For many purposes the Airy stress functions

provide a convenient way of a solution of a stress field, e.g. of dislocations and cracks in linear elasticity [49]. In absence of body forces, the Airy stress function must be biharmonic, i.e.

$$\nabla^4 \chi = 0 \tag{5.5}$$

Solutions of the form $\chi = r^{S+2} F(\varphi)$ are sought and Williams found, using the condition of traction free notch faces (i.e. σ_φ and $\sigma_{r\varphi}$ are both equal to zero for $\varphi = \pi - \frac{1}{2}\beta$)

$$\chi = C r^{s+2} \left\{ (s+2)\cos(s\varphi)\sin\left[(s+2)\left(\pi - \frac{\beta}{2}\right)\right] - s\cos\left[(s+2)\varphi\right]\sin\left[s\left(\pi - \frac{\beta}{2}\right)\right]\right\} \tag{5.6}$$

Any stress field can be derived from equation (5.6), that is, $\sigma_\varphi = \nabla_r^2 \chi$, etc. The strength of the notch singularity, s, follows from the conditions of traction free notch faces. If β is $\pi/2$, which is approximately the case in our experiments, the strength of singularity of the notch is found to be s = -0.45 and it is almost equal to the strength of a crack singularity in linear fracture mechanics, $\sigma \sim r^{-0.5}$.

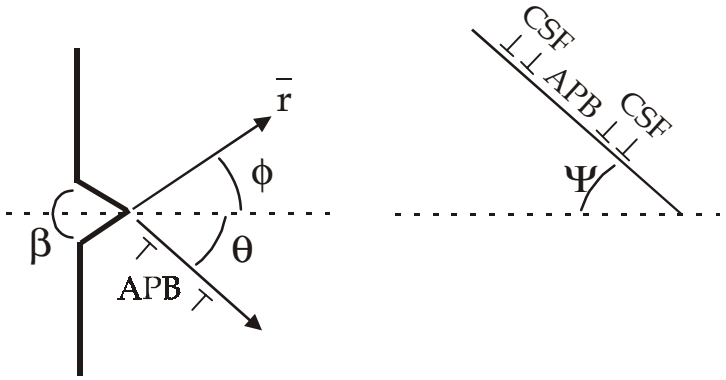

Figure 5.21: *Geometry of the notch with angle β. CSF and APB represent the complex stacking fault and antiphase boundary involved in a superlattice dislocation in Ni_3Al*

In the Charpy test that is executed the material is subjected to a relatively high strain rate. The notch promotes brittle fracture because the strain and strain rate are increased in its vicinity. An increase in strain rate, $\dot{\varepsilon}$, increases the flow stress, although the degree to which it does is strongly a function of temperature and is specific to the material. The nucleation stress for (cleavage) fracture becomes smaller than the yield stress.

The strain rate sensitivity of the flow stress is related to the atomistic / microscopic mechanisms of deformation dealing with dislocations. When both strain hardening and strain rate sensitivity are important, the flow stress may be adequately represented by

$$\sigma_f = k\left(\dot{\varepsilon}\right)^m \left(\varepsilon\right)^n \tag{5.7}$$

where $m \sim 0.1$ for metals at room temperature. As such, the notch effect causes an increase of the stress necessary to induce plastic flow, i.e. above that required in a simple tensile test. As a consequence, the ductile-to-brittle transition temperature is increased and the fracture stress becomes smaller than the yield stress up to higher temperatures. At the lowest temperatures for such a brittle fracture, the plastic zone in front of the notch becomes comparable to the grain size. Fracture is initiated at the notch tip and occurs by repeated fracture along grain boundaries. At higher temperatures, below DBTT, brittle fracture from the notch is considered as a linkage of cracks, initiated at the plastic-elastic zone, over the complete plastic zone in a more or less discontinuous process. Nevertheless, both continuous and discontinuous processes involve some plastic deformation.

The generation of a dislocation at the notch tip in Ni_3Al at low temperature is considered first. For dislocation emission the energy release rate G_{disl} can be estimated from the Rice-Thomson formalism [50], where G_{disl} is expressed in terms of the force necessary to emit dislocations, F_{emit}. The latter has to be at least equal to the image force F_{image}, which pulls the dislocation back to the notch. The image force exerted on a dislocation by a free surface is

$$\left|\vec{F}\right|_{image} = \left(\frac{\mu b^2 \cos^2\alpha}{4\pi\left(1-\nu\right)} + \frac{\mu b^2 \sin^2\alpha}{4\pi} \right)\frac{1}{r} \tag{5.8}$$

where μ is the shear modulus, ν is Poisson's ratio and α is the angle between the Burgers vector $\boldsymbol{b}$ and the normal to the crack tip. The shear stress acting on the slip plane that intersects the notch plane ($\varphi = 0$) under an angle θ (figure 5.21) can be derived from the Airy stress function χ by the expression

$$\sigma_{r\varphi} = -\frac{\partial}{\partial r}\left(\frac{1}{r}\frac{\partial \chi}{\partial \varphi}\right) \tag{5.9}$$

It follows that for a notch with $\beta = ½\,\pi$ the shear stress resembles the stress field of a mode-I crack if the constant in the Airy stress function, C in equation (5.6), is equal to $K/(2\pi)^{-s}$, with K the stress intensity factor of a crack. Then, equation (5.9) can be rewritten as

$$\sigma_{r\varphi} = -\frac{K}{(2\pi r)^{-s}}\,\Sigma_{r\varphi} \tag{5.10}$$

and the emission force can be described as

$$\left|\vec{F}\right|_{emit} = \frac{Kb\cos\alpha}{(2\pi r)^{-s}}\;\Sigma_{r\varphi} \tag{5.11}$$

Equation (5.8) and equation (5.11) are equated and using the relationship between the Griffith-Orowan energy release rate and the stress intensity factor (plane strain)

$$G = \frac{K^2}{E}\left(1-\nu^2\right) \tag{5.12}$$

where E is the Young's modulus, the energy release rate by a dislocation at the notch is given by

$$G_{disl} = \frac{E\,b^2}{16(2\pi r_c)^{2s+2}\left(1-\nu^2\right)}\left[\frac{\cos\alpha + (1-\nu)\sin\alpha\tan\alpha}{\sum_{r\varphi}}\right]^2 \tag{5.13}$$

For a unitary ½ <110> dislocation in Ni_3Al, with μ = 88 MPa and ν = 0.3, G_{disl} is found to be 34.8 J/m^2, i.e. much larger than the energy release rate associated with cleavage fracture, which is about 2 J/m^2. However, in this calculation the critical distance r_c is assumed to be of the order of the Burgers vector of a unitary ½ <110> dislocation, whereas in the $L1_2$ ordered Ni_3Al system a superlattice dislocation consisting of two unitary ½ <110> dislocations separated by an antiphase boundary (APB) should be considered. The two unitary dislocations may be split into two Shockley partial dislocations separated by another planar fault, i.e. a so-called Complex Stacking Fault (CSF). Experimentally [51,52] and theoretically [31-34] the distance between the two

unitary dislocations varies between 2.7 and 4.2 nm. Although the energy release rate of a unitary dislocation is high in comparison with G_{cleav}, G_{disl} for a superlattice dislocation will be considerably lower than G_{disl} for a unitary dislocation. Furthermore, it should be realized that after nucleation of the leading ½ <110> dislocation, the dislocation experiences an energy barrier because of the APB ordering energy. The dislocation gets stuck and will not be emitted under the same applied stress. In fact, F_{emit} will become more negative, which tries to draw the dislocation back into the notch. It should be stressed that the calculation thus far assumes the nucleation of a straight edge dislocation at the notch tip and that the tip lies along the intersection of a slip plane and the fracture plane. A more exact account of the three-dimensional elastic interactions between a nucleated dislocation loop and a crack has been reported in literature [53] and the value of G_{disl} is increased by an estimated factor of 2, depending on φ and α and on the value chosen for the energy of a ledge, E_{ledge}, created at the tip by the emerging dislocation loop.

So far, it can be concluded that plasticity at the notch will not occur to a great extent. However, although $G_{cleav} << G_{disl}$ it does not necessarily mean that cleavage will actually occur because this may be dominated by plastic flow associated with pre-existing, rather than tip nucleated dislocations. The situation described above is appropriate to a quasi-static notch or stationary crack, but changes when the crack/notch is moving and dislocation sources are present inside the grain at a position r. Dislocations may move to the crack plane along the slip plane oriented at an angle ψ to it (see figure 5.21). A conservative estimate of the dislocation velocity, v_D, required to effect crack blunting is: $v_D > v_{crack} / \cos \psi$. Consequently, relaxation of the crack necessitates a highly mobile dislocation density and/or a relatively slowly moving crack. The dislocation velocity is related to the frictional shear stress, τ_0, through

$$v_D \approx \left(\frac{\tau}{\tau_0} \right)^P \tag{5.14}$$

There are two reasons that make v_D in Ni_3Al small compared to e.g. Ni. First, the frictional force in Ni_3Al is much higher. τ_0 can be formulated in terms of a dislocation drag coefficient, depending on the Debye frequency squared, ω_D^2. Because the latter is larger for Ni_3Al than for pure Ni, the dislocation velocity is smaller in Ni_3Al. An even more important aspect is that dislocations in Ni_3Al

experience less cross-slip because of the ordering energies and Kear-Wilsdorf locks on {100} planes, i.e. an increase in τ_0 is expected.

Therefore, we may conclude that a highly mobile dislocation density that can cause crack tip blunting and ductile fracture is not present in Ni_3Al. Only at higher temperatures when the occurrence of cross-slip becomes more likely, τ_0 decreases and v_D increases.

5.5.4.2 The effect of boron on fracture

Whether the material exhibits intergranular fracture can be estimated from the stress of a pile-up of dislocations in a particular grain, τ^*, that is required to activate dislocations in the next grain. The stress concentration from the dislocation pile-up increases with the number of dislocations in the pile-up. The latter increases with the grain-size d [49] and dislocation activation in the next grain occurs when

$$(\tau_a - \tau_0)\sqrt{\frac{d}{4r}} = \tau^* \qquad (5.15)$$

where τ_a is the applied shear stress and τ_0 is the intrinsic, frictional shear stress, resisting dislocation motion inside the grain. Suppose that intergranular fracture occurs along the grain-boundary, i.e. r in equation (5.15) becomes of the order of the interatomic spacing, a_0, and that the effective tensile stress σ^* ($\cong 2\tau^*$) becomes larger than the theoretical strength, σ_{th}. The latter can be described by the decohesion of two atomic planes, on which the atoms are arranged periodically with λ. Hooke's law is assumed for the initial part of the stress-displacement curve, yielding a theoretical strength σ_{th} equal to $\sqrt{E\gamma / a_0}$. Equation (5.15) yields for crack nucleation, with $\gamma \cong Eb/40$

$$\sigma_{nuc} > \sigma_0 + \frac{1}{3}E\sqrt{\frac{b}{d}} \qquad (5.16)$$

Taking the experimental friction stress undoped Ni_3Al equal to 133 MPa [26] and an average grain size of about 100 μm in our samples, we find the stress for crack nucleation at the boundary to be 250 MPa. Whether or not flow initiation is concurrent with fracture depends on the value of σ_0 in comparison with the

fracture stress σ_F. Here, σ_0 is larger than σ_F. Therefore, cracks will nucleate and the microcracks thus formed propagate along the boundary, leading to intergranular fracture. The equations above are valid when there is no slip transmission at the grain boundaries at all and explain why undoped Ni_3Al fractures intergranularly.

Although the detected amount of boron on former grain boundaries of all boron doped specimens immediately after fracture is low compared to 24 hours later and the notched specimens still fracture easily, boron is present at the boundaries and has a beneficial effect on the ductility and formability. Without boron, homemade Ni_3Al specimens could not be cold rolled at all without cracking. With the addition of boron, it is possible to deform specimens by about 10% (reduction in thickness, the Von Mises equivalent strain is 12%) before surface cracks appear.

Specimens without a notch, containing 0.8 at.% boron, do not deform heavily during in-situ fracture attempts, in contrast to specimens with 0.2 at.% boron. Both sorts of specimens show similar relative intensities of boron on the fracture surface, indicating saturation of boron at the grain boundaries. Upon increasing the boron concentration from 0 to 0.2 at.%, the yield stress, which is proportional to σ_0, of the material increases, which would lead to a higher propensity for brittle fracture. Segregation of boron along the boundary will also affect σ_{th} in equation (5.16). The mechanism through which boron alters σ_0 can be related to an increase of the ordering energy. Upon boron doping both the APB energy and the energy of a complex stacking fault (CSF) increase [54] and therefore less cross-slip of the superlattice dislocation onto another {111} will occur. The consequence is that in boron doped specimens cracks will be nucleated with plastic flow at σ_0 but with increasing boron concentration cracks may not propagate until the stress is further increased to σ_F, i.e. the failure process becomes propagation controlled rather than crack nucleation controlled.

There has been quite a debate in literature that boron contributes to ductilization because the cohesive energy and σ_{th} increase along the grain-boundaries in Ni_3Al due to directional Ni-B bonds. However, in these systems with directional bonds a distinction should be made between bonds perpendicular and parallel to the applied stress. For purely metallic bonds less work of fracture is necessary for shearing the bond than for stretching it. Electronic charge will flow from the bond parallel to the stress to the bond

perpendicular to the applied stress and the fracture type will become ductile. In the case of highly localized bonds, the situation is different: the potential representing energy-displacements perpendicular to the bond axis will become steeper than the potential referring to displacement along the bond axis. The same observations can be made in molecular solids where the vibration of a stretch type motion has a lower frequency than the shear type vibration. A higher vibrational frequency is equivalent to a steeper, narrower potential well. This results in less force and work to break by stretching than by shearing. The consequence is that directional bonds, like Ni-B, will promote brittle fracture rather than ductile failure. Therefore, explanations of ductilization based on an increase in the cohesive strength due to the formation of Ni-B bonds are not supported. Actually, the effect of boron on the failure mechanism works only indirectly by increasing the Ni concentration along the grain boundary and not directly on the bond strength. Through the presence of boron at the grain boundaries slip transmission becomes feasible because the mean boundary plane becomes Ni-enriched. Also the energy associated with the formation of a crack tip ledge left by an emerging dislocation, E_{ledge} (see equation (5.13)) into the next grain will be decreased because of the Ni-enrichment and it will serve to ease the dislocation nucleation threshold. An increase of the boron concentration from 0.2 to 0.8 at.% does not lead to more slip transmission, because the amount of boron (and therefore its effect) at the grain boundaries is not observed to change. However, it does affect the yield stress, leading to a higher propensity towards brittle fracture. Evidence for increased slip transmission stems from the fact that Ni_3Al-0.8 at.% B specimens exhibit transgranular fracture, whereas the undoped specimens only show intergranular fracture.

The effect of boron depends on the grain size [55]. The homemade specimens consist, after the thermomechanical treatments, of grains with an average size of ~100 μm, which is fairly large compared to earlier studies [2,5]. Liu et al. [2] did not observe large differences in ductility between specimens containing 0.2 and 0.8 at.% boron. However, the average grain size was ~25 μm. For larger grain sizes, the effect of boron in the lattice overcomes the effect at the grain boundaries. On top of this, the grain boundary effect saturates when the boron amount at the grain boundary is at its maximum, whereas adding more boron still leads to an increase in yield stress. This explains the difference in ductility upon varying the boron content, for larger grain sizes. Grain refinement will decrease the sensitivity of the fracture behavior with respect to the amount of boron.

The Σ3 grain boundaries have a high resistance towards intergranular fracture. From a theoretical point of view this can be understood by realizing that resolved shear stresses act to a same extent on the slip planes on either side of a symmetrical Σ3 boundary. In addition, a leading ½ <110> superpartial can be fully absorbed in the Σ3 by dissociating in two grain boundary Shockley partials and a superlattice dislocation can be completely transmitted at higher shear stresses [31,32]. Therefore, intergranular fracture will not occur. This is also visible from the OIM results in figure 5.14. However, specimens with extremely high fractions of these low energy boundaries can only be manufactured through processes such as unidirectional growth through zone melting [24]. Cold rolling and annealing at 1000° C of these specimens was observed to lead to a decrease in the fraction of Σ3 grain boundaries from 0.29 to 0.14 [24]. The homemade specimens have to be cold rolled and annealed to remove the original solidification structure that remains after arc-melting. Therefore, the amount of 'strong' boundaries will not reach the values necessary for ductilization of the material. Furthermore, the indicated amount of Σ3 boundaries by OIM is obscured by the large amount of annealing twins present after several thermomechanical cycles.

The tensile tests on Ni_3Al-0.2 at.% B do not show the high ductilities that are expected when figure 5.9 is regarded. The maximum tensile elongation that is attained during the tensile tests is ~ 8%, which is higher than that for similarly processed undoped material [25], but much lower than the reported ~ 50% for Ni_3Al-B [2]. However, due to size limitations in the manufacturing process and the number of cold rolling treatments the tensile specimens are very small and delicate. Furthermore, because the specimens are intended for OIM analysis before and after the tensile experiments, the specimen surface has to be polished. This leads to extra preparation steps due to which the vulnerable specimens can already contain cracks before the tensile tests. This is also reflected by the different yield strengths that are obtained for some specimens. The initial presence of internal defects, caused by cold rolling or other steps of the specimen preparation, leads to scatter in the obtained values for yield strength and ductility and, in general, to a lower ductility. However, the large deformation of the Ni_3Al-0.2 at.% B rods without a notch, as shown in figure 5.9, indicates that the homemade material can be deformed to a large extent, under ideal circumstances. Estimations of the elongation in the tensile region of the rod in figure 5.9 yield a value of at least 20%.

The image quality obtained by OIM can provide an indication of present residual strain, because it gives information about the regularity of the lattice in the diffraction volume. Therefore, grain boundaries and strained regions appear darker in an image quality map. The only dark regions in the left side of figure 5.16 are the grain boundaries, which are easily recognized by the OIM software, and some pits that are present on the specimen surface. Before deformation, no strained regions occur inside grains. After tensile deformation, the situation is different. The grains itself may have a tendency to rotate or deform as a whole, which is complicated due to the constraints imposed by the surrounding grains. Therefore, the grains deform internally, which becomes clear from the maps of relative misorientations within grains.

Deformation of Ni_3Al-B is accompanied by the formation of bands with a relatively high misorientation, as is visible after tensile tests as well as after cold rolling. The high amount of annealing twins after several thermomechanical cycles leads to the assumption that these bands may evolve into annealing twins upon subsequent heating. Furthermore, the maps of relative misorientations after tensile deformation indicate an increase in misorientation close to the grain boundaries. These are the regions where the constraint of neighboring grains is the highest, especially near triple junctions.

Clearly, there is some interaction between two adjacent grains at a grain boundary, whereas this is not the case for undoped Ni_3Al. Although no tensile tests are performed on undoped material, this is concluded from the fact that it is impossible to deform Ni_3Al by cold rolling without immediate intergranular fracture. Upon the slightest deformation the grains are immediately separated.

The results obtained by OIM point in the direction of an increase in slip transmission at the grain boundaries by the addition of boron, as do the obtained results on the influence of the amount of boron. Adjacent grains can interact with each other, whereas they cannot in undoped Ni_3Al. Chemical disorder at the grain boundary, caused by Ni and boron interaction, which is indicated by the results of section 5.4, facilitates dislocation transmission, as discussed in 5.2.4. Both Ni-rich undoped Ni_3Al and boron doped stoichiometric Ni_3Al possess a higher ductility than the stoichiometric material without boron, but the fracture is mostly intergranular. This means that Ni-enrichment by itself is not sufficient to fully ductilize Ni_3Al and induce transgranular fracture. Ni-enrichment at the grain boundaries is present without boron [12], but the extent may be less than in boron doped Ni-rich material. The addition of boron to

slightly Ni-rich (75.2 % Ni) leads to a moderate ductility (18.5 % [2]). The addition of boron to Ni-rich material leads to the best possible ductilities, through the presence of both B- and Ni-enrichment at the boundaries, causing an increase in dislocation transmission.

5.6 CONCLUSIONS

In this chapter, it has been shown that after in situ fracture of Ni_3Al-B, boron is present at the surfaces that formerly were grain boundaries in the case of intergranular fracture. The boron intensity increases within 24 hours after fracture due to surface segregation at room temperature, under the influence of the present chemisorbed oxygen and Ni-enrichment at the surface. Sulfur segregates at high temperatures to internal (oxygen free) surfaces such as pores. The presence of sulfur at a surface hampers surface oxidation and thereby boron surface segregation. At room temperature, boron surface segregation occurs while sulfur segregation is not observed. Boron, interstitially present in the Ni_3Al matrix, has the ability to segregate to a free surface at room temperature. Furthermore, an important driving force for boron surface segregation, i.e. the interaction with oxygen, is not valid for sulfur surface segregation.

The presence of a notch induces brittle fracture due to an increase in strain and strain rate in its vicinity and, as a consequence, an increase in brittle-to-ductile transition temperature. The fracture stress is smaller than the yield stress up to higher temperatures. Because of the high ordering tendency in Ni_3Al, plasticity at the notch will not occur to a great extent and a highly mobile dislocation density, necessary for crack tip blunting, is not present.

Without a notch, the amount of boron is shown to have a marked influence on the fracture behavior of Ni-rich material. Specimens containing 0.8 at.% boron fractured in situ, whereas Ni_3Al-0.2 at.% B heavily deformed during in situ fracture attempts. Undoped specimens fractured intergranularly and did not show any ductility. Upon increasing the boron concentration from 0 to 0.2 at.%, slip transmission at the grain boundaries largely overcomes the increase in yield stress due to boron addition. When the amount of boron increases to 0.8 at.%, slip transmission at the boundaries does not change, because similar relative boron intensities are measured. It does lead to an increase in yield stress, increasing the propensity for brittle fracture. Grain refinement would

decrease the sensitivity of the fracture behavior with respect to the amount of boron.

The Σ3 grain boundaries have a high resistance toward intergranular fracture, as becomes clear from the OIM results on cold rolled and annealed material. However, specimens with fractions of Σ3 grain boundaries that are high enough to ductilize Ni_3Al cannot be manufactured by arc-melting and subsequent thermomechanical cycles, as is used for the homemade specimens. Due to mechanical damage induced by several preparation steps, the measured tensile ductilities of Ni_3Al-0.2 at.% B are low compared to earlier results, although they are higher than for undoped material. The presence of cracks before tensile testing leads to a scatter in the obtained yield strengths as well.

The comparison of OIM measurements before and after tensile deformation of doped specimens yields information on strained regions that are the result of deformation and the relative misorientations within grains. It becomes clear that the relative misorientation increases close to the grain boundaries and especially near the triple junctions, because these are the regions where the constraints imposed by the surrounding grains are maximal. This does mean that there is some interaction at the grain boundaries to accommodate to the applied deformation. In undoped material, however, there is no interaction at all at the grain boundaries, because it immediately fractures along the grain boundaries upon the slightest deformation. When there is no slip transmission at the grain boundaries at all, as in undoped Ni_3Al, it can be calculated that fracture will be intergranular.

The results obtained by OIM and the influence of the amount of boron point in the direction of an increase in slip activity near the grain boundaries by the addition of boron. Chemical disorder at the grain boundary is caused by Ni and boron interaction. Although boron causes an increase of the grain boundary cohesive energies, the formation of directional electronic Ni-B bonds does not contribute to enhanced ductility. On the contrary, addition of boron to Ni-rich material leads to ductilization through the accompanying Ni-enrichment at the boundaries, causing enhanced dislocation transfer.

REFERENCES

1. N.S. Stoloff, C.T. Liu in Physical Metallurgy and processing of Intermetallic Compounds (Eds. N.S. Stoloff, V.K. Sikka) Chapman & Hall, NY (1996)
2. C.T. Liu, C.L. White, J.A. Horton, Acta Metall. **33** (1985) 213
3. R.G. Davies, N.S. Stoloff, Trans. Metall. Soc. AIME **233** (1965) 714
4. T. Takasugi, E.P. George, D.P. Pope, O. Izumi, Scripta Metall. **19** (1985) 551
5. E.P. George, C.T. Liu, H. Lin, D.P. Pope, Mat. Sci. Eng. A **192-193** (1995) 277
6. K. Aoki, O. Izumi, Nippon Kinzoku Gakkaishi, **43** (1979) 1190
7. C. L. White, A. Choudhury, Mat. Res. Soc. Symp. Proc. **81** (1987) 427
8. S. Hofmann, M. G. Stepanova, Appl. Surf. Sci **90** (1995) 227
9. D. Tomanek, S. Mukherjee, V. Kumar, K.H. Bennemann, Surf. Sci. **114** (1982) 11
10. J.J. Kruisman, V.Vitek, J.Th.M. De Hosson, Acta Met. **36** (1988) 2729
11. S.P. Chen, A.F. Voter, D.J. Srolovitz, Scripta Metall. **20** (1986) 1389
12. S. Subramanian, D.A. Muller, J. Silcox, S.L. Sass, Mat. Sci. Eng. A **239-240** (1997) 297
13. D.A. Muller, S. Subramanian, P.E. Batson, J. Silcox, S.L. Sass, Acta Mater. **44** (1996) 1637
14. S.P. Chen, A.F. Voter, R.C. Albers, A.M. Boring, P.J. Hay, J. Mater. Res. **5** (1990) 955
15. O. Izumi, T. Takasugi, J. Mater. Res. **3** (1988) 426
16. A.I. Taub, C.L. Briant, Acta Metall. **35** (1987) 1597
17. W. Losch, Acta Metall. **27** (1979) 1885
18. R.P. Messmer, C.L. Briant, Acta Metall. **30** (1982) 457
19. L. Goodwin, R.J. Neds, V. Heine, Phys. Rev. Lett. **60** (1988) 2050
20. J.E. Hack, D.J. Srolovitz, S.P. Chen, Scripta Metall. **20** (1986) 1699
21. V. Vitek, S.P. Chen, Scripta Metall. **25** (1991) 1237
22. V. Vitek, S.P. Chen, A.F. Voter, J.J. Kruisman, J.Th.M. De Hosson, Mat. Sci. Forum **49** (1989) 237
23. I. Baker, E.M. Schulson, J.R. Michael, Phil. Mag. B **3** (1988) 57
24. T. Watanabe, S. Tsurekawa, Acta Mater. **47** (1999) 4171
25. T.P. Weihs, V. Zinoviev, D.V. Viens, E.M. Schulson, Acta Metall. **35** (1987) 1109
26. E.M. Schulson, T.P. Weihs, D.V. Viens, I. Baker, Acta Metall. **33** (1985) 1587
27. S. Hanada, S. Watanabe, O. Izumi, J. Mater. Sci. **21** (1986) 203
28. H. Lin, D.P. Pope, Acta Metall. **41** (1993) 553
29. T. Watanabe, T. Hirano, T. Ochiai, H. Oikawa, Mat. Sci. Forum **157-162** (1994)1103
30. C.T. Liu, Mater. Res. Soc. Symp. Proc. **122** (1988) 429
31. J.Th.M. De Hosson, Transmission Electron Microscopy of metals and alloys Handbook of Microscopy (editors: S. Amelinckx, D. van Dyck, J. van Landuyt, G. van Tendeloo), volume 3, p.5-111., VCH, N.Y. (1997)

32. B.J. Pestman, J.Th.M. De Hosson, V. Vitek, F.W. Schapink, Phil. Mag. A **64** (1991) 951
33. B.J. Pestman, J.Th.M. De Hosson, Acta Metall. **40** (1992) 2511
34. J.Th.M. De Hosson, B.J. Pestman, Mat. Sci. Eng. A **164** (1993) 415
35. C. Escher, G. Gottstein, Acta Mater. **46** (1998) 525
36. S.P. Chen, A.F. Voter, R.C. Albers, A.M. Boring, P.J. Hay, Scripta Metall. **23** (1989) 217
37. S.A. Koch, D.T.L. van Agterveld, G. Palasantzas, J.Th.M. De Hosson, Surf. Sci. **476** (2001) L267
38. D.T.L. van Agterveld, G. Palasantzas, J.Th.M. De Hosson, Acta Mater. **48** (2000) 1995
39. S.G. Addepalli, N.P. Magtoto, J.A. Kelber, Surf. Sci. **458** (2000) 123
40. S. Tanuma, C.J. Powell, D.R. Penn, Surf. Interface Anal. **11** (1988) 577
41. St. Frank, U. Södervall, C. Herzig, Intermetallics **5** (1997) 221
42. P. Wynblatt, R.C. Ku in Interfacial Segregation (Eds. W.C. Johnson and J.M Blakely), p.115, American Society for Metals, Metals Park, OH (1979)
43. J.A. Kerr, A.F. Trotman-Dickenson in Handbook of Chemistry and Physics, 52nd edition, 1971-1972
44. S. Subramanian, D.A. Muller, J. Silcox, S.L. Sass, Acta Mater. **44** (1996) 1647
45. U. Otterbein, S. Hofmann, Surf. Interface Anal. **24** (1996) 203
46. F. Labohm, A. van Veen, W.M. Arnoldbik, J. Vac. Sci. Technol. A **17** (1999) 198
47. R.G. Downing, K. Unlu, Trans. Amer. Nuc. Soc. **80** (1999) 110
48. M.L. Williams, J. Appl. Mech. **19** (1952) 526
49. J.P. Hirth, J. Lothe, Theory of Dislocations, McGraw-Hill, NY (1968)
50. J.R. Rice, R. Thomson, Phil. Mag. **29** (1973) 73
51. A.J. Huis in 't Veld, G. Boom, P.M. Bronsveld, J.Th.M. De Hosson, Scripta Metall. **19** (1985) 1123
52. J. Douin, P. Veyssière, P. Bauchamp, Phil. Mag. **A54** (1986) 375
53. P.M. Anderson, J.R. Rice, Scripta Met., **20** (1986)1467.
54. K.J. Hemker, M.J. Mills, Phil. Mag. **A68** (1993) 305
55. C.S. Lee, G.W. Han, R.E. Smallman, D. Feng, J.K.L. Lai, Acta Mater. **47** (1999) 1823

SUMMARY

This thesis describes a study of segregation to interfaces in polycrystalline materials, which may have both beneficial and detrimental effects on the mechanical performance. The importance of segregation to interfaces is determined primarily by the inherent inhomogeneity of interfaces, i.e. the fact that physical and chemical properties may change dramatically at or near the interface itself. The accumulation of impurity atoms at grain boundaries and surfaces leads to the formation of a very narrow zone, of the order of a few lattice spacings, with different chemical composition. As a result of sharp concentration gradients an isotropic bulk solid may change locally into a highly anisotropic medium. Very small bulk concentrations of impurity atoms can lead to significant amounts of those atoms at the grain boundary. This can drastically change the response of a material on loading and can eventually lead to brittle failure of an otherwise ductile material.

Although embrittlement by impurity segregation is frequently observed, grain boundary segregation can also have a ductilizing effect on brittle materials, depending on both impurity and matrix elements. The processes at the grain boundary have to be understood in order to tailor materials with a desirable set of physical and chemical properties for structural applications.

The objective of the research described in this thesis is to correctly correlate macroscopic changes of materials to the influences of segregating elements. The influences of impurity segregation on the materials properties are studied in alloys containing a relatively low number of elements, which minimizes obscuring effects such as the interaction between segregating impurities. In situ intergranular fracture in a dedicated UHV scanning electron – scanning Auger microscope (UHV SEM-SAM) enables the study of grain boundary segregation and its dependence on heat treatments and bulk composition. A direct comparison between grain boundary and surface segregation is made, because embrittling impurities have a higher tendency for surface segregation than for grain boundary segregation, whereas the behavior of ductilizing impurities is thought to be opposite.

Furthermore, the UHV SEM-SAM itself can influence the segregation process of several species. Surface oxidation leads to surface segregation of elements with

high oxygen affinities and prolonged exposure of a specimen to an electron beam leads to enhanced surface oxidation. Knowledge of the influence of an electron beam on the processes at a surface is indispensable when interpreting the acquired segregation data.

Electron beam enhanced oxidation

Prolonged exposure of a clean fracture surface to an electron beam leads to enhanced oxidation, compared to the non-exposed areas on which only oxygen chemisorption takes place. The phenomenon of electron beam enhanced oxidation is encountered during boron segregation studies in Ni_3Al and is found to obscure the observation of surface segregation as a function of time. Nevertheless, it enables a study of the kinetics of oxidation at room temperature in an UHV atmosphere where residual gases cause surface oxidation.

The oxidation kinetics of pure Ni, Ni_3Al, Ni_3Al-B and Ni(B) under the influence of an electron beam can be adequately described by a model assuming the creation of extra oxidation nucleation sites by the electron beam. Different electron fluxes are used to validate the model. At lower fluxes, surface oxidation slows down and the chemisorption regime can be distinguished. At higher fluxes no faster oxidation is observed. Here, the electron flux and therefore the created number of nucleation sites is relatively so large that the amount of oxygen present in the vacuum chamber becomes the rate limiting factor that determines the oxidation kinetics

Upon decreasing the electron flux below a certain level, the kinetics of boron surface segregation can be studied without too much of a distortion from the electron beam enhanced oxidation. Therefore, the influences of the electron beam are of great importance during attempts to monitor processes at a surface.

Embrittling segregants in copper

Grain boundary segregation of impurity elements in copper, such as bismuth or antimony, leads to embrittlement of the bulk material. Segregation studies are performed on Cu-Sb systems, containing sulfur as an impurity, which causes embrittlement as well. The driving force for segregation of antimony is mainly due to its size effect. The segregation of sulfur occurs through a very fast diffusion of sulfur-vacancy complexes and Cu_2S formation at defects. The

influence of the presence of sulfur impurities on the segregation behavior of antimony, to grain boundaries and surfaces, is investigated.

At grain boundaries in Cu-Sb, there is no site competition between Sb and sulfur. In pits, which are actually internal surfaces formed during processing, site competition between S and Sb is observed. The pits show facets and step terrace structures with shapes and symmetry that resemble the *fcc* structure of the copper matrix. Sulfur is found to segregate preferentially to high index surfaces. The crystallographic orientations of the surfaces within the pits are determined by a combination of scanning Auger microscopy, atomic force microscopy and crystallographic arguments based on shape and symmetry of the surfaces. AFM height images can be used to obtain the angles between facets by converting the height derivatives into a histogram.

Similar experiments were performed with Bi, which is even larger than Sb, in Cu. The addition of 1 at.% Bi to Cu leads to precipitation of Bi. At fracture surfaces of Cu-1 at.% Bi, the amount of Bi precipitates that is observed is higher than the amount of pits in Cu-Sb, but of the same order of magnitude. From this, it is concluded that precipitation of Bi in voids leads to the formation of weak spots, promoting fracture and that not all pits in the Cu-Sb specimens are filled with Cu_2S precipitates along the fracture path.

Finally, the quantification of the amount of Sb in grain boundary segregation studies is hampered by the inhomogeneity of the region of analysis. However, segregation studies on similarly inclined planes show that the amount of Sb at the grain boundary increases with increasing bulk content and with decreasing heating temperature. Heating at 250° C leads to both broadening of the profile and a decrease in $I_{Sb}(0)$ with increasing heating time.

Boron segregation in Ni_3Al

The strongly ordered aluminide Ni_3Al has attractive properties for structural applications. The flow stress of single crystalline material increases with increasing temperature and at high temperatures an oxide layer is formed that protects against corrosion. However, polycrystalline Ni_3Al is extremely brittle at room temperature. The addition of boron, which segregates to the grain boundaries, circumvents this problem. The detailed mechanism of the segregation induced ductilization remains still unknown. Auger electron

spectroscopy observations of segregated boron are combined with orientation imaging microscopy to study processes at the grain boundaries.

After in situ intergranular fracture of Ni_3Al-B, boron is present at the surfaces. The boron intensity increases within 24 hours after fracture due to surface segregation at room temperature, under the influence of the present chemisorbed oxygen and Ni-enrichment at the surface. Sulfur segregates at high temperatures to internal surfaces such as pores. The presence of sulfur at a surface hampers surface oxidation and thereby boron surface segregation.

All notched specimens fracture easily, due to an increase in strain and strain rate in its vicinity and, as a consequence, an increase in brittle-to-ductile transition temperature. The fracture stress is smaller than the yield stress and failure is crack nucleation controlled at lower temperatures. The amount of boron is shown to have a marked influence on the fracture behavior of material without a notch because of several reasons. First, its influence is attributed to an increase of the frictional stress and yield stress because the ordering energy increases with increasing boron concentration. Therefore, the coupling strength increases between the partials of the superlattice dislocations in the interior of the grains and consequently the yield stress increases. Secondly, boron segregates to the grain boundaries and increases the fracture stress locally. With increasing boron concentration the failure process becomes propagation controlled rather than crack nucleation controlled. Thirdly, ductilization is not due to the formation of Ni-B bonds because directional bonds will result in less work to break by stretching than by shearing, i.e. Ni-B will promote brittle fracture rather than ductile failure. The effect of boron on the failure mechanism works indirectly by increasing the Ni concentration along grain boundaries and not directly on the bond strength affecting the cohesive strength. Through the presence of boron at the grain boundaries slip transmission becomes feasible because the mean boundary planes become Ni-enriched. Also the energy associated with the formation of a crack tip ledge left by an emerging dislocation into the next grain will be decreased because of the Ni-enrichment and this will serve to ease the dislocation nucleation threshold. Beyond a certain bulk concentration, the amount of boron at the boundaries no longer increases and consequently the slip transmission at the grain boundaries does not increase. An increase in yield stress due to boron addition then leads to a higher propensity towards intergranular fracture.

The Σ3 grain boundaries have a high resistance toward intergranular fracture, as becomes clear from the orientation imaging microscopy (OIM) results on cold rolled and annealed material. The OIM results show that the misorientation increases close to the grain boundaries and especially near the triple junctions, because these are the regions where the constraints imposed by the surrounding grains are maximal. This does mean that there is some interaction at the grain boundaries to accommodate to the applied deformation. In undoped material, however, there is no interaction at all at the grain boundaries, because it immediately fractures along the grain boundaries upon the slightest deformation. Both the results obtained by OIM and the influence of the grain size point in the direction of an increase in slip activity at the grain boundaries by the addition of boron.

In conclusion, besides lattice mismatch, bulk concentration and thermal treatments, several other factors can influence interface segregation. Competition with other elements (S and Sb in Cu), the presence of oxygen at a surface (Mg in Al_3Mg_2, B in Ni_3Al) and electronic effects (B to Ni-rich interfaces) are investigated and observed to markedly affect segregation. Furthermore, the instrument that is used to study segregation may induce, reduce, or obscure the observation of segregation, which impels special caution during segregation studies.

SAMENVATTING

Dit proefschrift beschrijft onderzoek aan segregatie naar grensvlakken in polykristallijn materiaal, wat zowel een gunstig als schadelijk effect op de materiaaleigenschappen kan hebben. De opeenhoping van segregerende atomen aan korrelgrenzen en oppervlakken leidt tot de vorming van een zeer smal gebied met een andere chemische samenstelling dan de rest van het materiaal. Kleine hoeveelheden in de bulk kunnen leiden tot grote concentraties aan een grensvlak, wat een grote invloed heeft op de grensvlakenergie. Dit kan leiden tot drastische veranderingen in de mechanische eigenschappen van een materiaal, bijvoorbeeld tot brosse breuk van normaal gesproken plastisch vervormbare materialen.

Hoewel verbrossing door segregatie het meest voorkomt, kan korrelgrens-segregatie ook een gunstig effect hebben. Een goed begrip van de processen die plaatsvinden aan de korrelgrenzen is nodig om de composities van legeringen aan te passen om zo een gunstig effect te bewerkstelligen en de legeringen te kunnen gebruiken voor structurele toepassingen.

Het doel van het onderzoek is het op de juiste wijze correleren van materiaaleigenschappen aan de invloeden van toegevoegde onzuiverheden. Hiertoe worden de invloeden van segregatie op de materiaaleigenschappen in legeringen met relatief weinig componenten bestudeerd, om zo de interacties tussen de segregerende elementen te minimaliseren. Het in situ intergranulair breken van materiaal in de gecombineerde elektronen- en Auger-microscoop maakt het bestuderen van korrelgrens-segregatie mogelijk. Daarna valt ook oppervlaktesegregatie te onderzoeken en kan een vergelijking worden gemaakt. Verbrossende elementen vertonen namelijk meer oppervlaktesegregatie dan korrelgrens-segregatie en het omgekeerde geldt voor de gunstige elementen.

De Auger microscoop heeft een directe invloed op de segregatie van elementen. Oxidatie leidt tot segregatie van elementen met een hoge affiniteit voor zuurstof en oxidatie wordt versterkt door de elektronenbundel. Kennis van deze invloeden is noodzakelijk om segregatiegegevens op een juiste wijze te interpreteren.

Versterkte oxidatie door de elektronenbundel

Wanneer een schoon oppervlak voor lange tijd wordt blootgesteld aan een elektronenbundel leidt dit lokaal tot een sterkere oxidatie. Dit verschijnsel is opgemerkt tijdens studies naar oppervlaktesegregatie van het element boor in Ni_3Al en blijkt het waarnemen van segregatie versus tijd te bemoeilijken. Het is echter wel mogelijk de ontwikkeling van de hoeveelheid zuurstof te bestuderen, in een ultra hoog vacuüm omgeving waar restgassen de oxidatie moeten verzorgen.

De ontwikkeling van de oxidatie van Ni, Ni_3Al, Ni_3Al-B en Ni(B) onder de invloed van een elektronenbundel blijkt adequaat beschreven te worden door een model dat er van uitgaat dat de elektronenbundel extra mogelijkheden tot oxidatie creëert. Het model is getest door de elektronenflux te variëren. Wanneer de flux lager wordt oxideert het oppervlak minder snel, maar wanneer de flux toeneemt komt er een punt waarop de oxidatie niet meer sneller gaat. Dan is de flux niet langer de bepalende factor in de oxidatie, maar de hoeveelheid restgassen in de vacuümkamer.

Wanneer de elektronenflux genoeg afneemt wordt het mogelijk de ontwikkeling van de hoeveelheid boor op een Ni_3Al oppervlak waar te nemen voordat het oppervlak te ver geoxideerd is. Bij de bestudering van processen aan oppervlakken moet dus terdege rekening worden gehouden met de invloeden van de elektronen bundel.

Verbrossende elementen in koper

Korrelgrens-segregatie van grote elementen als bismut en antimoon leidt tot verbrossing van plastisch vervormbaar koper. Cu-Sb legeringen die ook kleine hoeveelheden zwavel bevatten worden gebruikt om de invloed van de aanwezigheid van zwavel op zowel korrelgrens- als oppervlaktesegregatie van antimoon te bepalen.

Aan korrelgrenzen in Cu-Sb,S is voornamelijk antimoon en derhalve geen competitie tussen antimoon en zwavel waargenomen. In gaten, die interne oppervlakken zijn gedurende de fabricage, komt echter wel competitie voor. De gaten bestaan uit facetten en terrasstructuren waarvan de vormen en onderlinge symmetrie duiden op de *fcc* structuur van het koper. Het is gebleken dat zwavel bij voorkeur naar hoge index vlakken segregeert. De

kristallografische oriëntaties van de vlakken in de gaten zijn bepaald door een combinatie van Auger microscopie, atomaire kracht microscopie (AFM) en het gebruiken van de vormen en symmetrie van de facetten. AFM hoogtebeelden kunnen worden omgezet naar een histogram van hoogte-afgeleiden waaruit de hoeken tussen de facetten kunnen worden bepaald.

Soortgelijke experimenten zijn uitgevoerd met bismut, dat nog groter is dan antimoon, in koper. Het toevoegen van 1% bismut aan koper leidt tot precipitatie van puur bismut. Op de breukvlakken is het aantal waargenomen precipitaten hoger dan het aantal gaten in Cu-Sb,S maar nog steeds in dezelfde orde van grootte. Hieruit wordt geconcludeerd dat precipitatie van bismut uitmondt in de vorming van zwakke plekken die leiden tot verbrossing.

Tenslotte blijkt dat de kwantificatie van de hoeveelheid antimoon aan de korrelgrenzen bemoeilijkt wordt door de inhomogene samenstelling van de bovenste atoomlagen en de hoeken die de oppervlakken maken met de detector. Uit metingen op oppervlakken met vergelijkbare inclinatie blijkt dat de hoeveelheid antimoon aan de korrelgrenzen toeneemt wanneer de bulk concentratie toeneemt en wanneer de temperatuur van de warmtebehandeling afneemt. Lange tijd verhitten op dezelfde temperatuur leidt tot een breder concentratieprofiel, vergezeld van een lagere concentratie aan het oppervlak.

Segregatie van boor in Ni_3Al

De sterk geordende legering Ni_3Al heeft aantrekkelijke eigenschappen die het materiaal interessant maken voor bepaalde toepassingen bij hoge temperaturen. De sterkte van Ni_3Al dat uit één kristal bestaat neemt toe wanneer de temperatuur toeneemt en het materiaal wordt beschermd tegen corrosie door de vorming van een resistente oxidehuid bij hoge temperatuur. Polykristallijn Ni_3Al is echter extreem bros op kamertemperatuur. Dit probleem kan worden verholpen door kleine hoeveelheden boor, dat naar de korrelgrenzen segregeert, toe te voegen. De precieze processen die plaatsvinden aan de korrelgrens zijn nog steeds onbekend. Auger elektronen spectroscopie wordt gecombineerd met *orientation imaging microscopy* (OIM) om de invloeden van boor aan de korrelgrenzen te bestuderen.

Boor wordt gedetecteerd op de oppervlakken, na intergranulaire breuk van Ni_3Al-B. De intensiteit van boor neemt toe, binnen 24 uur na het breken, door segregatie naar het oppervlak onder de invloed van zuurstof en verrijking van

nikkel aan het oppervlak. Zwavel segregeert bij hoge temperaturen naar interne oppervlakken zoals gaten. De aanwezigheid van zwavel aan een oppervlak verhindert oxidatie en daarmee oppervlaktesegregatie van boor.

Materiaal met een kerf breekt altijd bros, wat toegeschreven wordt aan verhoogde rek en reksnelheid in de buurt van de kerf. De hoeveelheid boor heeft een grote invloed op het breukgedrag van Ni_3Al zonder kerf, wat wordt toegeschreven aan de effecten van boor in de korrels en aan de korrelgrenzen. Boor toevoeging (van 0 naar 0.2 at.%) leidt tot verhoogde slip transmissie aan de korrelgrenzen. Bij verdere verhoging van de boor concentratie neemt de hoeveelheid aan de korrelgrens en dus de slip transmissie niet toe. De vloeispanning neemt echter wel toe bij verdere toevoeging van boor, wat leidt tot een grotere kans op brosse breuk van het materiaal.

De Σ3 korrelgrenzen zijn sterk, wat blijkt uit de OIM observaties van gewalst en verhit materiaal. OIM laat zien dat de misoriëntatie binnen korrels toeneemt in de buurt van de korrelgrenzen en *triple junctions*, doordat dit de plekken zijn waar de door de naburige korrels opgelegde beperkingen maximaal zijn. Dit betekent dat er wel degelijk deformatie plaatsvindt aan de korrelgrenzen. In Ni_3Al zonder boor is er in het geheel geen interactie aan de korrelgrens, aangezien dit bij de minste deformatie al intergranulair breekt. Zowel de OIM resultaten als de invloed van de korrelgrootte wijzen in de richting van een toename van slipactiviteit aan de korrelgrenzen door de aanwezigheid van boor.

Naast de concentratie in de bulk, warmtebehandelingen en spanningen door verschillen in grootte zijn er nog andere factoren die segregatie naar grensvlakken kunnen beïnvloeden. Competitie met andere elementen (S met Sb in Cu), de aanwezigheid van zuurstof aan het oppervlak (Mg in Al_3Mg_2, B in Ni_3Al) en elektronische effecten (B naar Ni-rijke grensvlakken) zijn onderzocht en geven blijk van grote invloeden op segregatie. Bovendien kan het instrument waarmee segregatie gemeten wordt zelf segregatie bevorderen, verhinderen en de waarnemingen ervan nadelig beïnvloeden, wat voorzichtigheid bij het interpreteren van gegevens nodig maakt.

DANKWOORD

Vier jaar geleden, een aantal tijdzones ten oosten van hier, is het proces in gang gekomen dat uiteindelijk geleid heeft tot de totstandkoming van dit proefschrift. De kiem was echter al gelegd tijdens het daaraan voorafgaande afstudeerproject bij de vakgroep Technische Natuurkunde/Materiaalkunde. Het dagelijks bezig zijn met wetenschappelijk onderzoek smaakte naar meer, zodat ik de kans bij dezelfde vakgroep te kunnen promoveren meteen aangreep.

Voor het bieden van die kans en voor de wetenschappelijke begeleiding in de afgelopen jaren wil ik mijn promotor, Jeff De Hosson, van harte bedanken. Van hem heb ik altijd voldoende input gekregen en de mogelijkheid met de meest geavanceerde apparatuur te kunnen werken. Het heeft mij de afgelopen jaren dan ook aan weinig ontbroken.

George Palasantzas wil ik bedanken voor de samenwerking gedurende de laatste drie jaar en het wegnemen van mijn *horror vacuï*. Inhoudelijke discussies over publicaties waren in een juiste balans met het gesleutel aan en verbeteren van de instrumenten.

Verder wil ik de vaste medewerkers van de vakgroep Technische Natuurkunde/Materiaalkunde bedanken: Henk Bron, van SEM introductie tot sample preparatie, Paul Bronsveld voor zijn nimmer aflatende interesse, met name voor Ni_3Al-B, Coen van Dijk voor zijn SEM en E-SEM expertise, Jan Harkema voor de talloze glasbuizen en andere technische hoogstandjes, Irene De Hosson voor al het werk dat ze me uit handen heeft genomen, Bart Kooi voor zijn bijdrage aan hoofdstuk 4 en het beantwoorden van alle soorten vragen, Uko Nieborg voor al zijn constructies en Klaas Post en Reint Vegt voor mijn korte kennismaking met de wereld van de lasers.

De lijst met collega promovendi en post-docs is te lang om iedereen de aandacht te geven die hij of zij verdient. Door de jaren heen is deze groep regelmatig van samenstelling veranderd; wat altijd bleef was de goede onderlinge verstandhouding. Dit maakt niet alleen het onderling discussiëren over wetenschap bijzonder gemakkelijk; het uit zich ook in gecultiveerde gekte zoals borrels, uitjes en Tour-middagen.

Kortom, Peter Balke, Nuno Carvalho, Patricia Carvalho, Steven Celotto, Jim-Wah Chung, Bas Groen, Henk Haarsma, Marc-Jan de Haas, Hans Hegeman, Jaap Hooijmans, Jacob Kerssemakers, Arjen Kloosterman, Siete Koch, Emiel Metselaar, Stefan Mogck, Vašek Ocelík, Yutao Pei, Ronald Popma, Arjen Roos, Erik Teeuw, Tiedo Tinga, Arjan Vreeling, Tomáš Vystavel, Onne Wouters en Edzo Zoestbergen, bedankt.

De studenten Siete Koch, Henk-Jan Kooij, Herman Nicolai en Wouter Soer die met mij, al dan niet direct, hebben samengewerkt worden bedankt voor hun bijdrage.

De hoogleraren Boerma, Van der Giessen en Van Veen ben ik dankbaar voor het doornemen en beoordelen van dit proefschrift en professor Van Veen voor de NDP metingen.

Ed Snoek van JEOL was, ondanks zijn drukke schema, altijd bereid de reis naar het noorden te wagen als er iets was met het instrument waar ik met James Kuipers en George niet uit kon komen.

Mijn kamergenoten in gebouw 13 wil ik bedanken voor het aanhoren van mijn monologen en hun bijdrage aan dit proefschrift; zeker de hulp van Peter Balke met de OIM was onmisbaar.

Het was een eer om voor de stichting FOM te mogen werken; zij wordt bedankt voor de ondersteuning en alle geboden mogelijkheden.

Inspanning tijdens het werk moet gecompenseerd worden door ontspanning daarbuiten. Activiteiten van de MK-Studs (in de breedste zin) zoals voetbal via Walrus of DWS, buitenlandse trips, weekenden in afzondering en andere traditionele samenkomsten staan hiervoor garant en kunnen daarom niet onvermeld blijven. Het is geen toeval dat mijn paranimfen, Arjan Vreeling en Wim Oele, uit deze groep gerecruteerd zijn.

Tenslotte wil ik Tanja, mijn ouders, zus, familie en vrienden bedanken voor hun belangstelling, onvoorwaardelijke steun en de relativerende kijk op wetenschappelijk onderzoek. Tanja, het beseffen van de reden tot reizen maakte dat de dagelijkse autorit gereduceerd werd tot een ‘rondje rond de kerk’!